

Theoretical Study of Inhomogeneous Polymeric Systems

Theoretical Study of Inhomogeneous Polymeric Systems

By

Ashkan Dehghan Kooshkghazi

A Thesis

Submitted to the School of Graduate Studies

in Partial Fulfillment of the Requirements

for the Degree

Doctor of Philosophy

McMaster University

©Copyright by Ashkan Dehghan Kooshkghazi

Declaration

DOCTOR OF PHILOSOPHY, McMaster University Hamilton, Ontario

TITLE: Theoretical Study of Inhomogeneous Polymeric Systems

AUTHOR: Ashkan Dehghan Kooshkghazi, M.Sc. SUPERVISOR: Dr. An-Chang Shi

Abstract

In this thesis, we use the self-consistent field theory (SCFT) to study neutral and charged block copolymer melts and blends in thin films and bulk. We showcase the utility of the SCFT by applying it to a number of different model systems.

In our first study, we examined the elastic properties of multi-component bilayer membranes composed of amphiphilic AB/ED diblock copolymers. We focused on the effects of chain architecture and interactions between the amphiphilic molecules on the line tension or edge energy of a membrane pore. We discovered a direct relationship between the effective volume of the amphiphilic molecules, which is dictated by their architecture, and the line tension. We found that the addition of cone-shaped molecules to the membrane results in a decrease in the line tension. The opposite effect is seen for inverse cone-shaped amphiphiles, where an increase in their concentration results in an increase of the line tension.

Studies two and three fall under the theme of directed self assembly of block copolymer thin films. First we examined the effects of ion concentration on the strength of the external electric field required to reorient lamellar domains from the parallel to the perpendicular orientation. The change in the critical electric field is found to be dependent on whether the neutral or charged polymer species is favoured by the top and bottom surfaces. In the second study, we examined the mechanism of using the entropic effect to direct the self assembly of micro domains in star block copolymer thin films. We control the architecture of star block copolymers by varying the number of arms, ranging from a linear chain with 1-arm to 4-arm star block copolymers. Using both experiments and SCFT, we showed that the entropic effect is enhanced in star block copolymer blends with greater number of arms. Furthermore, we showed that the entropic effect can be used to direct the self assembly of micro domains perpendicular to the substrate.

In our last study, we examined the unbinding transition of the α -BN phase in pentablock terpolymer/homopolymer blends. We constructed a phase diagram of the system as a function of homopolymer concentration. We discovered that the unbinding transition is preempted by the macrophase separation of the

blends into block copolymer rich/ homopolymer rich domains.

The results presented in this thesis help advance our understanding of various properties of polymeric systems, such as the elastic properties of multi-component membranes, directed self assembly in block copolymer thin films and the phase behaviour of block copolymers in bulk.

Acknowledgements

As I look back at my journey through graduate school, I can not help but feel extremely fortunate to have had the privilege to work with so many amazing people. I am very lucky and grateful to have been a part of an incredible community of physicists at McMaster University. Most important of all, my supervisor and mentor, Dr. An-Chang Shi, I can not thank you enough for your kind support and guidance over the years. You have always motivated me to work hard and pushed me to be best that I can be. I am also very thankful to Dr. Kari Dalnoki-Veress, who has been an incredible mentor to me. Kari, I can not thank you enough for inspiring me to pursue my graduate studies, it was the best decision of my life. I owe you big time.

Throughout my research I had the privilege to work with many talented people. Professor Michael Schick, Professor Rong-Ming Ho, Ting-Ya Lo, Jiajia Zhou, Kyle Pastor, Hurmiz Shamana and Chris Gubbels, thank you all for being such wonderful collaborators. Hopefully you enjoyed working with me as much as I enjoyed working with you.

To my parents Fatemeh Taheri and Mehran Dehghan, and my brother and sister, Arash and Negin, no words describe how thankful I am for your endless support and love. You are the reason I have made it this far. I am so lucky to have such a wonderful family. Thank you, thank you, thank you.

To my wonderful friends Saeed, Nehad and Markus. Thank you for all the nerdy discussions we had over coffee. You were always there for me when I needed help. I hope I can one day repay your kindness.

And of course, my amazing partner in life, Sarra Saiyed. Thank you for being so awesome. Your support and love made the bad days good and good days even better. Also, thank you for proof reading my thesis, and sorry for my poor writing skills.

Contents

1	INTRODUCTION	10
1.1	Properties of Polymers	10
1.2	Self-Consistent Field Theory	13
1.3	Objective and Outline	14
2	THEORETICAL METHODS	16
2.1	Neutral Block Copolymers	17
2.2	Charged Block Copolymers	22
2.3	Block Copolymers in Confinement	27
3	NUMERICAL METHODS	30
3.1	Pseudo Spectral Method	31
3.2	Alternating Direction Implicit Method	35
4	LINE TENSION OF MULTICOMPONENT BILAYER MEMBRANES	43
5	EFFECT OF MOBILE IONS ON THE ELECTRIC FIELD NEEDED TO ORIENT CHARGED DIBLOCK COPOLYMER THIN FILMS	53
6	ORIENTING BLOCK COPOLYMER THIN FILMS VIA ENTROPY	67
7	UNBINDING TRANSITION IN PENTABLOCK TERPOLYMER/HOMOPOLYMER BLENDS	93
7.1	Introduction	93
7.2	Results and Discussion	94
7.3	Conclusion	101

8	CONCLUSION AND FINAL REMARKS	103
---	------------------------------	-----

List of Figures

- Figure 1 Schematics of a selection of polymer architectures. In figures (a)-(f) we show examples of linear, branched, multi, charged, star and rigid block copolymers. The inset in Figure (a) shows the molecular structure of a polymer chain. As an example, the monomers are considered to be styrene molecules. 11
- Figure 2 A schematic diagram showing the concept of particle to field transformation. Figure a) shows a complex system of many polymer chains interacting with each other and b) shows the same system where a single polymer chain is interacting with an effective field. 16
- Figure 3 A schematic diagram of a simple neutral diblock copolymer, with two chemically distinct blocks, denoted by A and B. 17
- Figure 4 A schematic diagram of a charged diblock copolymer with negatively charged A block, neutral B block and positive counter ions. 23
- Figure 5 Figure a) shows a schematic diagram of a polymeric system in confinement, and b) shows the effect of confinement on the density of polymers near the surfaces. 28
- Figure 6 A schematic diagram of the computational box in the cylindrical geometry. 37
- Figure 7 A schematic diagram for the $B_1AB_2CB_3/H$ system. 95
- Figure 8 Density profiles for the α -BN, NaCl, $C_{A/C}$ and CsCl morphologies, constructed for the $B_1AB_2CB_3$ melt with $\phi_H=0$. Here, only the A (red) and C (blue) species are presented. 96
- Figure 9 Figure (a), shows a schematic model a graphite structure (public domain image). In Figure (b), we present a side and top-down view of the α -BN morphology. 96

- Figure 10 In Figure (a) we present the density distribution for the tail and bridge junctions, shown in grey and black respectively. In Figure (b), we present a schematic diagram showing that the B_2 bridge blocks concentrated within the α -BN plane, whereas the B_1 and B_3 tail blocks concentrate in the region between the planes. 97
- Figure 11 In Figures (a) and (b) we present the density profiles for the tail and bridge junctions for the $C_{A/C}$ and NaCl phases respectively. 98
- Figure 12 Phase diagram for the $B_1AB_2CB_3$ -H blends in the f_{B_2} - ϕ_H plane. 99
- Figure 13 Figure (a), shows the density profiles for the α -BN and single-layer α -BN phases, where homopolymers are shown in yellow. In Figure (b), we show the free energy for the α -BN phase, single-layer α -BN morphology and the disordered phase, as a function of chemical potential. 100
- Figure 14 The normalized period of the α -BN phase in the x, y and z directions plotted as a function of homopolymer concentration. 101

1 | Introduction

1.1 PROPERTIES OF POLYMERS

Polymers are a remarkable class of materials with wide applications in nanotechnology, material engineering and medicine (1–4). They also form a major component of many biological systems. Natural polymers such as proteins, DNA and RNA molecules are abundant in biological systems and they play a crucial role in many biological processes (5). Synthetic polymers such as polystyrene and polyethylene are used extensively in material engineering, and form the major component of many widely used materials such as glue and plastics (6). Given their ubiquitous presence in daily life and advanced technology, the study of polymers has branches in physics, chemistry, engineering and biology. The focus of this thesis is to present results from our theoretical studies of equilibrium properties of inhomogeneous polymeric systems. We begin by defining what a polymer is, and describe in detail some of their fundamental properties.

Polymers are long string-like macromolecules composed of repeating units called monomers (7, 8). They can have simple or complex chemical and architectural structures. Figure 1 presents a selection of polymers with different types of architecture and chemical composition. In Figure 1.a we show a simple linear diblock copolymer composed of two chemically distinct types of monomers, shown in red and blue. Polymers could have complex architectures, such as branched, star or multiblock copolymers, as shown in Figures 1.b, 1.c and 1.e.

Furthermore, polymeric species could be neutral or charged. A schematic of a charged diblock copolymer is shown in Figure 1.d. In this picture, negative charges are fixed to the backbone of the chain, whereas the dissociated positive ions are free. Lastly, the chemistry of the monomers often dictates the flexibility of the polymer chain. Although most polymer species with high degree of polymerization are flexible in nature, the degree of flexibility could depend on the chemistry of the monomers. For example poly(styrene-

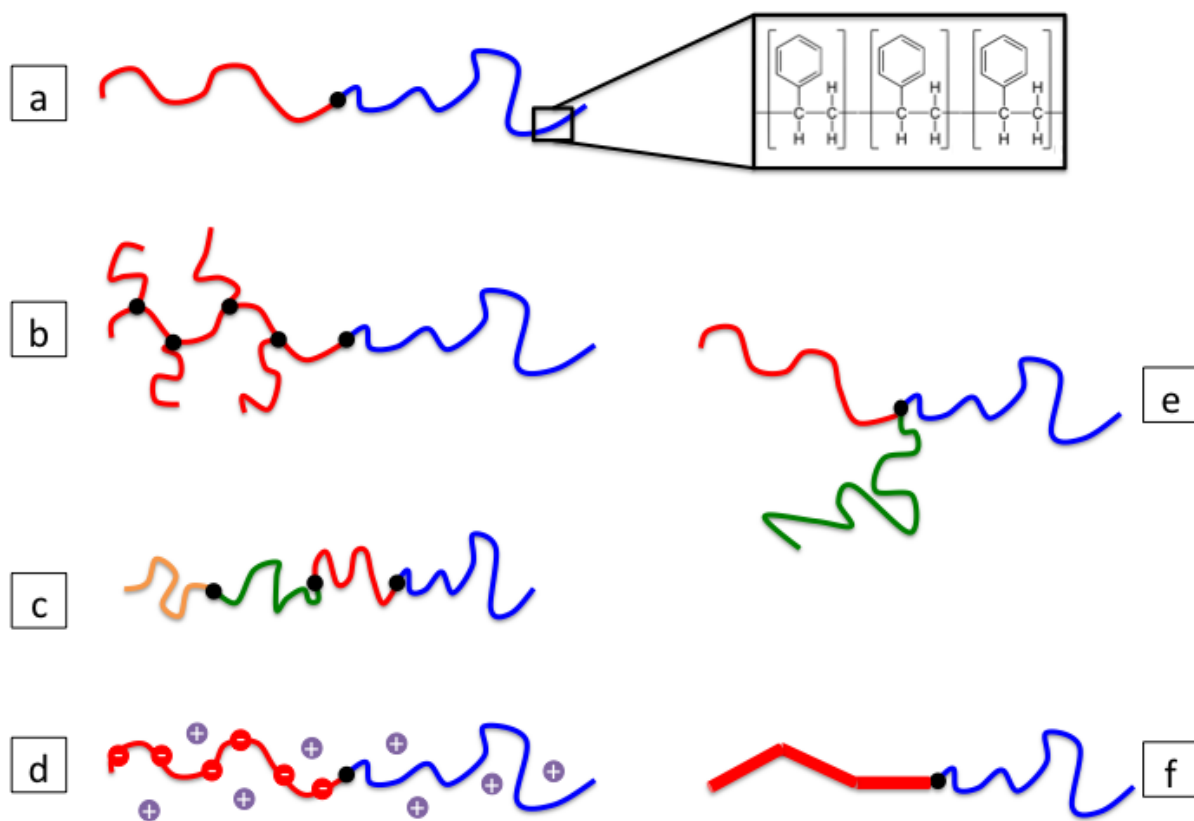


Figure 1: Schematics of a selection of polymer architectures. In figures (a)-(f) we show examples of linear, branched, multi, charged, star and rigid block copolymers. The inset in Figure (a) shows the molecular structure of a polymer chain. As an example, the monomers are considered to be styrene molecules.

block-(2,5-bis[4-methoxyphenyl]oxycarbonyl)styrene) (PS-*b*-PMPCS) is composed of a flexible PS block and rigid rod-like PMPCS block (9). The flexibility of the polymer chains, dictated by the chemistry of the monomers, could effect the phase behaviour and mechanical properties of the polymer melts or solutions (9). Figure 1.f presents a schematic example of a rod-coil diblock copolymer chain with rigid and flexible blocks.

There is an endless variety of polymer architectures and chemical compositions, each with unique phys-

ical and chemical properties. The complexity of the polymer chains results in a very large parameter space, within which one could ideally find a system with properties desirable for particular applications. However, a comprehensive study of the entire parameter space for a polymeric system is often difficult due to the multi dimensional nature of the phase space. Modern theoretical techniques, together with robust and efficient numerical methods, makes it possible to explore this multi dimensional phase space. To construct a theoretical framework for studying the equilibrium behaviour of polymeric systems, one has to construct a model for describing the statistics of a single polymer chain, in addition to capturing the statistics of the many-body system of polymer melts or solutions (10). Although the sheer complexity of polymer chains and polymeric systems makes this a daunting task, there are several properties of the polymers which help simplify the problem.

Despite the fact that the chemistry of the monomers plays an important role in defining the properties of polymers at the microscopic level, at length scales comparable to the size of the polymer chain ($\sim 10 - 100nm$) certain universal properties emerge. These universal properties are independent of the details at the microscopic level (1, 10). Among such properties is the dependence of the size of the polymer chain, measured in terms of the radius of gyration R_g , or the degree of polymerization N (11). The scaling relationship between the size of the polymers and their degree of polymerization is often written as $R_g \sim N^\nu$, where the scaling exponent $\nu = \frac{1}{2}$ for ideal polymers (7). In general, the conformation of a polymer chain, or its three dimensional structure, depends on three factors; the flexibility of the chain, the interaction of the monomers on the chain with one another and the interaction of the monomers with their surroundings (7). For polymer chains with high degree of polymerization, the conformation of the chains can be described using the ideal chain model (7, 10). In this model, we ignore the long range interactions between the monomers and describe the chain as a random walk. The ideal chain model is valid for polymers in dense polymer melts or blends (7, 10). The statistics of an ideal polymer chain can be described using the Gaussian chain model. The model systems studied in this thesis are composed of dense blends or melts of block copolymers with high degree of polymerization. We therefore describe the statistics of the polymer chains using the Gaussian chain model. A more detailed description of the Gaussian chain model is presented in later chapters.

The second challenge in constructing a theoretical framework for studying the equilibrium properties of polymers is to implement a statistical model for describing the many-body nature of polymeric systems.

Fortunately, in dense polymer melts and blends, the large effective coordination number ensures the validity of the mean field approximation (10), therefore allowing us to implement mean field techniques, such as self-consistent field theory to study the equilibrium properties of polymeric systems. In chapter two, we outline in detail the self-consistent field theory framework for neutral and charged block copolymers. Before delving into the mathematical description of the self-consistent field theory, we present a brief historical overview of the SCFT framework.

1.2 SELF-CONSISTENT FIELD THEORY

One of the most powerful theoretical tools for studying the equilibrium properties of dense polymeric systems is the self-consistent field theory or SCFT for short. The pioneering work of Edwards, de Gennes, Helfand and others, laid the foundation for the modern self-consistent field theories (12–14). Over the years, a number of different analytical techniques have been developed for solving the SCFT equations. Most notably are weak segregation theory by Leibler and the strong segregation theory by Semenov (15, 16). The pioneering work of Leibler, Semenov and others provided useful methods for investigating the equilibrium phase behaviour of polymeric systems at the strong and weak segregation limits. Increase in the availability and power of modern computers in the early 2000s accelerated the study of polymer physics and helped bridge the gap between previously proposed analytical techniques.

Perhaps one of the most important breakthroughs was the introduction of the spectral method for solving the SCFT equations by Matsen, Schick (17, 18). Using this technique, the authors investigated the phase behaviour of diblock copolymers, and obtained a phase diagram as a function of block composition and the product of the Flory-Huggins parameter and degree of polymerization (17, 18). Other important contributions to the development of methods for solving the SCFT equations are due to pioneering work by Helfand, Whitmore, Shi and others (19–22). Another powerful tool, in the family of spectral techniques, is the pseudo spectral method which leverages the best of real space and reciprocal space for solving the SCFT equations (23, 24). In recent years, advances in efficient numerical algorithms and computers have allowed polymer physicists to tackle more complex and interesting problems. For example, the study of weakly charged polymeric systems (25, 26), polymers in confined geometries (27–29) and polymers as a mean to model

biological systems (30, 31) are just a handful of examples highlighting the utility of the self-consistent field theory.

1.3 OBJECTIVE AND OUTLINE

We use self-consistent field theory as a tool to study the equilibrium properties of neutral and charged block copolymers. The objective is to highlight the utility of the SCFT as a powerful tool to obtain solutions of model systems and to gain understanding of these systems from the results. In chapter 2, we present a detailed description of the self-consistent field theory framework, where we develop models for neutral and charged systems in bulk and thin film geometries. In chapter 3, we introduce numerical techniques for solving the SCFT equations. We focus on two techniques in particular, the pseudo-spectral and a finite-difference method known as alternating direction implicit technique. Having built the appropriate foundation for model building using the SCFT framework, we examine three main topics: elastic properties of bilayer membranes, directed self-assembly in polymer thin films and the phase behaviour of multiblock copolymers in bulk.

In the first study we use self-consistent field theory to investigate the elastic properties of multi-component bilayer membranes. In particular, we examine the line tension or edge energy as a function of lipid architecture and molecular interactions. We model lipid molecules as amphiphilic diblock copolymers, forming a membrane in a solvent modelled as homopolymers. The architecture of the molecules is controlled by adjusting the volume fractions of the hydrophilic and hydrophobic groups. With this, we examine two scenarios. One, in which the hydrophilic head groups are larger than the hydrophobic tails, resulting in a cone-shaped molecular structure. Second, in which the hydrophobic tails are larger than the hydrophilic heads, resulting in an inverse cone-shaped structure. By studying the density distribution of the amphiphilic molecules throughout the membrane, we try to understand the effects of chain architecture on the line tension. Lastly, we examine the effects of interactions between the head groups of the amphiphilic molecules on the pore line tension.

In the second and third study, we use SCFT to investigate the self-assembly of block copolymers in confined geometries. We explore two novel mechanisms for directing the self-assembly of micro domains perpendicular to the thin film surfaces. In the first study, we use an external electric field to align micro

domains in lamellae forming charged block copolymers perpendicular to the substrate. In the study following that, the entropic effect of polymers is used as a mechanism to direct the self-assembly of star block copolymers in a thin film geometry.

We first investigate the effects of ion concentration on the strength of the electric field required to reorient lamellar domains from the parallel alignment, preferred by the surface interactions, to the perpendicular orientation. We focus on two main scenarios. In the first case, we consider melts in which the neutral blocks interact favourably with the surfaces. In the second scenario, we examine thin films in which the charged species interact favourably with the surfaces. In both cases, we control the mobility of the free ions by adjusting χ_{BI} , the strength of interaction between the ions and the B polymer species. Furthermore, we calculate the phase behaviour of the system as a function of the surface interactions, focusing the parallel, perpendicular and mixed morphologies.

In the second study of this unit, we explore the effects of entropy on the orientation of lamellae and cylinder forming $(PS-PDMS)_n$ star block copolymer thin films. The entropic effect is examined using both experiments and self-consistent field theory. Using SCFT, we model the $(PS-PDMS)_n$ polymers as $(AB)_n$ star block copolymers. We control the strength of the entropic effect by adjusting the number of arms from $n=1$ to $n=4$. We consider lamellae and cylinder forming $(AB)_n$ star block copolymers in which the (PDMS) or A species interact favourably with the air surface. Using SCFT, we calculate the free energies of the parallel, perpendicular and mixed morphologies as a function of n , the number of arms in the $(AB)_n$ system. In this work, we explore the phase behaviour of the $(AB)_n$ star block copolymer thin films and make direct comparison between the experiments and the SCFT results.

In the last study, we examine the unbinding transition of the α -BN phase in the $B_1AB_2CB_3$ pentablock terpolymer / homopolymer blends. We investigate the phase behaviour of the pentablock terpolymers as a function of homopolymer concentration, constructing a phase diagram in the ϕ_H-fB_2 plane. We compare the free energies of the α -BN, single-domain α -BN and the homogenous phases to study the unbinding transition in the α -BN structure. The key question we aim to answer is whether the increase in the homopolymer concentration results in an unbinding transition at a finite ϕ_H , or if the unbinding transition is preempted by a macrophase separation of the blends into a homopolymer rich/ block copolymer rich macro domains.

2 | Theoretical Methods

In this chapter, we present a theoretical framework to describe the equilibrium thermodynamic properties of polymeric systems. More specifically, we present a field-theoretic model, where the complex many-body interactions between polymer chains are replaced with the interaction between a single polymer chain and an effective field, as shown schematically in Figure 2 (10, 32).

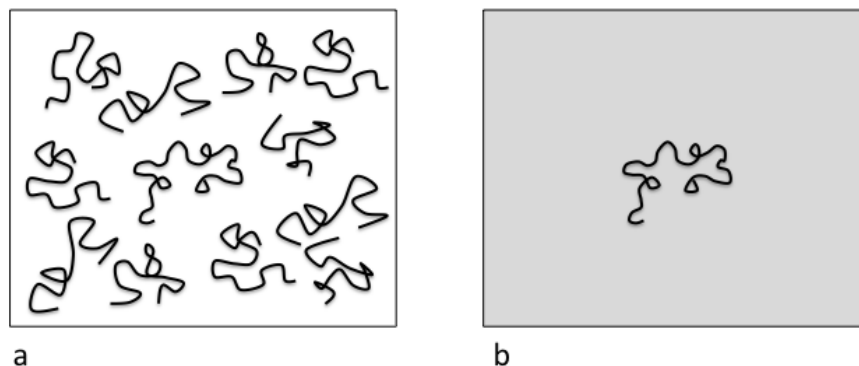


Figure 2: A schematic diagram showing the concept of particle to field transformation. Figure a) shows a complex system of many polymer chains interacting with each other and b) shows the same system where a single polymer chain is interacting with an effective field.

As described earlier, Edwards was the first to work out the statistics of a polymeric system in a field theoretic framework (14). Since then, field theory models have been extended to explore a wide spectrum of diverse and interesting problems. The modern version of the field theoretic model of polymers is commonly referred to as self-consistent field theory (SCFT) (1, 10). In this chapter, we present self-consistent field theory models for neutral and charged polymeric systems in bulk and confined geometries. The result of applying the SCFT formalism is a set of mean field equations, which could be solved self-consistently to determine the equilibrium properties of a polymeric system.

2.1 NEUTRAL BLOCK COPOLYMERS

In this section, we consider a system of n_{AB} neutral diblock copolymers in volume Ω . The AB diblock copolymers, as shown in Figure 3, have degree of polymerization N_{AB} .

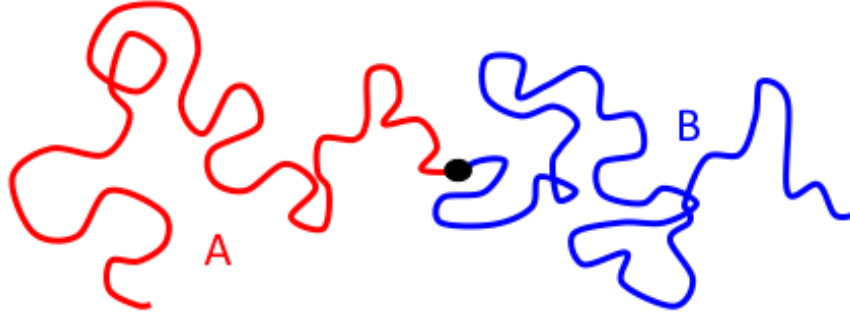


Figure 3: A schematic diagram of a simple neutral diblock copolymer, with two chemically distinct blocks, denoted by A and B.

The fraction of A block is denoted by f and the fraction of B block by $1 - f$. The hardcore volume per monomer is defined as $v_\alpha = \frac{1}{\rho_\alpha^\circ}$, where $\alpha = A, B$. We define the densities for the A and B species using,

$$\begin{aligned}\hat{\rho}_A(\mathbf{r}) &= \sum_{i=1}^{n_{AB}} \int_0^f ds \delta(\mathbf{r} - \mathbf{R}_i^A(s)), \\ \hat{\rho}_B(\mathbf{r}) &= \sum_{i=1}^{n_{AB}} \int_f^1 ds \delta(\mathbf{r} - \mathbf{R}_i^B(s)),\end{aligned}\tag{1}$$

where the $\hat{\rho}$ symbol indicates that the densities are functions of the molecular configuration (I). In the above equation, $\mathbf{R}_i^A(s)$ and $\mathbf{R}_i^B(s)$ are the space curves specifying the position of the segment s along the A and B blocks respectively. In our model, we consider the system to be incompressible and thus require $\sum_{\alpha=A,B} \frac{\rho_\alpha(\mathbf{r})}{\rho_\alpha^\circ} = 1$ at every point in space, where ρ_α° is the monomer reference density for the α species ($I, 10$).

The thermodynamic properties of the system are most conveniently described using the canonical ensemble, with the partition function written as,

$$Z = \left(\frac{\xi_{AB}^{n_{AB}}}{n_{AB}!} \right) \prod_{i=1}^{n_{AB}} \int D[\mathbf{R}_i^A(s)] D[\mathbf{R}_i^B(s)] P_A[\mathbf{R}_i^A(s)] P_B[\mathbf{R}_i^B(s)] \delta[\mathbf{R}_i^A(f) - \mathbf{R}_i^B(1-f)] \prod_{\mathbf{r}} \delta \left(\sum_{\alpha=A,B} \frac{\hat{\rho}_{\alpha}(\mathbf{r})}{\rho_{\alpha}^{\circ}} - 1 \right) \exp[-U[\hat{\rho}(\mathbf{r})]]. \quad (2)$$

The functional integrals in the above equation are over all possible chain configurations (I, IO). Here, $\xi_{AB}^{n_{AB}}$ is the single chain partition function due to the kinetic energy, and $n_{AB}!$ is introduced due to the fact that the polymer chains are indistinguishable (I, IO). The delta function $\delta[\mathbf{R}_i^A(f) - \mathbf{R}_i^B(1-f)]$ in Eq.2 ensures that the A and B blocks are connected. Furthermore, $\delta \left(\sum_{\alpha=A,B} \frac{\hat{\rho}_{\alpha}(\mathbf{r})}{\rho_{\alpha}^{\circ}} - 1 \right)$ enforces the incompressibility condition. We consider the polymer chains to be flexible and monodisperse, where their statistics can be described using the continuous Gaussian chain model (33). We write the Boltzmann distributions $P_A[\mathbf{R}_i^A(s)]$ and $P_B[\mathbf{R}_i^B(s)]$ for the polymer chains as,

$$P_A[\mathbf{R}_i^A(s)] = C \exp \left[-\frac{3}{2b^2} \int_0^f ds \left(\frac{d\mathbf{R}_i^A(s)}{ds} \right)^2 \right],$$

$$P_B[\mathbf{R}_i^B(s)] = C \exp \left[-\frac{3}{2b^2} \int_f^1 ds \left(\frac{d\mathbf{R}_i^B(s)}{ds} \right)^2 \right], \quad (3)$$

where C is a normalization constant. In the above equations, we assumed that the Kuhn length b is the same for both A and B species.

The energy of the system $U[\hat{\rho}(\mathbf{r})]$ is a functional of the polymer density, where for neutral polymers, it accounts for the contribution from the short range interactions between the polymer segments (33). The energy due to the short range interactions can be written as,

$$U[\hat{\rho}(\mathbf{r})] = \frac{1}{2} \sum_{\alpha\beta=A,B} \int d\mathbf{r} \hat{\rho}_{\alpha}(\mathbf{r}) \chi_{\alpha\beta} \hat{\rho}_{\beta}(\mathbf{r}), \quad (4)$$

where $\chi_{\alpha\beta}$ is the Flory-Huggins parameter between the α and β species. χ is a dimensionless phenomenological parameter that is a measure of the difference in the interaction between the like and unlike segments (7, 34). The $\frac{1}{2}$ factor in Eq.4 is introduced to correct for double counting.

Using the definitions for the stretching energy of the polymer chains Eq.3 and the short range interactions between the segments Eq.4, we rewrite the partition function as,

$$Z = \left(\frac{\xi_{AB}^{n_{AB}}}{n_{AB}!} \right) \prod_{i=1}^{n_{AB}} \int D[\mathbf{R}_i^A(s)] D[\mathbf{R}_i^B(s)] \prod_{\mathbf{r}} \delta \left(\sum_{\alpha=A,B} \frac{\hat{\rho}_\alpha(\mathbf{r})}{\rho_\alpha^\circ} - 1 \right) \exp \left[-\frac{1}{2} \sum_{\alpha\beta=A,B} \int d\mathbf{r} \hat{\rho}_\alpha(\mathbf{r}) \chi_{\alpha\beta} \hat{\rho}_\beta(\mathbf{r}) - \frac{3}{2b^2} \sum_{\alpha=A,B} \int ds \left(\frac{d\mathbf{R}_i^\alpha(s)}{ds} \right)^2 \right], \quad (5)$$

where the normalization constants from Eq.3 are absorbed into the definition of $\xi_{AB}^{n_{AB}}(I)$. The above partition function is written in terms of the functional integral over the configuration of the polymer chains. A standard approach in polymer physics is to perform a particle (or polymer segment) to field transformation, which replaces the polymer-polymer interactions with a polymer-field interaction ($I, I0$). The first step in this formalism is to introduce the auxiliary fields $\rho_\alpha(\mathbf{r})$ and $\omega_\alpha(\mathbf{r})$, through the following identity (35),

$$\int D[\rho_\alpha(\mathbf{r})] \prod_{\mathbf{r}} \delta[\rho_\alpha(\mathbf{r}) - \hat{\rho}_\alpha(\mathbf{r})] = \int D[\rho_\alpha(\mathbf{r})] D[\omega_\alpha(\mathbf{r})] \exp \left[\int d\mathbf{r} \omega_\alpha(\mathbf{r}) [\rho_\alpha(\mathbf{r}) - \hat{\rho}_\alpha(\mathbf{r})] \right] = 1. \quad (6)$$

Here, $\rho_\alpha(\mathbf{r})$ can be interpreted as the polymer segment number density, and $\omega_\alpha(\mathbf{r})$ as the inhomogeneous chemical potential. It is important to note that the range of the integral for $\omega_\alpha(\mathbf{r})$ is over a line in the complex plane from $-i\infty$ to $i\infty$ ($I0$). Using the above identity, we can rewrite the partition function in the following form,

$$Z = \left(\frac{\xi_{AB}^{n_{AB}}}{n_{AB}!} \right) \int D[\rho_\alpha(\mathbf{r})] D[\omega_\alpha(\mathbf{r})] D[\mathbf{R}_i^A(s)] D[\mathbf{R}_i^B(s)] \prod_{\mathbf{r}} \delta \left(\sum_{\alpha=A,B} \frac{\rho_\alpha(\mathbf{r})}{\rho_\alpha^\circ} - 1 \right) \exp \left[-\frac{1}{2} \sum_{\alpha\beta=A,B} \int d\mathbf{r} \rho_\alpha(\mathbf{r}) \chi_{\alpha\beta} \rho_\beta(\mathbf{r}) - \frac{3}{2b^2} \sum_{\alpha=A,B} \int ds \left(\frac{d\mathbf{R}_i^\alpha(s)}{ds} \right)^2 + \sum_{\alpha=A,B} \int d\mathbf{r} \omega_\alpha(\mathbf{r}) [\rho_\alpha(\mathbf{r}) - \hat{\rho}_\alpha(\mathbf{r})] \right]. \quad (7)$$

The chain-conformation dependent contribution to the partition function can be expressed in the following way,

$$Q_{AB} = \frac{1}{\Omega} \int D[\mathbf{R}_i^A(s)] \int D[\mathbf{R}_i^B(s)] \delta[\mathbf{R}_i^A(f) - \mathbf{R}_i^B(1-f)] \exp \left[-\frac{3}{2b^2} \sum_{\alpha=A,B} \int ds \left(\frac{d\mathbf{R}_i^\alpha(s)}{ds} \right)^2 - \sum_{\alpha=A,B} \int d\mathbf{r} \omega_\alpha(\mathbf{r}) \hat{\rho}_\alpha(\mathbf{r}) \right], \quad (8)$$

where Q_{AB} is referred to as the single chain partition function (36). The single chain partition function contains the contribution from the chain stretching energy and the coupling of the local densities to the inhomogeneous chemical potential $\omega_\alpha(\mathbf{r})$. We further simplify the partition function by introducing a Lagrange multiplier $\eta(\mathbf{r})$, which enforces the incompressibility (1),

$$\prod_{\mathbf{r}} \delta\left(\sum_{\alpha=A,B} \frac{\rho_\alpha(\mathbf{r})}{\rho_\alpha^\circ} - 1\right) = \int D[\eta] \exp\left[\int d\mathbf{r} \eta(\mathbf{r}) \left(\sum_{\alpha=A,B} \frac{\rho_\alpha(\mathbf{r})}{\rho_\alpha^\circ} - 1\right)\right]. \quad (9)$$

where the range of the integral is over a line in the complex plane from $-i\infty$ to $i\infty$ (10).

Using the above definition for $\eta(\mathbf{r})$ and Q_{AB} , the canonical partition function for the neutral AB diblock copolymers can be written as,

$$Z = \int D[\rho_\alpha(\mathbf{r})] D[\omega_\alpha(\mathbf{r})] D[\eta(\mathbf{r})] \exp\left[-F[\omega_\alpha(\mathbf{r}), \rho_\alpha(\mathbf{r}), \eta(\mathbf{r})]\right], \quad (10)$$

where Stirling approximation $n! \approx (\frac{n}{e})^n$ is used. The functional free energy $F[\omega_\alpha(\mathbf{r}), \rho_\alpha(\mathbf{r}), \eta(\mathbf{r})]$ of the system can be defined as,

$$F[\omega_\alpha(\mathbf{r}), \rho_\alpha(\mathbf{r}), \eta(\mathbf{r})] = \int d\mathbf{r} \left\{ \frac{1}{2} \sum_{\alpha\beta=A,B} \rho_\alpha(\mathbf{r}) \chi_{\alpha\beta} \rho_\beta(\mathbf{r}) - \sum_{\alpha=A,B} \omega_\alpha(\mathbf{r}) \rho_\alpha(\mathbf{r}) + \eta(\mathbf{r}) \left(\sum_{\alpha=A,B} \frac{\rho_\alpha(\mathbf{r})}{\rho_\alpha^\circ} - 1 \right) \right\} - n_{AB} \ln\left(\frac{\xi_{AB} Q_{AB} \Omega}{n_{AB}}\right). \quad (11)$$

It is convenient to express our formulation in terms of the volume fraction of the polymer segments. The volume fraction for the polymer species are defined as, $\phi_\alpha(\mathbf{r}) = \frac{\rho_\alpha(\mathbf{r})}{\rho^\circ}$, where we assume that all species have the same reference segment density $\rho_\alpha^\circ = \rho^\circ$. We can also define the average volume fraction for the AB diblock copolymers as $\bar{\phi}_{AB} = \frac{n_{AB} N_{AB}}{\rho^\circ \Omega}$ (1).

Using the above definitions, we define the free energy density per chain as $f[\omega_\alpha(\mathbf{r}), \phi_\alpha(\mathbf{r}), \eta(\mathbf{r})] = \frac{N_{AB}}{\rho^\circ \Omega} F[\omega_\alpha(\mathbf{r}), \phi_\alpha(\mathbf{r}), \eta(\mathbf{r})]$, and write,

$$f[\omega_\alpha(\mathbf{r}), \phi_\alpha(\mathbf{r}), \eta(\mathbf{r})] = \frac{1}{\Omega} \int d\mathbf{r} \left\{ \frac{1}{2} \sum_{\alpha\beta=A,B} \phi_\alpha(\mathbf{r}) \chi_{\alpha\beta} N_{AB} \phi_\beta(\mathbf{r}) - \sum_{\alpha=A,B} \omega_\alpha(\mathbf{r}) \phi_\alpha(\mathbf{r}) + \eta(\mathbf{r}) \left(\sum_{\alpha=A,B} \phi_\alpha(\mathbf{r}) - 1 \right) \right\} - \bar{\phi}_{AB} \ln\left(\frac{\xi_{AB} Q_{AB} \Omega}{n_{AB}}\right). \quad (12)$$

We scale the auxiliary fields $\omega_\alpha(\mathbf{r})$ and $\eta(\mathbf{r})$ such that; $\omega_\alpha(\mathbf{r}) N_{AB} \rightarrow \omega_\alpha(\mathbf{r})$ and $\eta(\mathbf{r}) N_{AB} \rightarrow \eta(\mathbf{r})$ (1). The field theoretic partition function in Eq.10 is written in terms of the $\phi_\alpha(\mathbf{r})$, $\omega_\alpha(\mathbf{r})$ and $\eta(\mathbf{r})$ auxiliary

fields. Evaluating the free energy of the system, or any observable, requires the evaluation of the functional integrals in Eq.10. Aside from a handful of simple cases, evaluating the partition function in closed form is not possible (1, 10). To evaluate the partition function Eq.10, we use the mean field approximation.

The functional integrals in equation 10 run over an infinite number of configurations. The mean field (saddle point) approximation assumes that the dominant contribution to the partition function is from a single field configuration (10). To evaluate the mean field solutions, we determine the extremum of the functional $f[\omega_\alpha(\mathbf{r}), \phi_\alpha(\mathbf{r}), \eta(\mathbf{r})]$ with respect to the $\omega_\alpha(\mathbf{r})$, $\phi_\alpha(\mathbf{r})$ and $\eta(\mathbf{r})$ auxiliary fields,

$$\begin{aligned}\frac{\delta f[\omega_\alpha(\mathbf{r}), \phi_\alpha(\mathbf{r}), \eta(\mathbf{r})]}{\delta \omega_\alpha(\mathbf{r})} &= 0, \\ \frac{\delta f[\omega_\alpha(\mathbf{r}), \phi_\alpha(\mathbf{r}), \eta(\mathbf{r})]}{\delta \phi_\alpha(\mathbf{r})} &= 0, \\ \frac{\delta f[\omega_\alpha(\mathbf{r}), \phi_\alpha(\mathbf{r}), \eta(\mathbf{r})]}{\delta \eta(\mathbf{r})} &= 0.\end{aligned}\tag{13}$$

The first functional derivative with respect to the $\omega_\alpha(\mathbf{r})$ auxiliary fields results in,

$$\frac{\delta f[\omega_\alpha(\mathbf{r}), \phi_\alpha(\mathbf{r}), \eta(\mathbf{r})]}{\delta \omega_\alpha(\mathbf{r})} = \frac{\delta}{\delta \omega_\alpha(\mathbf{r})} \left\{ - \int d\mathbf{r} \sum_{\alpha=A,B} \omega_\alpha(\mathbf{r}) \phi_\alpha(\mathbf{r}) - \bar{\phi}_{AB} \ln \left(\frac{\xi_{AB} Q_{AB} \Omega}{n_{AB}} \right) \right\}.\tag{14}$$

The single chain partition function Q_{AB} is a functional of the auxiliary field $\omega_\alpha(\mathbf{r})$, as given in Eq.8. By evaluating the above functional derivative we arrive at (10),

$$\begin{aligned}\frac{\delta f[\omega_\alpha(\mathbf{r}), \phi_\alpha(\mathbf{r}), \eta(\mathbf{r})]}{\delta \omega_\alpha(\mathbf{r})} &= -\phi_\alpha(\mathbf{r}) - \frac{\bar{\phi}_{AB}}{Q_{AB}} \frac{\delta}{\delta \omega_\alpha(\mathbf{r})} Q_{AB} \\ &= -\phi_\alpha(\mathbf{r}) - \frac{\bar{\phi}_{AB}}{Q_{AB}} \int ds q_\alpha(\mathbf{r}, s) q_\alpha^\dagger(\mathbf{r}, s),\end{aligned}\tag{15}$$

where, $q_\alpha(\mathbf{r}, s)$ and $q_\alpha^\dagger(\mathbf{r}, s)$ are the end-integrated forward and complementary propagators, respectively. The propagators describe the statistical weight of the chain segment s at position \mathbf{r} in space (37). The propagators in equation 15 are determined by solving the following differential equations,

$$\begin{aligned}\frac{\partial}{\partial s} q_\alpha(\mathbf{r}, s) &= [\nabla^2 - \omega_\alpha(\mathbf{r})] q_\alpha(\mathbf{r}, s), \\ \frac{\partial}{\partial s} q_\alpha^\dagger(\mathbf{r}, s) &= -[\nabla^2 - \omega_\alpha(\mathbf{r})] q_\alpha^\dagger(\mathbf{r}, s).\end{aligned}\tag{16}$$

The above differential equations are known in the polymer physics community as the modified diffusion equations (10). The modified diffusion equations are solved using the following initial conditions: $q_A(\mathbf{r}, 0) =$

1 and $q_A^\dagger(\mathbf{r}, 0) = q_B(\mathbf{r}, 1 - f)$ for the A species and, $q_B(\mathbf{r}, 0) = 1$ and $q_B^\dagger(\mathbf{r}, 0) = q_A(\mathbf{r}, f)$ for the B species.

By evaluating the second and third functional derivatives in Eq.13 and combining them with results from Eq.15, we arrive at the following set of mean field equations,

$$\begin{aligned}
\phi_A(\mathbf{r}) &= \frac{\bar{\phi}_{AB}}{Q_{AB}} \int_0^f ds q_A(\mathbf{r}, s) q_A^\dagger(\mathbf{r}, f - s), \\
\phi_B(\mathbf{r}) &= \frac{\bar{\phi}_{AB}}{Q_{AB}} \int_f^1 ds q_B(\mathbf{r}, s) q_B^\dagger(\mathbf{r}, 1 - s), \\
\omega_A(\mathbf{r}) &= \chi_{AB} N_{AB} \phi_B(\mathbf{r}) + \eta(\mathbf{r}), \\
\omega_B(\mathbf{r}) &= \chi_{AB} N_{AB} \phi_A(\mathbf{r}) + \eta(\mathbf{r}), \\
\sum_{\alpha=A,B} \phi_\alpha(\mathbf{r}) &= 1.
\end{aligned} \tag{17}$$

Equations 16 and 17 are solved self-consistently to determine the mean field solutions to the SCFT equations. Using the solutions to Eq.13, we can write the mean field free energy for the neutral diblock copolymer system as,

$$f_{\text{MF}} = \frac{1}{\Omega} \int d\mathbf{r} \left\{ \frac{1}{2} \sum_{\alpha\beta=A,B} \phi_\alpha(\mathbf{r}) \chi_{\alpha\beta} N_{AB} \phi_\beta(\mathbf{r}) - \sum_{\alpha=A,B} \omega_\alpha(\mathbf{r}) \phi_\alpha(\mathbf{r}) \right\} - \bar{\phi}_{AB} \ln(Q_{AB}). \tag{18}$$

2.2 CHARGED BLOCK COPOLYMERS

We extend the theoretical model for neutral polymers to a system of charged AB diblock copolymers composed of negatively charged A blocks and neutral B blocks. The theoretical model presented here for the charged system is an extension of the neutral AB diblock copolymers and will have a similar overall structure. Therefore, we reference any previously defined equations and notations and only focus on concepts specific to the charged AB system.

Figure 4 presents a schematic diagram of a charged AB diblock copolymer with a negatively charged A block and a neutral B block. As before, N_A and N_B represent the degree of polymerization of the A and B blocks, respectively. We assume that there are n_I positive counter ions dissociated within the system, such

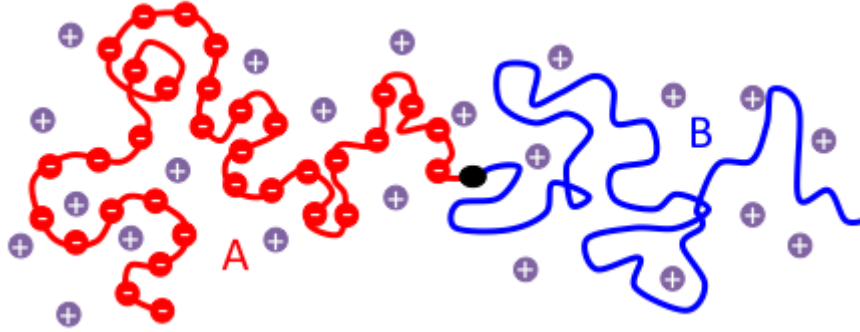


Figure 4: A schematic diagram of a charged diblock copolymer with negatively charged A block, neutral B block and positive counter ions.

that global charge neutrality is satisfied (25). The dimensionless densities for the A and B polymer segments are defined in Eq.1, and similarly we define the density for the positive counter ions as,

$$\hat{\rho}_I(\mathbf{r}) = \sum_{i=1}^{n_I} \delta(\mathbf{r} - \mathbf{r}_i^I), \quad (19)$$

where as before, the symbol $\hat{}$ indicates that the counter ion density is a function of the molecular configuration (I). In the above equation, \mathbf{r}_i^I is the position of the i^{th} ion in the volume Ω . We also define a charge density $\hat{\rho}_e(\mathbf{r})$, which corresponds to the total amount of charge per volume at position \mathbf{r} and write,

$$\hat{\rho}_e(\mathbf{r}) = \hat{\rho}_e^A(\mathbf{r}) + \hat{\rho}_e^I(\mathbf{r}), \quad (20)$$

where,

$$\begin{aligned} \hat{\rho}_e^A(\mathbf{r}) &= \sum_{i=1}^{n_{AB}} \int_0^f ds P_A z_A e \delta(\mathbf{r} - \mathbf{R}_i^A(s)), \\ \hat{\rho}_e^I(\mathbf{r}) &= \sum_{i=1}^{n_I} z_I e \delta(\mathbf{r} - \mathbf{r}_i^I). \end{aligned} \quad (21)$$

Here, z_A and z_I are the valence charges for the A and I species, and e is the elementary unit of charge (25). The parameter P_A represents the fraction of negative charge on the A blocks, where it assumes a value between 0 and 1. The global electroneutrality implies that,

$$\int d\mathbf{r} \hat{\rho}_e(\mathbf{r}) = 0, \quad (22)$$

where the integral is over the volume of the system. As before, we enforce incompressibility by demanding $\sum_{\alpha=A,B} \frac{\hat{\rho}_\alpha(\mathbf{r})}{\rho_\alpha^\circ} = 1$. We describe the thermodynamic properties of the system using the canonical ensemble and write the canonical partition function as,

$$Z = \left(\frac{\xi_{AB}^{n_{AB}}}{n_{AB}!} \right) \left(\frac{\xi_I^{n_I}}{n_I!} \right) \left[\prod_{i=1}^{n_{AB}} \sum_{c_{A,i}(s)} P[c_{A,i}(s)] \right] \left[\prod_{i=1}^{n_{AB}} \int D[\mathbf{R}_i^A(s)] D[\mathbf{R}_i^B(s)] P_A[\mathbf{R}_i^A(s)] P_B[\mathbf{R}_i^B(s)] \right] \delta[R_i^A(f) - R_i^B(1-f)] \left[\prod_{\mathbf{r}} \int d\mathbf{r}_i^I \right] \delta \left(\sum_{\alpha=A,B} \frac{\hat{\rho}_\alpha(\mathbf{r})}{\rho_\alpha^\circ} - 1 \right) \exp \left[-U[\hat{\rho}(\mathbf{r}), V(\mathbf{r})] \right], \quad (23)$$

where $V(\mathbf{r})$ is the electrostatic potential and $\sum_{c_{A,i}(s)}$ is the sum over all possible charge distributions on the A blocks, each with probability $P[c_{A,i}(s)]$ (25, 26). As before, ξ_{AB} and ξ_I are the single molecule partition functions due to the kinetic energy. The statistics of the AB diblock copolymer chains are described using the Gaussian chain model, as given in Eq.3. The energy of the system contains two parts, one due to the short range interactions between the polymer segments and counter ions, as described by Eq.4. The other is due to the electrostatic interactions between the charged species. We write the energy contribution due to the electrostatics as,

$$U_e[\hat{\rho}_e(\mathbf{r}), V(\mathbf{r})] = \int d\mathbf{r} \left[\hat{\rho}_e(\mathbf{r}) V(\mathbf{r}) - \frac{\varepsilon(\mathbf{r})}{2} |\nabla V(\mathbf{r})|^2 \right], \quad (24)$$

where $\varepsilon(\mathbf{r})$ is the position dependent dielectric constant (38). Similar to the neutral polymer model, it is convenient to introduce volume fractions $\phi_\alpha(\mathbf{r}) = \frac{\rho_\alpha(\mathbf{r})}{\rho_\circ}$ for the polymers and counter ions. Here, ρ_\circ is the reference density and $\alpha = A, B$ and I . Also, we define the volume fraction for the charged species as $\phi_e(\mathbf{r}) = \frac{\rho_e(\mathbf{r})}{e\rho_\circ}$. The average volume fraction for the polymers and counter ions are defined as $\bar{\phi}_{AB} = \frac{n_{AB}N_{AB}}{\rho_\circ\Omega}$ and $\bar{\phi}_I = \frac{n_I}{\rho_\circ\Omega}$, respectively. Furthermore, we define a dimensionless electrostatic potential $\tilde{V}(\mathbf{r}) = \frac{eV(\mathbf{r})}{k_B T}$ and a dimensionless dielectric constant $\tilde{\varepsilon}(\mathbf{r}) = \frac{\varepsilon(\mathbf{r})}{\varepsilon_\circ}$. We assume that the position dependent dielectric constant $\tilde{\varepsilon}(\mathbf{r})$ is a function of polymer densities and can be written as $\tilde{\varepsilon}(\mathbf{r}) = \kappa_A \phi_A(\mathbf{r}) + \kappa_B \phi_B(\mathbf{r})$, where κ_A and κ_B are the dielectric constants of the A and B polymer species (25, 38).

The particle to field transformation follows a similar procedure to that described in Eq.6, where we introduce auxiliary fields that couple to the configuration dependent densities. Using the definition for the polymer and counter ion volume fractions and the dimensionless electrostatic potential, the particle to field transformation results in,

$$Z = \int D[\phi_\alpha(\mathbf{r})] D[\omega_\alpha(\mathbf{r})] D[\tilde{V}(\mathbf{r})] D[\eta(\mathbf{r})] \exp \left[-F[\omega_\alpha(\mathbf{r}), \phi_\alpha(\mathbf{r}), \tilde{V}(\mathbf{r}), \eta(\mathbf{r})] \right], \quad (25)$$

where $F[\omega_\alpha(\mathbf{r}), \phi_\alpha(\mathbf{r}), \tilde{V}(\mathbf{r}), \eta(\mathbf{r})]$ is the free energy functional of the system. Similar to the neutral polymer model, it is convenient to define a free energy density functional per chain $f[\omega_\alpha(\mathbf{r}), \phi_\alpha(\mathbf{r}), \tilde{V}(\mathbf{r}), \eta(\mathbf{r})] = \frac{N_{AB}}{\rho_o k_B T \Omega} F[\omega_\alpha(\mathbf{r}), \phi_\alpha(\mathbf{r}), \tilde{V}(\mathbf{r}), \eta(\mathbf{r})]$, such that,

$$\begin{aligned} f[\omega_\alpha(\mathbf{r}), \phi_\alpha(\mathbf{r}), \eta(\mathbf{r})] = & \frac{1}{\Omega} \int d\mathbf{r} \left\{ \frac{1}{2} \sum_{\alpha\beta=A,B,I} \phi_\alpha(\mathbf{r}) \chi_{\alpha\beta} N_{AB} \phi_\beta(\mathbf{r}) - \sum_{\alpha=A,B,I} \omega_\alpha(\mathbf{r}) \phi_\alpha(\mathbf{r}) \right. \\ & - e\omega_e(\mathbf{r}) \phi_e(\mathbf{r}) + \phi_e(\mathbf{r}) N_{AB} \tilde{V}(\mathbf{r}) - \frac{2\pi N_{AB} b^2 \tilde{\epsilon}(\mathbf{r})}{\tau} |\nabla \tilde{V}(\mathbf{r})|^2 \\ & \left. + \eta(\mathbf{r}) \left(\sum_{\alpha=A,B,I} \phi_\alpha(\mathbf{r}) - 1 \right) \right\} - \bar{\phi}_{AB} \ln\left(\frac{Q_{AB}}{\bar{\phi}_{AB}}\right) - N_{AB} \bar{\phi}_I \ln\left(\frac{Q_I}{\bar{\phi}}\right). \end{aligned} \quad (26)$$

In the above equation, the following scaling is performed; $N_{AB} \omega_\alpha(\mathbf{r}) \rightarrow \omega_\alpha(\mathbf{r})$ for $\alpha = A, B$ and I , and $N_{AB} e \omega_e(\mathbf{r}) \rightarrow e \omega_e(\mathbf{r})$. We have also introduced a new parameter τ , which takes into account the fact that there are two length scales in play (25). First is the length scale associated with the size of the monomer segments, set by the Kuhn length, b . The second is due to the electrostatic interactions between the charged species. This length scale can be characterized using the Bjerrum length l_B , which is the length at which the electrostatic interactions are the same strength as the thermal fluctuations (5, 25). The τ parameter can be written as,

$$\tau = \frac{4\pi \rho_o b^2 e^2}{k_B T \epsilon_o}. \quad (27)$$

If we define the the Bjerrum length as $l_B = \frac{e^2}{\epsilon_o k_B T}$ and assume $\rho_o = \frac{1}{4\pi b^3}$, then τ is the ratio between the Bjerrum length and the Kuhn length of the polymers, $\tau = \frac{l_B}{b}$.

In Eq.26, Q_{AB} and Q_I are the single chain and single molecule partition functions which can be written as,

$$\begin{aligned} Q_{AB} = & \frac{1}{\Omega} \int D[\mathbf{R}_i^A(s)] \int D[\mathbf{R}_i^B(s)] \delta[\mathbf{R}_i^A(f) - \mathbf{R}_i^B(1-f)] \\ & \exp\left[-\frac{3}{2b^2} \sum_{\alpha=A,B} \int ds \left(\frac{d\mathbf{R}_i^\alpha(s)}{ds}\right)^2 - \int_0^f ds \omega_A^{\text{eff}}(\mathbf{R}_i^A(s), s) - \int_f^1 ds \omega_B(\mathbf{R}_i^B(s))\right], \end{aligned} \quad (28)$$

$$Q_I = \frac{1}{\Omega} \int d\mathbf{r} \exp\left[-\omega_I^{\text{eff}}(\mathbf{r})\right]. \quad (29)$$

Here, $\omega_A^{\text{eff}}(\mathbf{R}_i^A(s), s)$ and $\omega_I^{\text{eff}}(\mathbf{r})$ are the effective auxiliary fields for the A and I species (25). We define the effective auxiliary fields as,

$$\begin{aligned}\omega_A^{\text{eff}}(\mathbf{r}, s) &= \omega_A(\mathbf{r}) - \ln \left[\sum_{c_A(s)} P_A(c_A(s), s) \exp \left(-c_A(s) z_A e \omega_e(\mathbf{r}) \right) \right], \\ \omega_I^{\text{eff}}(\mathbf{r}) &= \omega_I(\mathbf{r}) + z_I e \omega_e(\mathbf{r}),\end{aligned}\quad (30)$$

where $\sum_{c_A(s)} P_A(c_A(s), s)$ sums over all possible charge distributions $c_A(s)$ each with a probability $P_A(c_A(s), s)$ (25). In the model presented here, we consider the case where the negative charges are smeared on the A blocks, such that the amount of charge on the s^{th} monomer of the i^{th} chain is given by $c_{A,i}(s) z_A e$ (25, 26). In general, the probability of a particular charge distribution is given by $P(c_{A,i}(s)) = \prod_s p(c_{A,i}(s), s)$. If we assume that charges are fixed and smeared on the A blocks, then we can write $p(c_{A,i}(s)) = \delta(c_{A,i}(s) - P_A)$, where P_A assumes a value between 0 and 1. Using the above description, we can write $\omega_A^{\text{eff}}(\mathbf{r}, s)$ as,

$$\omega_A^{\text{eff}}(\mathbf{r}) = \omega_A(\mathbf{r}) + P_A z_A e \omega_e(\mathbf{r}). \quad (31)$$

Given the above definition for the $\omega_A^{\text{eff}}(\mathbf{r})$ fields, we write the single chain partition function for the AB diblock copolymers as,

$$\begin{aligned}Q_{AB} &= \frac{1}{\Omega} \int D[\mathbf{R}_i^A(s)] \int D[\mathbf{R}_i^B(s)] \delta[\mathbf{R}_i^A(f) - \mathbf{R}_i^B(1-f)] \exp \left[-\frac{3}{2b^2} \sum_{\alpha=A,B} \int ds \left(\frac{d\mathbf{R}_i^\alpha(s)}{ds} \right)^2 \right. \\ &\quad \left. - \int_0^f ds (\omega_A(\mathbf{r}) + P_A z_A e \omega_e(\mathbf{r})) - \int_f^1 ds \omega_B(\mathbf{R}_i^B(s)) \right].\end{aligned}\quad (32)$$

Similar to the SCFT model for neutral polymers, the solutions to the partition function are determined using the mean field (saddle point) approximation, where we minimize the free energy functional density $f[\omega_\alpha(\mathbf{r}), \phi_\alpha(\mathbf{r}), \tilde{V}(\mathbf{r}), \eta(\mathbf{r})]$ with respect to the $\phi_\alpha(\mathbf{r})$, $\omega_\alpha(\mathbf{r})$, $\tilde{V}(\mathbf{r})$ and $\eta(\mathbf{r})$ auxiliary fields. Evaluating the functional derivatives with respect to the $\omega_\alpha(\mathbf{r})$ fields results in the mean field equations for the polymer and counter ion densities,

$$\begin{aligned}\phi_A(\mathbf{r}) &= \frac{\bar{\Phi}_{AB}}{Q_{AB}} \int_0^f ds q_A(\mathbf{r}) q_A^\dagger(\mathbf{r}, f-s), \\ \phi_B(\mathbf{r}) &= \frac{\bar{\Phi}_{AB}}{Q_{AB}} \int_f^1 ds q_B(\mathbf{r}) q_B^\dagger(\mathbf{r}, 1-s), \\ \phi_I(\mathbf{r}) &= \frac{\bar{\Phi}_I}{Q_I} \exp \left[-\frac{1}{N_{AB}} \omega_I^{\text{eff}}(\mathbf{r}) \right].\end{aligned}\quad (33)$$

The forward and complementary propagators satisfy the modified diffusion equations similar to those in Eq.16. For the A species however, the modified diffusion equations are slightly different and contain the effective $\omega_A^{\text{eff}}(\mathbf{r})$ auxiliary fields,

$$\begin{aligned}\frac{\partial}{\partial s} q_A(\mathbf{r}, s) &= \left[\nabla^2 - \omega_A^{\text{eff}}(\mathbf{r}) \right] q_A(\mathbf{r}, s), \\ \frac{\partial}{\partial s} q_A^\dagger(\mathbf{r}, s) &= - \left[\nabla^2 - \omega_A^{\text{eff}}(\mathbf{r}) \right] q_A^\dagger(\mathbf{r}, s),\end{aligned}\quad (34)$$

where the effective auxiliary fields are given by Eq.31. Calculating the functional derivatives $\frac{\delta f}{\delta \phi_\alpha}$ results in the following mean field equations for the $\omega_\alpha(\mathbf{r})$ fields,

$$\begin{aligned}\omega_A(\mathbf{r}) &= \chi_{AB} N_{AB} \phi_B(\mathbf{r}) + \chi_{AI} N_{AB} \phi_I(\mathbf{r}) + \eta(\mathbf{r}) - \frac{12\pi\kappa_A}{\tau} |\nabla\tilde{V}(\mathbf{r})|^2, \\ \omega_B(\mathbf{r}) &= \chi_{AB} N_{AB} \phi_A(\mathbf{r}) + \chi_{BI} N_{AB} \phi_I(\mathbf{r}) + \eta(\mathbf{r}) - \frac{12\pi\kappa_B}{\tau} |\nabla\tilde{V}(\mathbf{r})|^2, \\ \omega_I(\mathbf{r}) &= \chi_{AI} N_{AB} \phi_A(\mathbf{r}) + \chi_{BI} N_{AB} \phi_B(\mathbf{r}), \\ e\omega_e(\mathbf{r}) &= N_{AB} \tilde{V}(\mathbf{r}).\end{aligned}\quad (35)$$

And lastly, evaluating the functional derivative of Eq.26 with respect to the electrostatic potential $\tilde{V}(\mathbf{r})$ results in the Poisson equation,

$$\nabla \cdot \left[\tilde{\epsilon}(\mathbf{r}) \nabla \tilde{V}(\mathbf{r}) \right] = - \frac{N_{AB}\tau}{24\pi} \phi_e(\mathbf{r}), \quad (36)$$

which is solved for a given charge distribution $\phi_e(\mathbf{r})$ to determine the electrostatic potential $\tilde{V}(\mathbf{r})$. Using the mean field solutions to equations 33-36, we write free energy of the charged AB diblock copolymers as,

$$\begin{aligned}f_{MF}[\omega_\alpha(\mathbf{r}), \phi_\alpha(\mathbf{r}), \tilde{V}(\mathbf{r})] &= \frac{1}{\Omega} \int d\mathbf{r} \left\{ \frac{1}{2} \sum_{\alpha\beta=A,B,I} \phi_\alpha(\mathbf{r}) \chi_{\alpha\beta} \phi_\beta(\mathbf{r}) - \sum_{\alpha=A,B,I} \omega_\alpha(\mathbf{r}) \phi_\alpha(\mathbf{r}) \right. \\ &\quad \left. - e\omega_e(\mathbf{r}) \phi_e(\mathbf{r}) + \phi_e(\mathbf{r}) N_{AB} \tilde{V}(\mathbf{r}) - \frac{2\pi N_{AB} b^2 \tilde{\epsilon}(\mathbf{r})}{\tau} |\nabla \tilde{V}(\mathbf{r})|^2 \right\} \\ &\quad - \bar{\phi}_{AB} \ln\left(\frac{Q_{AB}}{\bar{\phi}_{AB}}\right) - N_{AB} \bar{\phi}_I \ln\left(\frac{Q_I}{\bar{\phi}}\right).\end{aligned}\quad (37)$$

2.3 BLOCK COPOLYMERS IN CONFINEMENT

In confined geometries, such as polymer thin films and polymers near surfaces, one must consider the boundary effects on the properties of the system (10, 39–41). Based on our description of the polymer melts

for both neutral and charged polymers, the properties of the polymer densities are dictated according to the incompressibility condition (42). However, the incompressibility condition, $\sum_{\alpha} \phi_{\alpha}(\mathbf{r}) = 1$, does not hold near the boundaries. At the boundaries, the density of polymers must fall to zero (42). To take into account the boundary effects, we redefine the incompressibility condition such that,

$$\sum_{\alpha} \phi_{\alpha}(\mathbf{r}) = \Phi(\mathbf{r}), \quad (38)$$

where $\Phi(\mathbf{r})$ is written as,

$$\Phi(\mathbf{r}) = \begin{cases} \frac{1}{2} [1 - \cos(\frac{\pi x}{\Delta})] & 0 \leq x \leq \Delta \\ 1 & \Delta \leq x \leq L - \Delta \\ \frac{1}{2} [1 - \cos(\frac{\pi(L-x)}{\Delta})] & L - \Delta \leq x \leq L \end{cases}$$

Here, we assume that the system is confined in the x direction, and the distance between the two plates confining the polymers is L . Furthermore, Δ describes the distance from the wall where the polymer densities will rise to the bulk value of 1. This distance is much smaller than the radius of gyration of the polymers, $\Delta \ll bN^{1/2}$. The boundary effects are shown schematically in Figure 5. In Figure 5.b we can see that the density of polymers falls sharply to zero at the boundaries.

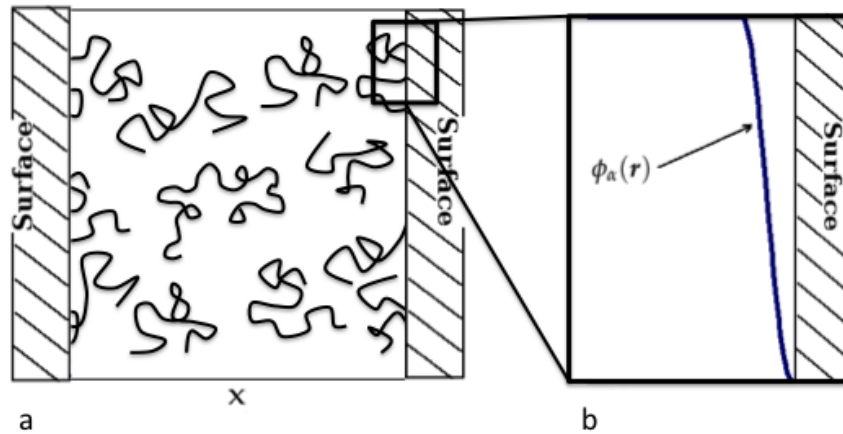


Figure 5: Figure a) shows a schematic diagram of a polymeric system in confinement, and b) shows the effect of confinement on the density of polymers near the surfaces.

It is also important to consider and take into account the interactions of polymers with various surfaces.

For example, in an AB diblock copolymer system, the A and B blocks could interact differently with the substrate or air surfaces (43). To model the polymer surface interactions, we introduce a function $h(\mathbf{r})$ which describes the strength of the interactions between polymers and surfaces. We define $h(\mathbf{r})$ such that,

$$h(\mathbf{r}) = \begin{cases} \frac{4R_g\sigma_1}{\Delta} [1 + \cos(\frac{\pi x}{\Delta})] & 0 \leq x \leq \Delta \\ 0 & \Delta \leq x \leq L - \Delta \\ \frac{4R_g\sigma_2}{\Delta} [1 + \cos(\frac{\pi(L-x)}{\Delta})] & L - \Delta \leq x \leq L \end{cases}$$

where, σ_1 and σ_2 control the strength of the interactions of polymers with the two surfaces (42, 44). To capture the confinement effect in the SCFT model, we rewrite the free energy density functional of the neutral block copolymer system as,

$$f[\omega_\alpha(\mathbf{r}), \phi_\alpha(\mathbf{r}), \eta(\mathbf{r})] = \int d\mathbf{r} \left\{ \frac{1}{2} \sum_{\alpha\beta=A,B} \phi_\alpha(\mathbf{r}) \chi_{\alpha\beta} N_{AB} \phi_\beta(\mathbf{r}) - \sum_{\alpha=A,B} \omega_\alpha(\mathbf{r}) \phi_\alpha(\mathbf{r}) \right. \\ \left. \eta(\mathbf{r}) \left(\sum_{\alpha=A,B} \phi_\alpha(\mathbf{r}) - \Phi(\mathbf{r}) \right) - h(\mathbf{r}) [\phi_A(\mathbf{r}) - \phi_B(\mathbf{r})] \right\} - \bar{\phi}_{AB} \ln\left(\frac{\xi_{AB} Q_{AB} \Omega}{n_{AB}}\right). \quad (39)$$

Using the above free energy, we formulate the mean field solutions to partition function and write,

$$\begin{aligned} \phi_A(\mathbf{r}) &= \frac{\bar{\phi}_{AB}}{Q_{AB}} \int_0^f ds q_A(\mathbf{r}, s) q_A^\dagger(\mathbf{r}, f-s), \\ \phi_B(\mathbf{r}) &= \frac{\bar{\phi}_{AB}}{Q_{AB}} \int_f^1 ds q_B(\mathbf{r}, s) q_B^\dagger(\mathbf{r}, 1-s), \\ \omega_A(\mathbf{r}) &= \chi_{AB} N_{AB} \phi_B(\mathbf{r}) - h(\mathbf{r}) + \eta(\mathbf{r}), \\ \omega_B(\mathbf{r}) &= \chi_{AB} N_{AB} \phi_A(\mathbf{r}) + h(\mathbf{r}) + \eta(\mathbf{r}), \\ \sum_{\alpha=A,B} \phi_\alpha(\mathbf{r}) &= \Phi(\mathbf{r}), \end{aligned} \quad (40)$$

where the confinement effect is captured in the expression for the auxiliary fields $\omega_A(\mathbf{r})$ and $\omega_B(\mathbf{r})$ and the incompressibility condition $\eta(\mathbf{r})$.

3 | Numerical Methods

In the previous chapter, we presented a field theoretic framework for studying the equilibrium properties of polymeric systems. Although statistical field theories have been used extensively to study the thermodynamic properties of polymeric systems, analytical solutions to the partition functions of non-trivial models of polymeric systems are difficult to obtain (10, 45, 46). The most fruitful approach for extracting useful information about the thermodynamic properties of polymeric systems is a combination of analytical approximations and numerical techniques. As described previously, a powerful method for determining the solutions to the field theoretic partition function is the mean-field (saddle point) approximation (10).

The result of the mean-field approximation is a set of non-linear equations, which must be solved self-consistently to determine the equilibrium solutions. At the heart of the self-consistent field theory algorithm, lies the process of generating solutions to the modified diffusion equations (1). The solutions to the modified diffusion equations are the forward and complementary propagators, used to determine the mean-field densities of the polymers. A general algorithm for solving the mean fields equations, presented in Eq.16 and 17 in the previous chapter, can be described in the following way:

1. The first step is to initialize the $\omega_\alpha(\mathbf{r})$ fields. As a rule of thumb, the initial guess should resemble the morphology of the desired phase. For example, for the lamellae phase, a sine or cosine function can be used as the initial guess.
2. The $\omega_\alpha(\mathbf{r})$ fields are then used to solve the modified diffusion equations, with appropriate initial and boundary conditions.

$$\begin{aligned} \frac{\partial}{\partial s} q_\alpha(\mathbf{r}, s) &= [\nabla^2 - \omega_\alpha(\mathbf{r})] q_\alpha(\mathbf{r}, s) \\ \frac{\partial}{\partial s} q_\alpha^\dagger(\mathbf{r}, s) &= -[\nabla^2 - \omega_\alpha(\mathbf{r})] q_\alpha^\dagger(\mathbf{r}, s) \end{aligned} \tag{41}$$

3. The solutions to the above modified diffusion equations are used to evaluate the density field, $\phi_\alpha(\mathbf{r})$. For example, for the AB diblock copolymers we calculate $\phi_A(\mathbf{r})$ and $\phi_B(\mathbf{r})$ using the following equations,

$$\begin{aligned}\phi_A(\mathbf{r}) &= \frac{\bar{\Phi}_{AB}}{Q_{AB}} \int_0^f ds q_A(\mathbf{r}, s) q_A^\dagger(\mathbf{r}, f-s) \\ \phi_B(\mathbf{r}) &= \frac{\bar{\Phi}_{AB}}{Q_{AB}} \int_f^1 ds q_B(\mathbf{r}, s) q_B^\dagger(\mathbf{r}, 1-s)\end{aligned}\quad (42)$$

4. Using $\phi_\alpha(\mathbf{r})$, the incompressibility condition ($\sum_{\alpha=A,B} \phi_\alpha(\mathbf{r}) = 1$) is evaluated and $\eta(\mathbf{r})$ is updated.
5. For a given set of $\chi_{\alpha\beta}$, $\phi_\alpha(\mathbf{r})$ and $\eta(\mathbf{r})$, the $\omega_\alpha(\mathbf{r})$ fields are calculated.

$$\begin{aligned}\omega_A(\mathbf{r}) &= \chi_{AB} N_{AB} \phi_B(\mathbf{r}) + \eta(\mathbf{r}) \\ \omega_B(\mathbf{r}) &= \chi_{AB} N_{AB} \phi_A(\mathbf{r}) + \eta(\mathbf{r})\end{aligned}\quad (43)$$

6. The convergence condition $\delta\theta \equiv |\theta^i - \theta^{i-1}|$ is calculated at every iteration step i . Here, $\delta\theta = \{\delta\phi, \delta\omega, \delta F\}$. If $\delta\theta < \varepsilon$, where ε is a convergence criteria, then the mean field solutions are found. If not, we proceed with step 2 and repeat this process until the convergence criteria are met.

There are numerous classes of numerical techniques which can be used to implement the above algorithm (47–50). The choice for the appropriate technique relies on a number of different factors such as accuracy, computational efficiency and the ease of use based on the properties of the specific model (47). In this chapter, we will examine in detail two numerical methods; the pseudo spectral method and a finite difference technique known as the alternating direction implicit (ADI) method.

3.1 PSEUDO SPECTRAL METHOD

In this section, we will examine in detail the pseudo spectral method for solving the modified diffusion equations. The pseudo spectral technique is a powerful and accurate numerical method for solving partial differential equations (51–53). It takes advantage of the best aspects of the real and reciprocal space, allowing for a robust and flexible approach for solving the modified diffusion equations. The pseudo spectral technique is most useful for models which are periodic in nature and thus plays an important role in the

solving of inhomogeneous polymeric systems (10).

For the purpose of our discussion, we will focus on the application of the pseudo spectral technique for solving a one dimensional modified diffusion equation. The extension of our description to two and three dimensions is straight forward. The modified diffusion equation as described in chapter 2 can be written as,

$$\frac{\partial q(x,s)}{\partial s} = \left[\frac{\partial^2}{\partial x^2} - \omega(x) \right] q(x,s), \quad (44)$$

where $q(x,s)$ is the forward propagator and $\omega(x)$ is the chemical potential field. The numerical recipe presented here will also apply to the modified diffusion equation for the complementary propagators $q^\dagger(x,s)$.

The challenge here is to determine the solution to the above differential equation for given $\omega(x)$. The general idea is to approximate the solution to the differential equation using a finite sum of basis functions (51). The pseudo spectral method assumes that a continuous well-behaved function $f(x)$ can be written in terms of set of orthogonal basis functions $g(x)$ in the following form (51),

$$f(x) \approx f_M(x) = \sum_{n=0}^{M-1} a_n g_n(x). \quad (45)$$

Here, $f_M(x)$ is the approximated solution and a_n are the expansion coefficients. Furthermore, we enforce the condition such that the approximate solution $f_M(x)$ agrees with the exact solution $f(x)$ at a set of M collocation points x_n with $n=0, 1, 2, \dots, M-1$ (51). In the case of the propagators, we write,

$$q_M(x,s) = \sum_{n=0}^{M-1} a_n(s) \psi_n(x), \quad (46)$$

where we enforce the condition $q_M(x_n,s) = q(x_n,s)$ for x_n with $n=0, 1, 2, \dots, M-1$ (10). In the above expression, $\psi(x)$ are the basis functions, which satisfy the same boundary condition as $q(x,s)$. For linear Gaussian homopolymers, the modified diffusion equation Eq.44 is solved using the initial condition $q(x,0) = 1$. The boundary conditions however depend on the specifics of the model system. For example, in the case of confined or grafted polymers, one might demand specific restrictions on one or more boundaries. The choice for the boundary conditions determines the basis functions used in equation 46.

In the case of periodic boundary condition, the basis functions are planes waves,

$$q_M(x,s) = \sum_{n=0}^{M-1} a_n(s) \exp\left[\frac{i2\pi x n}{L}\right], \quad (47)$$

where, L is the length of the computational box (10). In scenarios where we require $q_M(x = 0, s) = 0$ and $q_M(x = M - 1, s) = 0$, Dirichlet boundary condition is used, leading to the expansion,

$$q_M(x, s) = \sum_{n=0}^{n=M-1} a_n(s) \sin\left[\frac{\pi nx}{L}\right], \quad (48)$$

where the basis functions $\psi_n(x)$ are the *sine* series expansion (10). Furthermore, in scenarios where one requires $\frac{dq(x,s)}{dx}|_{x=0} = 0$ and $\frac{dq(x,s)}{dx}|_{x=M-1} = 0$, Neumann boundary condition is used, leading to,

$$q_M(x, s) = \sum_{n=0}^{n=M-1} a_n(s) \cos\left[\frac{\pi nx}{L}\right]. \quad (49)$$

In this case, the basis functions $\psi_n(x)$ are the *cosine* series expansion (10). To solve the modified diffusion equations, we introduce a linear operator \mathcal{L} , defined as,

$$\mathcal{L} \equiv \frac{\partial^2}{\partial x^2} - \omega(x), \quad (50)$$

where \mathcal{L} is non-local in both real and reciprocal space (51). Using the above operator, the value of the propagator at any point along the contour of the chain can be determined using,

$$q(x, s + \Delta s) = e^{\mathcal{L}\Delta s} q(x, s), \quad (51)$$

where Δs is a small contour step along the backbone of the chain. Using the Taylor expansion in Δs , we can split the operator in terms of its diffusive and potential contribution; $\mathcal{L} = \mathcal{L}^D + \mathcal{L}^\omega$, and write,

$$\exp[\mathcal{L}\Delta s] = \exp\left[-\frac{\omega(x)\Delta s}{2}\right] \exp\left[\frac{\partial^2}{\partial x^2}\Delta s\right] \exp\left[-\frac{\omega(x)\Delta s}{2}\right] + \mathcal{O}(\Delta s^3). \quad (52)$$

The solution to the modified diffusion equation, based on the above expansion, can be written as,

$$q(x, s + \Delta s) = \left\{ \exp\left[-\frac{\omega(x)\Delta s}{2}\right] \exp\left[\frac{\partial^2}{\partial x^2}\Delta s\right] \exp\left[-\frac{\omega(x)\Delta s}{2}\right] \right\} q(x, s). \quad (53)$$

For our one dimensional model, we can discretize the spatial domain and contour-length of the polymer chains such that,

$$q(x, s) \rightarrow q[m, n], \quad (54)$$

where,

$$\begin{aligned} n = 0, 1, 2, \dots, N_s - 1 \quad s \in [0, N] \quad s_n = n\Delta s \quad \Delta s = \frac{N}{N_s - 1}, \\ m = 0, 1, 2, \dots, N_x - 1 \quad x \in [0, L] \quad x_m = m\Delta x \quad \Delta x = \frac{L}{N_x - 1}. \end{aligned} \quad (55)$$

Using the discrete representation of the propagator $q[m, n]$, we can rewrite Eq.53 in the matrix form such that,

$$\begin{bmatrix} q[0, n+1] \\ q[1, n+1] \\ \cdot \\ \cdot \\ q[N_x - 1, n+1] \end{bmatrix} = \begin{bmatrix} W_{0,0} & 0 & \cdot & \cdot & \cdot & 0 \\ 0 & W_{1,1} & \cdot & \cdot & \cdot & \cdot \\ \cdot & \cdot & \cdot & \cdot & \cdot & \cdot \\ \cdot & \cdot & \cdot & \cdot & \cdot & 0 \\ 0 & \cdot & \cdot & \cdot & 0 & W_{N_x-1, N_x-1} \end{bmatrix} \begin{bmatrix} D_{0,0} & \cdot & \cdot & \cdot & \cdot & D_{N_x-1,0} \\ \cdot & \cdot & \cdot & \cdot & \cdot & \cdot \\ \cdot & \cdot & \cdot & \cdot & \cdot & \cdot \\ \cdot & \cdot & \cdot & \cdot & \cdot & \cdot \\ \cdot & \cdot & \cdot & \cdot & \cdot & \cdot \\ D_{0, N_x-1} & \cdot & \cdot & \cdot & \cdot & D_{N_x-1, N_x-1} \end{bmatrix} \quad (56)$$

$$\begin{bmatrix} W_{0,0} & 0 & \cdot & \cdot & \cdot & 0 \\ 0 & W_{1,1} & \cdot & \cdot & \cdot & \cdot \\ \cdot & \cdot & \cdot & \cdot & \cdot & \cdot \\ \cdot & \cdot & \cdot & \cdot & \cdot & \cdot \\ \cdot & \cdot & \cdot & \cdot & 0 & \cdot \\ 0 & \cdot & \cdot & \cdot & 0 & W_{N_x-1, N_x-1} \end{bmatrix} \begin{bmatrix} q[0, n] \\ q[1, n] \\ \cdot \\ \cdot \\ \cdot \\ q[N_x - 1, n] \end{bmatrix}$$

The elements of the above matrices are written based on the definition of the diffusive and potential operators. For simplicity, we write the above matrices in the following form,

$$q_m^{n+1} = \mathbf{W} \mathbf{D} \mathbf{W} q_m^n, \quad (57)$$

where q_m^{n+1} and q_m^n are vectors and \mathbf{W} and \mathbf{D} are matrices. It is important to note that the \mathbf{W} matrices are diagonal and thus would only require $N_x - 1$ multiplication (10). The \mathbf{D} matrix however is not diagonal in real space. The unique feature of the pseudo spectral method is that it takes advantage of the reciprocal

representation of the diffusion operator. In the reciprocal space, the \mathbf{D} matrix is diagonal. To take advantage of this property, we leverage the Fourier transform and inverse transform pairs $(\mathcal{F}, \mathcal{F}^\dagger)$ and write,

$$q_m^{n+1} = \mathbf{W} \mathcal{F} \mathcal{F}^\dagger \mathbf{D} \mathcal{F} \mathcal{F}^\dagger \mathbf{W} q_m^n. \quad (58)$$

By performing the operations in the above expression in the correct order, one could solve the modified diffusion equation for a single contour step. Based on Eq.58, the pseudo spectral algorithm can be written as:

1. The first step is to perform the $N_x - 1$ multiplication between the diagonal \mathbf{W} matrix and the q_m^n vector, resulting in: $p_m^n = \mathbf{W} q_m^n$, where p_m^n is a $N_x - 1 \times 1$ dimensional vector.
2. Then, Fourier transform of the p_m^n vector is computed, resulting in: $\bar{p}_m^n = \mathcal{F}^\dagger p_m^n$.
3. The Fourier representation of the diffusion operator matrix, \mathbf{D} , is computed. This step results in: $\bar{\mathbf{D}} = \mathcal{F}^\dagger \mathbf{D} \mathcal{F}$. In the reciprocal space, the $\bar{\mathbf{D}}$ matrix is diagonal.
4. The next step is to compute the product of the $\bar{\mathbf{D}}$ matrix and \bar{p}_m^n vector, which in the reciprocal space would only require $N_x - 1$ multiplications. For simplicity we write this as: $\bar{d}_m^n = \bar{\mathbf{D}} \bar{p}_m^n$.
5. The next step is to perform the inverse Fourier transform on the vector \bar{d}_m^n . This step, transforms the \bar{d}_m^n vector into its real space representation.
6. The final step is to perform the $N_x - 1$ multiplication between the \mathbf{W} matrix and the $\mathcal{F} \bar{d}_m^n$ vector.

The above algorithm advances $q(x, s)$ one contour step Δs along the backbone of the polymer chain. Repeating the above algorithm $N_s - 1$ times, computes the solution to the modified diffusion equation Eq.44. The pseudo spectral method described here is performed in step 2 of the general algorithm defined at the beginning of this chapter.

3.2 ALTERNATING DIRECTION IMPLICIT METHOD

In this section, we present a detailed description of the alternating direction implicit (ADI) method. The ADI method is in the family of finite difference (FD) techniques, similar to the Crank-Nicolson and the simple

implicit methods (10, 54, 55). The advantage of the ADI technique in comparison with other FD methods is that it provides a simpler method for solving two and three dimensional differential equations (56). In this section, we use the ADI method to solve the modified diffusion equation Eq 59. Similar to other Finite-Difference techniques, the differential equation is sampled at discrete points inside the computational box (10, 55). The advantage of using Finite Difference techniques, including ADI, is that the modified diffusion equation can be solved rather easily in a number of different coordinate systems (30, 57). To showcase this, we construct the SCFT framework using the cylindrical geometry, and solve the diffusion equations using the ADI method. We start with the generic modified diffusion equation,

$$\frac{\partial q(\mathbf{r}, s)}{\partial s} = \nabla^2 q(\mathbf{r}, s) - \omega(\mathbf{r})q(\mathbf{r}, s), \quad (59)$$

where $q(\mathbf{r}, s)$ is the end-integrated propagator and $\omega(\mathbf{r})$ is the auxiliary field coupled to the polymer density. In eq 59, ∇^2 is the Laplacian operator, which could be written as,

$$\begin{aligned} \nabla^2 &\equiv \frac{\partial^2}{\partial x^2} + \frac{\partial^2}{\partial y^2} + \frac{\partial^2}{\partial z^2} \quad [\text{Cartesian coordinates}], \\ \nabla^2 &\equiv \frac{1}{r} \frac{\partial}{\partial r} \left(r \frac{\partial}{\partial r} \right) + \frac{1}{r^2} \frac{\partial^2}{\partial \theta^2} + \frac{\partial^2}{\partial z^2} \quad [\text{Cylindrical coordinates}], \\ \nabla^2 &\equiv \frac{1}{r^2} \frac{\partial}{\partial r} \left(r^2 \frac{\partial}{\partial r} \right) + \frac{1}{r^2 \sin^2 \phi} \frac{\partial^2}{\partial \theta^2} + \frac{1}{r^2 \sin \phi} \frac{\partial}{\partial \phi} \left(\sin \phi \frac{\partial}{\partial \phi} \right) \quad [\text{Spherical coordinates}]. \end{aligned} \quad (60)$$

For simplicity, we write the Laplacian operator in the following format; $\nabla^2 \equiv \nabla_1 + \nabla_2 + \nabla_3$, where $(\nabla_1, \nabla_2, \nabla_3)$ can be defined depending on the dimensionality and symmetry of the model. In this section, we consider a two dimensional system, where $\nabla^2 \equiv \nabla_1 + \nabla_2$. Using this notation, we can discretize the modified diffusion equation in two steps,

$$\frac{2}{\Delta s} [q_{ij}^{n+1/2} - q_{ij}^n] = \frac{b^2}{6} [\nabla_1 q_{ij}^{n+1/2} + \nabla_2 q_{ij}^n] - \frac{\omega_{ij}}{2} [q_{ij}^{n+1/2} + q_{ij}^n], \quad (61)$$

$$\frac{2}{\Delta s} [q_{ij}^{n+1} - q_{ij}^{n+1/2}] = \frac{b^2}{6} [\nabla_1 q_{ij}^{n+1/2} + \nabla_2 q_{ij}^{n+1}] - \frac{\omega_{ij}}{2} [q_{ij}^{n+1} + q_{ij}^{n+1/2}], \quad (62)$$

where i and j are indices running over each dimension. For the purpose of this derivation, we use the cylindrical coordinates, where,

$$\begin{aligned} \nabla_1 &\equiv \frac{1}{r} \frac{\partial}{\partial r} + \frac{\partial^2}{\partial r^2}, \\ \nabla_2 &\equiv \frac{\partial^2}{\partial z^2}. \end{aligned} \quad (63)$$

Applying the above operators to the modified diffusion equations 61 and 62 and solving for $q^{n+1/2}$ and q^{n+1} in terms of q^n and $q^{n+1/2}$, we arrive at,

$$\begin{aligned}
& q_{ij}^{n+1/2} - \frac{\Delta s b^2}{12} \left[\frac{1}{i\Delta r + R} \frac{q_{i+1j}^{n+1/2} - q_{i-1j}^{n+1/2}}{2\Delta r} + \frac{q_{i+1j}^{n+1/2} - 2q_{ij}^{n+1/2} + q_{i-1j}^{n+1/2}}{\Delta r^2} \right] + \frac{\Delta s \omega_{ij}}{4} q_{ij}^{n+1/2}, \\
& = \\
& q_{ij}^n + \frac{\Delta s b^2}{12} \frac{q_{ij+1}^n - 2q_{ij}^n + q_{ij-1}^n}{\Delta z^2} - \frac{\Delta s \omega_{ij}}{4} q_{ij}^n, \tag{64}
\end{aligned}$$

for the $n + 1/2$ step and,

$$\begin{aligned}
& q_{ij}^{n+1} - \frac{\Delta s b^2}{12} \frac{q_{ij+1}^{n+1} - 2q_{ij}^{n+1} + q_{ij-1}^{n+1}}{\Delta z^2} - \frac{\Delta s \omega_{ij}}{4} q_{ij}^{n+1}, \\
& = \\
& q_{ij}^{n+1/2} + \frac{\Delta s b^2}{12} \left[\frac{1}{i\Delta r + R} \frac{q_{i+1j}^{n+1/2} - q_{i-1j}^{n+1/2}}{2\Delta r} + \frac{q_{i+1j}^{n+1/2} - 2q_{ij}^{n+1/2} + q_{i-1j}^{n+1/2}}{\Delta r^2} \right] - \frac{\Delta s \omega_{ij}}{4} q_{ij}^{n+1/2}, \tag{65}
\end{aligned}$$

for the $n + 1$ step. In the above set of equations, R is the distance from the origin to the computational box. This is shown more clearly in Figure 6. Furthermore, Δr and Δz are calculated by discretizing the computational box with dimensions of L_r and L_z using N_r and N_z points. For simplicity, we assume $N_r = N_z = N$.

To simplify Eq.64 and 65, we introduce the following notation,

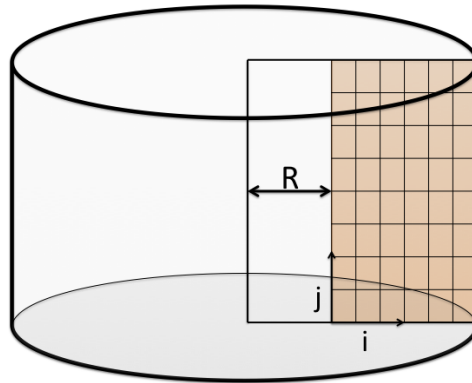


Figure 6: A schematic diagram of the computational box in the cylindrical geometry.

$$\begin{aligned}
\alpha_i &\equiv \frac{\Delta s b^2}{24\Delta r(i\Delta r + R)} - \frac{\Delta s b^2}{12\Delta r^2}, \\
\beta_{ij} &\equiv 1 + \frac{\Delta s \omega_{ij}}{4} + \frac{\Delta s b^2}{6\Delta r^2}, \\
\gamma_i &\equiv -\frac{\Delta s b^2}{24\Delta r(i\Delta r + R)} - \frac{\Delta s b^2}{12\Delta r^2}, \\
\theta &\equiv \frac{\Delta s b^2}{12\Delta z^2}, \\
\sigma_{ij} &\equiv 1 - \frac{\Delta s b^2}{6\Delta z^2} - \frac{\Delta s \omega_{ij}}{4},
\end{aligned} \tag{66}$$

for the $n + 1/2$ step and,

$$\begin{aligned}
\hat{\theta} &\equiv -\frac{\Delta s b^2}{12\Delta z^2}, \\
\hat{\sigma}_{ij} &\equiv 1 + \frac{\Delta s b^2}{6\Delta z^2} + \frac{\Delta s \omega_{ij}}{4}, \\
\hat{\alpha}_i &\equiv \frac{\Delta s b^2}{12\Delta r^2} - \frac{\Delta s b^2}{24\Delta r(i\Delta r + R)}, \\
\hat{\beta}_{ij} &\equiv 1 - \frac{\Delta s b^2}{6\Delta r^2} - \frac{\Delta s \omega_{ij}}{4}, \\
\hat{\gamma}_i &\equiv \frac{\Delta s b^2}{24\Delta r(i\Delta r + R)} + \frac{\Delta s b^2}{12\Delta r^2},
\end{aligned} \tag{67}$$

for the $n + 1$ step. Using the above notation, Equations 64 and 65 can be written as,

$$\alpha_i q_{i+1j}^{n+1/2} + \beta_{ij} q_{ij}^{n+1/2} + \gamma_i q_{i-1j}^{n+1/2} = \theta q_{ij-1}^n + \sigma_{ij} q_{ij}^n + \theta q_{ij+1}^n, \tag{68}$$

$$\hat{\theta} q_{ij-1}^{n+1} + \hat{\sigma}_{ij} q_{ij}^{n+1} + \hat{\theta} q_{ij+1}^{n+1} = \hat{\alpha}_i q_{i-1j}^{n+1/2} + \hat{\beta}_{ij} q_{ij}^{n+1/2} + \hat{\gamma}_i q_{i+1j}^{n+1/2}, \tag{69}$$

where we have not yet defined the boundary conditions. The choice of boundary condition depends on the specifics of the model system. In this thesis, we apply the ADI method to study the elastic properties of bilayer membranes, where the appropriate boundary condition is defined by setting $\nabla f=0$ at the boundaries.

We redefine the above set of equations using matrices, where we solve for $q^{n+1/2}$ in the range $0 < j < N - 1$ such that,

$$\begin{bmatrix} q_{0j}^{n+1/2} \\ q_{1j}^{n+1/2} \\ \cdot \\ \cdot \\ \cdot \\ q_{N-1j}^{n+1/2} \end{bmatrix} = \begin{bmatrix} \beta_{0j} & (\gamma_0 + \alpha_0) & 0 & \cdot & \cdot & 0 \\ \alpha_1 & \beta_{1j} & \gamma_1 & \cdot & \cdot & \cdot \\ 0 & \cdot & \cdot & \cdot & \cdot & \cdot \\ \cdot & \cdot & \cdot & \cdot & \cdot & \cdot \\ 0 & \cdot & \cdot & \alpha_{N-2} & \beta_{N-2j} & \gamma_{N-2} \\ 0 & \cdot & \cdot & \cdot & (\gamma_{N-1} + \alpha_{N-1}) & \beta_{N-1j} \end{bmatrix}^{-1} \begin{bmatrix} \theta q_{0j-1}^n + \sigma_{0j} q_{0j}^n + \theta q_{0j+1}^n \\ \theta q_{1j-1}^n + \sigma_{1j} q_{1j}^n + \theta q_{1j+1}^n \\ \cdot \\ \cdot \\ \cdot \\ \theta q_{N-1j-1}^n + \sigma_{N-1j} q_{N-1j}^n + \theta q_{N-1j+1}^n \end{bmatrix} \quad (70)$$

The boundary points at $j=0$ and $j=N-1$ are solved for in a similar format. For the case where $j=0$ we write,

$$\begin{bmatrix} q_{00}^{n+1/2} \\ q_{10}^{n+1/2} \\ \cdot \\ \cdot \\ \cdot \\ q_{N-10}^{n+1/2} \end{bmatrix} = \begin{bmatrix} \beta_{00} & (\gamma_0 + \alpha_0) & 0 & \cdot & \cdot & 0 \\ \alpha_1 & \beta_{10} & \gamma_1 & \cdot & \cdot & \cdot \\ 0 & \cdot & \cdot & \cdot & \cdot & \cdot \\ \cdot & \cdot & \cdot & \cdot & \cdot & \cdot \\ 0 & \cdot & \cdot & \alpha_{N-2} & \beta_{N-20} & \gamma_{N-2} \\ 0 & \cdot & \cdot & \cdot & (\gamma_{N-1} + \alpha_{N-1}) & \beta_{N-10} \end{bmatrix}^{-1} \begin{bmatrix} \sigma_{00}q_{00}^n + 2\theta q_{01}^n \\ \sigma_{10}q_{10}^n + 2\theta q_{11}^n \\ \cdot \\ \cdot \\ \cdot \\ \sigma_{N-10}q_{N-10}^n + 2\theta q_{N-11}^n \end{bmatrix} \quad (71)$$

and similarly for $j=N-1$,

$$\begin{bmatrix} q_{0N-1}^{n+1/2} \\ q_{1N-1}^{n+1/2} \\ \cdot \\ \cdot \\ \cdot \\ q_{N-1N-1}^{n+1/2} \end{bmatrix} = \begin{bmatrix} \beta_{0N-1} & (\gamma_0 + \alpha_0) & 0 & \cdot & \cdot & 0 \\ \alpha_1 & \beta_{1N-1} & \gamma_1 & \cdot & \cdot & \cdot \\ 0 & \cdot & \cdot & \cdot & \cdot & \cdot \\ \cdot & \cdot & \cdot & \cdot & \cdot & \cdot \\ 0 & \cdot & \cdot & \alpha_{N-2} & \beta_{N-2N-1} & \gamma_{N-2} \\ 0 & \cdot & \cdot & \cdot & (\gamma_{N-1} + \alpha_{N-1}) & \beta_{N-1N-1} \end{bmatrix}^{-1} \begin{bmatrix} 2\theta q_{0N-2}^n + \sigma_{0N-1}q_{0N-1}^n \\ 2\theta q_{1N-2}^n + \sigma_{1N-1}q_{1N-1}^n \\ \cdot \\ \cdot \\ \cdot \\ 2\theta q_{N-1N-2}^n + \sigma_{N-1N-1}q_{N-1N-1}^n \end{bmatrix} \quad (72)$$

In the above matrices, we have implemented the Neumann boundary condition. Similar to $q^{n+1/2}$, we can solve for q^{n+1} in the range $0 < i < N - 1$ such that,

$$\begin{bmatrix} q_{i0}^{n+1} \\ q_{i1}^{n+1} \\ \cdot \\ \cdot \\ q_{iN-1}^{n+1} \end{bmatrix} = \begin{bmatrix} \hat{\sigma}_{i0} & 2\hat{\theta} & 0 & \cdot & \cdot & 0 \\ \hat{\theta} & \hat{\sigma}_{i1} & \hat{\theta} & \cdot & \cdot & \cdot \\ 0 & \cdot & \cdot & \cdot & \cdot & \cdot \\ \cdot & \cdot & \cdot & \cdot & \cdot & \cdot \\ 0 & \cdot & \cdot & \hat{\theta} & \hat{\sigma}_{iN-2} & \hat{\theta} \\ 0 & \cdot & \cdot & \cdot & 2\hat{\theta} & \hat{\sigma}_{iN-1} \end{bmatrix}^{-1} \begin{bmatrix} \hat{\alpha}_i q_{i-10}^{n+1/2} + \hat{\beta}_{i0} q_{i0}^{n+1/2} + \hat{\gamma}_i q_{i+10}^{n+1/2} \\ \hat{\alpha}_i q_{i-11}^{n+1/2} + \hat{\beta}_{i1} q_{i1}^{n+1/2} + \hat{\gamma}_i q_{i+11}^{n+1/2} \\ \cdot \\ \cdot \\ \hat{\alpha}_i q_{i-1N-1}^{n+1/2} + \hat{\beta}_{iN-1} q_{iN-1}^{n+1/2} + \hat{\gamma}_i q_{i+1N-1}^{n+1/2} \end{bmatrix} \quad (73)$$

And for boundary points at $i=0$ we write,

$$\begin{bmatrix} q_{00}^{n+1} \\ q_{01}^{n+1} \\ \cdot \\ \cdot \\ q_{0N-1}^{n+1} \end{bmatrix} = \begin{bmatrix} \hat{\sigma}_{00} & 2\hat{\theta} & 0 & \cdot & \cdot & 0 \\ \hat{\theta} & \hat{\sigma}_{01} & \hat{\theta} & \cdot & \cdot & \cdot \\ 0 & \cdot & \cdot & \cdot & \cdot & \cdot \\ \cdot & \cdot & \cdot & \cdot & \cdot & \cdot \\ 0 & \cdot & \cdot & \hat{\theta} & \hat{\sigma}_{0N-2} & \hat{\theta} \\ 0 & \cdot & \cdot & \cdot & 2\hat{\theta} & \hat{\sigma}_{0N-1} \end{bmatrix}^{-1} \begin{bmatrix} \hat{\beta}_{00} q_{00}^{n+1/2} + (\hat{\alpha}_0 + \hat{\gamma}_0) q_{10}^{n+1/2} \\ \hat{\beta}_{01} q_{01}^{n+1/2} + (\hat{\alpha}_0 + \hat{\gamma}_0) q_{11}^{n+1/2} \\ \cdot \\ \cdot \\ \hat{\beta}_{0N-1} q_{0N-1}^{n+1/2} + (\hat{\alpha}_0 + \hat{\gamma}_0) q_{1N-1}^{n+1/2} \end{bmatrix} \quad (74)$$

And lastly, for $i=N-1$ we write,

$$\begin{bmatrix} q_{N-10}^{n+1} \\ q_{N-11}^{n+1} \\ \cdot \\ \cdot \\ q_{N-1N-1}^{n+1} \end{bmatrix} = \begin{bmatrix} \hat{\sigma}_{N-10} & 2\hat{\theta} & 0 & \cdot & \cdot & 0 \\ \hat{\theta} & \hat{\sigma}_{N-11} & \hat{\theta} & \cdot & \cdot & \cdot \\ 0 & \cdot & \cdot & \cdot & \cdot & \cdot \\ \cdot & \cdot & \cdot & \cdot & \cdot & \cdot \\ 0 & \cdot & \cdot & \hat{\theta} & \hat{\sigma}_{N-1N-2} & \hat{\theta} \\ 0 & \cdot & \cdot & \cdot & 2\hat{\theta} & \hat{\sigma}_{N-1N-1} \end{bmatrix}^{-1} \begin{bmatrix} \hat{\beta}_{N-10}q_{N-10}^{n+1/2} + (\hat{\alpha}_{N-1} + \hat{\gamma}_{N-1})q_{N-20}^{n+1/2} \\ \hat{\beta}_{N-11}q_{N-11}^{n+1/2} + (\hat{\alpha}_{N-1} + \hat{\gamma}_{N-1})q_{N-21}^{n+1/2} \\ \cdot \\ \cdot \\ \cdot \\ \hat{\beta}_{N-1N-1}q_{N-1N-1}^{n+1/2} + (\hat{\alpha}_{N-1} + \hat{\gamma}_{N-1})q_{N-2N-1}^{n+1/2} \end{bmatrix} \quad (75)$$

Solving the above set of matrices for $q^{n+1/2}$ and q^{n+1} advances to the solution to the modified diffusion equation one contour step Δs along the contour of the polymer chain. Similar to the Pseudo-Spectral technique, the ADI method described here is performed in step 2 of the general algorithm presented at the beginning of this chapter.

4 | Line Tension of Multicomponent Bilayer Membranes

Authors: Ashkan Dehghan, Kyle Pastor and An-Chang Shi

Contribution: I was the principal investigator of this study. I constructed the theoretical framework for modelling multicomponent bilayer membranes, and developed the computational model to solve the SCFT equations. My contribution also includes writing the first draft of the manuscript, which was edited and reviewed by Dr. An-Chang Shi.

[Phys. Rev. E 91, 022713 (2015)]

In this work, we use the self-consistent field theory to study the elastic properties of bilayer membranes. More specifically, we examine the line tension or edge energy of pores in multi-component membranes. A coarse-grained model of an infinite membrane is constructed using amphiphilic AB and ED diblock copolymers, mixed in a solvent modelled as C homopolymers. The large parameter space of the system allows us to investigate the elastic properties of the membrane as a function of various molecular properties. In this work, we examine the line tension σ as a function of molecular architecture and interactions between amphiphilic molecules. The molecular architecture of the amphiphilic molecules is controlled by tuning the hydrophobic/hydrophilic fractions of the chains. The intermolecular interactions are adjusted via the Flory-Huggins parameter χ . Furthermore, the statistical properties of the AB/ED/C membrane is captured using the grand canonical ensemble. The composition of the amphiphilic and solvent molecules in the system is controlled by tuning the chemical potential of the species.

The free energy of the infinite membrane with a circular symmetric pore of radius R is calculated using self-consistent field theory. In the Helfrich model, the free energy of a pore in a tensionless membrane with zero spontaneous curvature is given by $f_H = 2\pi R\sigma$ (58). We fit the free energy of the system, calculated

using self-consistent field theory, with the Helfrich model. This allows us to extract the edge energy or line tension of a membrane pore. Leveraging the cylindrical symmetry of the membrane pore, the self-consistent field theory calculations are performed in a 2-dimensional r-z plane using the Alternating Direction Implicit technique.

The main results of this study can be divided into three main findings. Calculating the line tension as a function of the hydrophobic fraction of the ED chains, we examine the effects of chain architecture on the line tension. We discover that membranes composed of amphiphilic molecules with large head groups, which form cone-shaped structures, have lower line tension as compared to membranes composed of symmetric chains. The opposite effect is observed for membranes composed of inverse cone-shaped molecules. The dependency of the line tension on the molecular architecture of the amphiphilic molecules is due to the packing of the chains at the pore edge. If the spontaneous curvature of the asymmetric molecules matches the curvature of the pore edge, the line tension could be lowered by packing those chains at the edge. We show this effect by examining the line tension as a function of the concentration of the cone- and inverse cone-shaped molecules. By plotting the density distribution of the polymer species, we observe that the cone-shaped molecules concentrate at the pore edge. Lastly, we study the effects of intermolecular interactions on the pore line tension in multi-component membranes. We observe that increase in the repulsive interaction between the head groups results in a decrease in the pore edge energy. We argue that the repulsive interaction between the head groups induces the formation of effective cone-shaped molecules, which lower the line tension.

Line tension of multicomponent bilayer membranes

Ashkan Dehghan, Kyle A. Pastor, and An-Chang Shi*

Department of Physics and Astronomy, McMaster University, Hamilton, Ontario, Canada L8S 4M1

(Received 26 November 2014; published 23 February 2015)

The line tension or edge energy of bilayer membranes self-assembled from binary amphiphilic molecules is studied using self-consistent-field theory (SCFT). Specifically, solutions of the SCFT equations corresponding to an infinite membrane with a circular pore, or an open membrane, are obtained for a coarse-grained model in which the amphiphilic species and hydrophilic solvents are represented by AB and ED diblock copolymers and C homopolymers, respectively. The edge energy of the membrane is extracted from the free energy of the open membranes. Results for membranes composed of mixtures of symmetric and cone- or inverse cone-shaped amphiphilic molecules with neutral and/or repulsive interactions are obtained and analyzed. It is observed that an increase in the concentration of the cone-shaped species leads to a decrease of the line tension. In contrast, adding inverse cone-shaped copolymers results in an increase of the line tension. Furthermore, the density profile of the copolymers reveals that the line tension is regulated by the distribution of the amphiphiles at the bilayer edge.

DOI: [10.1103/PhysRevE.91.022713](https://doi.org/10.1103/PhysRevE.91.022713)

PACS number(s): 87.16.D–, 61.25.hk

I. INTRODUCTION

Bilayer membranes self-assembled from phospholipids are ubiquitous in the cell, separating the cell from the exterior environment as well as encasing its internal organelle structures [1]. Many functions of the membrane depend on its physical and mechanical properties. In recent years, a great number of theoretical and experimental studies have focused on the relationship between the molecular properties (such as composition, geometrical shape, and interactions between lipid species) of the amphiphiles and the elastic properties of the self-assembled membranes [2–5]. In particular, the study of pore formation in bilayer membranes has been a subject of great interest for its fundamental importance in processes such as membrane fusion [6–9], transleaflet lipid diffusion [10], and transport of small molecules across the membranes [1]. Many medical and biotechnological applications also take advantage of artificially formed membrane pores for delivering materials into the cell [11,12].

The property of the self-assembled bilayer membrane is strongly affected by the structure and composition of the amphiphilic molecules, with consequences directly impacting the formation and stability of membrane pores. From a phenomenological point of view, the formation and stability of a membrane pore can be understood by considering the membrane's surface tension γ and the line tension σ of an open membrane edge [13]. It should be pointed out that, in the literature, the term “line tension” has been used to refer to the energy of the phase boundary between two phases of lipids coexisting in the same membrane and to the edge energy of an open lipid membrane. In the current study, the line tension refers to the edge energy of an open membrane, and the terms line tension and edge energy will be used interchangeably. In general, the energy associated with creating an open membrane edge originates from the bending of the lipid monolayers at the edge, thus shielding

the hydrocarbons from the water molecules. Therefore, the formation of an open edge is associated with a highly curved lipid monolayer with a large positive curvature. The toroidal structure of an open membrane edge has been examined in a number of computational studies [14,15]. In general, large surface tension and low edge energy would favor the formation of pores. The competition between the surface tension and the edge energy determines the stability of the membrane. In many cases, self-assembled structures such as biological membranes or liposomes are considered to be tensionless, having zero or nearly zero surface tension. Thus for these systems, the formation and stability of pores is mainly determined by the energy of the open edge or the line tension. For bilayer membranes self-assembled from one type of lipid, the line tension is mainly determined by the property of the lipids. However, for multicomponent membranes, the line tension can be further regulated by the composition and molecular property of the amphiphilic species. From this perspective, it is desirable to study the relationship between the composition and molecular property of the amphiphiles and the line tension of an open membrane edge.

In recent years, a number of studies using continuum theory [16–18], computer simulations [14,19–26], and self-consistent field theory [5,27–29] have focused on examining the line tension of model bilayer membranes. In the studies using continuum theory, the structure of the bilayer at the pore edge is modeled by a highly curved monolayer. This approach provides a simple model for estimating the line tension, however it ignores the molecular structure of the amphiphilic molecules. Furthermore, applying the continuum theory to highly curved surfaces could lead to inaccurate results. Computer simulations such as molecular dynamics (MD) or Monte Carlo (MC) simulations provide a more detailed description of the membrane pores, but these simulations are computationally expensive and are limited by the number of amphiphiles. Self-consistent-field theory (SCFT) has also been used for studying the line tension of bilayer membranes, where lipids are modeled as amphiphilic block copolymers. Although SCFT provides a less detailed picture

*shi@mcmaster.ca

of the bilayer membrane as compared with the MC or MD simulations, it is computationally less expensive and provides a complementary method for examining the elastic properties of bilayer membranes.

Many of the theoretical and computational studies examining the elastic properties of bilayers have been focused on single-component membranes [5,19–21,24,25,27,29–33]. For example, Li *et al.* investigated the elastic properties of bilayers using SCFT and the continuum Helfrich model [5]. Modeling lipids as *AB*-diblock copolymers, the authors studied the effects of molecular architecture on the line tension of single-component bilayers [5]. In a similar simulation study, Hu *et al.* used the line tension of bilayer disks as a driving force to construct flat and closed vesicles [33]. By studying this mechanism, the authors were able to develop an accurate theoretical method for calculating the membrane's Gaussian modulus [33]. Very recently, Pera *et al.* examined the edge energy and the stability of pores of single-component lipid membranes using a lattice self-consistent-field theory. These previous studies indicate that the elastic properties of the lipid bilayers are sensitive to the molecular architecture of the lipids within the membrane. On the other hand, it is expected that for membranes formed by multicomponent lipids, lipid-lipid interactions and the interplay between different lipid architectures can play a significant role in determining the membrane properties. It is therefore desirable to extend the study to multicomponent systems.

For multicomponent membranes, a number of experimental, computational, and theoretical studies have been carried out in recent years to examine the effects of composition, geometrical shape, and interactions of lipids and other membrane-associated molecules on their line tension [23,34–36]. For example, Sakuma *et al.* studied the effects of DHPC or DPPC (cone- or cylindrical-shaped) lipids on the stability of pores in giant unilamellar vesicles (GUVs) [36]. Complementing the experimental results, the authors also used a two-dimensional continuum model to support the idea that pore formation can be stabilized by the aggregation of the cone-shaped lipids at the pore edge [36]. In a similar work investigating the effects of inclusion molecules on the line tension of bilayers, Karatekin *et al.* demonstrated that the addition of cholesterol, approximated as inverse cone-shaped molecules, resulted in an increase in the line tension [34]. In contrast, the addition of cone-shaped molecules was shown to reduce the line tension of the bilayer membrane [34]. Using molecular dynamics simulations, de Joannis *et al.* examined the line tension of bilayers composed of short and long tail phospholipids [23]. These authors showed that an increase in the concentration of short tail lipids results in a decrease in the line tension of ribbon-shaped aggregates [23]. Furthermore, they found that the short tail lipids concentrate at the edge of the aggregates [23]. The studies highlighted above indicate that the composition, geometrical shape, and interactions of lipids and other membrane-associated molecules have significant effects on the line tension of multicomponent bilayer membranes. These previous studies have provided valuable insight into the property of multicomponent membranes. Despite these studies, a systematic study of the physical properties of multicomponent model membranes has been scarce.

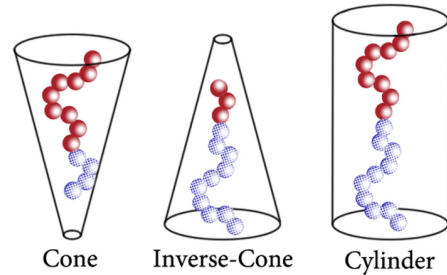


FIG. 1. (Color online) Schematics showing the different molecular architectures studied.

In this paper, we utilize self-consistent-field theory to study the line tension of self-assembled multicomponent bilayers. We model the lipids as amphiphilic *AB* and *ED* diblock copolymers, which self-assemble to form bilayer membranes in a hydrophilic solvent modeled as *C*-homopolymers. Modeling the lipids and water molecules by polymeric species provides a coarse-grained mesoscopic model, in which some of the atomistic details of the system are ignored. The simplified coarse-grained model could lead to significant computational speed-up so that larger systems are accessible. Furthermore, the mesoscopic model and interactions allow the study of collective phenomena of the system, including self-assembled structures and their mechanical properties, as well as phase transitions between these structures [37]. We use the coarse-grained model system to examine the effects of composition, geometrical shape, and interactions of the amphiphilic molecules on the line tension of the bilayer membranes. We control the geometrical shape of the lipid species by varying the relative size of the hydrophilic or hydrophobic blocks of diblock copolymers, as shown schematically in Fig. 1. Similarly, we control the interactions between the lipids by adjusting the Flory-Huggins parameter χ between the blocks. The composition of lipid species within the bilayer is regulated by tuning the relative chemical potential of diblock copolymers, allowing us to examine the effects of lipid composition on the line tension of the membrane edge.

The remainder of this paper is organized as follows. The theoretical model and numerical procedure are presented in Sec. II. Results on the effects of the composition of different lipid species and their geometrical shape and interactions on the line tension of bilayer membranes are reported in Sec. III. Finally, a conclusion and summary of the current study are given in Sec. IV.

II. THEORETICAL FRAMEWORK

The self-consistent-field theory (SCFT) is a well-established theoretical framework for the study of many-body systems, especially polymeric systems. Details of the SCFT formalism have been reported in numerous references [38–40]. In this section, we will give a brief introduction of the theory, focusing on the main aspects of the model and numerical procedure.

The multicomponent system considered in this work is composed of two amphiphilic diblock copolymers (*AB* and *ED*) and a homopolymer (*C*). The hydrophilic or hydrophobic

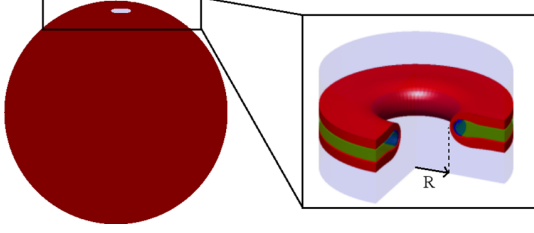


FIG. 2. (Color online) Schematics of the model system investigated. A small pore formed in a giant unilamellar vesicle.

nature of the molecular species is ensured by specifying the interactions between the blocks of the diblock copolymers and the homopolymers, respectively [5]. The thermodynamic properties of the system are most conveniently described using the grand-canonical ensemble, in which the model system contains AB, ED -diblock copolymers and C -homopolymers at a fixed temperature, volume, and activities or chemical potentials. In this study, we assume the membrane geometry is locally flat, corresponding to systems in which the radius of the vesicle is much larger than the region of the pore captured within the computational box. A schematic description of such a configuration is presented in Fig. 2.

In our model, the conformation of the amphiphilic molecules is described by the Gaussian chain model. Furthermore, the interactions between the different segments are modeled using the Flory-Huggins interaction parameters $\chi_{\alpha\beta}$. An application of the SCFT formalism [38–40] to the model system leads to an expression of the grand-canonical partition function of the system,

$$\Xi = \sum_{n_1=0}^{\infty} \sum_{n_2=0}^{\infty} \sum_{n_3=0}^{\infty} \frac{1}{n_1! n_2! n_3!} \int \mathcal{D}[\phi(\mathbf{r})] \mathcal{D}[\omega(\mathbf{r})] \prod_{\mathbf{r}} \delta \left[\sum_{\alpha} \phi_{\alpha}(\mathbf{r}) - 1 \right] \delta \left[\sum_{\beta} \phi_{\beta}(R) - \phi_C(R) \right] e^{-G[\phi, \omega]}, \quad (2.1)$$

where $\phi_{\alpha}(\mathbf{r})$ and $\omega_{\alpha}(\mathbf{r})$ correspond to the volume fraction and conjugate auxiliary fields of the polymer species, with $\alpha = \{A, B, E, C, D\}$ and $\beta = \{A, B, E, D\}$. The local incompressibility constraint is ensured by the first δ function in Eq. (2.1). The second δ function is used as a pinning condition to stabilize a pore of radius R [5]. Furthermore, the quantity $G[\phi, \omega]$ in Eq. (2.1) is the grand potential functional or the grand canonical free-energy functional of the system. It is more convenient, however, to consider the free-energy density $g[\phi, \omega] = N_{AB} G[\phi, \omega] / \rho_0 V$, where the lengths of the polymer chains are scaled with respect to the length of the AB -diblock copolymers. Here, ρ_0 is the monomer density of the polymers, which we assume to be the same for all species. The relative degree of polymerization of the species with respect to the length of the AB -diblock copolymers can be written as $\kappa_{ED} = N_{ED} / N_{AB}$ and $\kappa_C = N_C / N_{AB}$.

Using Lagrangian multipliers η and ξ to enforce the incompressibility and pinning condition, the free-energy density can

be written as

$$g[\phi, \omega, \eta, \xi] = \frac{1}{V} \int d\mathbf{r} \left[\eta(\mathbf{r}) \left(\sum_{\alpha} \phi_{\alpha}(\mathbf{r}) - 1 \right) + \xi(R) \left(\sum_{\beta} \phi_{\beta}(R) - \phi_C(R) \right) - \sum_{\alpha} N_{AB} \omega_{\alpha}(\mathbf{r}) \phi_{\alpha}(\mathbf{r}) + \frac{1}{2} \sum_{\alpha \neq \beta} \phi_{\alpha}(\mathbf{r}) \phi_{\beta}(\mathbf{r}) \chi_{\alpha\beta} N_{AB} \right] - Q_{AB} - \frac{z_{ED}}{\kappa_{ED}} Q_{ED} - \frac{z_C}{\kappa_C} Q_C, \quad (2.2)$$

where Q_{AB}, Q_{ED} , and Q_C are the single-chain partition functions for the AB, ED , and C molecules, and z_{ED} and z_C are the activities of the ED and C species. We note that the chemical potential of the AB -diblock copolymers is chosen such that $z_{AB} = 1$. Using the saddle point approximation, the density profiles $\phi_{\alpha}(\mathbf{r})$ and their conjugate fields $\omega_{\alpha}(\mathbf{r})$ are determined by demanding that the free energy Eq. (2.2) be invariant with respect to variations in the ϕ, ω, η , and ξ fields. This minimization leads to a set of self-consistent field equations,

$$\begin{aligned} \phi_{\alpha}(\mathbf{r}) &= \int_0^{f_{\alpha}} ds q_{\alpha}(\mathbf{r}, s) q_{\alpha}^{\dagger}(\mathbf{r}, f_{\alpha} - s), \\ \phi_{\beta}(\mathbf{r}) &= \frac{z_{ED}}{\kappa_{ED}} \int_0^{\kappa_{ED} f_{\beta}} ds q_{\beta}(\mathbf{r}, s) q_{\beta}^{\dagger}(\mathbf{r}, \kappa_{ED} f_{\beta} - s), \\ \phi_C(\mathbf{r}) &= \frac{z_C}{\kappa_C} \int_0^{\kappa_C} ds q_C(\mathbf{r}, s) q_C^{\dagger}(\mathbf{r}, \kappa_C - s), \\ \omega_{\alpha}(\mathbf{r}) &= \frac{1}{2} \sum_{\theta \neq \alpha} \phi_{\theta}(\mathbf{r}) \chi_{\alpha\theta} + \eta(\mathbf{r}) - \xi(R), \\ \omega_{\beta}(\mathbf{r}) &= \frac{1}{2} \sum_{\theta \neq \alpha} \phi_{\theta}(\mathbf{r}) \chi_{\beta\theta} + \eta(\mathbf{r}) - \xi(R), \\ \omega_C(\mathbf{r}) &= \frac{1}{2} \sum_{\theta \neq C} \phi_{\theta}(\mathbf{r}) \chi_{C\theta} + \eta(\mathbf{r}) + \xi(R), \\ \phi_A(R) + \phi_B(R) + \phi_E(R) + \phi_D(R) &= \phi_C(R), \\ \sum_{\theta} \phi_{\theta}(\mathbf{r}) &= 1, \end{aligned} \quad (2.3)$$

where $\alpha = \{A, B\}$, $\beta = \{E, D\}$, and $\theta = \{A, B, C, D, E\}$. In the above set of self-consistent equations, the functions $q(\mathbf{r}, s)$ and $q^{\dagger}(\mathbf{r}, s)$ are the forward and backward end-integrated propagators. These propagators satisfy the modified diffusion equations,

$$\begin{aligned} \frac{\partial q(\mathbf{r}, s)}{\partial s} &= R_g^2 \nabla^2 q(\mathbf{r}, s) - \omega(\mathbf{r}) q(\mathbf{r}, s), \\ \frac{\partial q^{\dagger}(\mathbf{r}, s)}{\partial s} &= -R_g^2 \nabla^2 q^{\dagger}(\mathbf{r}, s) + \omega(\mathbf{r}) q^{\dagger}(\mathbf{r}, s), \end{aligned} \quad (2.4)$$

with the initial conditions $q(\mathbf{r}, 0) = 1$ and $q^{\dagger}(\mathbf{r}, 1) = 1$ [38]. In the above equations, R_g is the radius of gyration and is defined

as $R_g = b\sqrt{N/6}$, where b is the Kuhn length of the Gaussian chain.

In the geometry examined in our study, the axial symmetry about the center of the pore permits us to write the self-consistent equations in cylindrical coordinates [5]. With this, we apply the alternating direction implicit (ADI) technique to solve the modified diffusion equations [Eqs. (2.4)] in the r - z plane [41]. By solving Eq. (2.4) using appropriate boundary conditions, we can determine solutions of the SCFT equations in terms of the density profiles $\phi_\alpha(\mathbf{r})$ and their conjugate fields $\omega_\alpha(\mathbf{r})$ for a given set of model parameters. In particular, solutions corresponding to a pore of a given radius can be obtained. To extract physical quantities such as membrane surface tension, bending moduli, and pore line tension, we fit the free energy of the system calculated using the SCFT method to that given by the Helfrich model [13]. In the Helfrich model, the membrane can be represented as a two-dimensional elastic sheet, with a free energy given by

$$f_H = \int d\mathbf{A} [2\kappa_M(M - c_0)^2 + \kappa_G G + \gamma] + \int d\mathbf{L} \sigma, \quad (2.5)$$

where M and G are the local mean and Gaussian curvatures. These curvatures can be specified in terms of the principal curvatures c_1 and c_2 as $M = (c_1 + c_2)/2$ and $G = c_1 c_2$ [13,42]. In Eq. (2.5), c_0 , γ , and σ are the spontaneous curvature, membrane's surface tension, and line tension, respectively. For large vesicles or flat membranes, the membrane pore, as shown schematically in Fig. 2, can be considered to be in a flat geometry, thus allowing us to set $c_1 = c_2 = 0$. Using this information, we can rewrite the Helfrich free energy as a function of membrane surface tension and pore line tension,

$$f_H = \gamma \int d\mathbf{A} + \sigma \int d\mathbf{L}.$$

Although the self-assembled biological membranes can often be characterized as tensionless, many studies focus on bilayers with nonzero surface tension [31,34,43]. In the current study, however, we focus on tensionless membranes. Specifically, we vary the chemical potential of the C -homopolymers so that the membrane is tensionless [5]. For a tensionless membrane and with the assumption that the pore is circular and locally flat, we can write the free energy of the pore as $f_H = 2\pi R\sigma$. In this simple form, the free energy of the pore is linearly proportional to the radius. The line tension or the edge energy of the membrane is proportional to the slope of the line. By fitting the free energy calculated using the SCFT method to f_H , we can obtain the line tension for membranes for various copolymer composition, geometrical shape, and interactions. It should be pointed out that extension of the study to membranes with tension is straightforward. Specifically, the free energy of the pore with tension will be given by $f_H = -\pi R^2\gamma + 2\pi R\sigma$. A fitting of the free energy of the pore to this expression can then be used to obtain the surface tension γ and the line tension σ .

III. RESULTS AND DISCUSSION

In this section, we present the results for the line tension of bilayer membranes composed of two types of amphiphilic molecules. We vary the architecture of the lipid species by

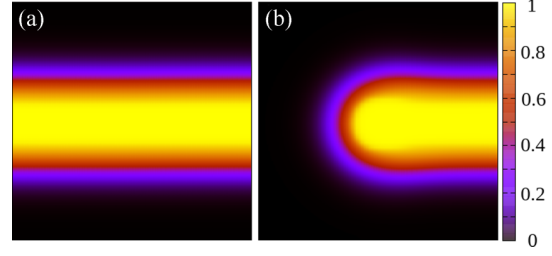


FIG. 3. (Color online) 2D density profiles for the (a) bilayer and (b) pore configuration. The profile illustrates the overall density of the diblock copolymers $AB + ED$ in the lighter regions and solvent C in the dark regions. These plots correspond to the cross-sectional view of the bilayer and the pore, respectively.

adjusting the volume fractions f_α and the relative block lengths κ of the diblock copolymers. Similarly, the interactions between the segments are controlled by adjusting the Flory-Huggins parameters χ . To investigate the effects of amphiphile composition, we introduce an order parameter, $\psi = (\phi_{AB} - \phi_{ED})/(\phi_{AB} + \phi_{ED})$, to characterize the relative volume fraction of the AB and ED amphiphilic molecules within the bilayer. Furthermore, to isolate the effects of molecular geometries, interactions, and membrane composition, we investigate bilayer systems with zero surface tension ($\gamma = 0$). Starting with a system in the bilayer configuration, as shown in Fig. 3(a), we adjust the chemical potential of the solvent such that the membrane is tensionless. We then construct a pore of radius R , illustrated in Fig. 3, using the pinning condition as described in the preceding section.

The free energy of the pore, as described by the continuum model, is $f_H = (2\pi\sigma)R$. In this form, the line tension σ can be determined by evaluating the free energy of the system as a function of radius R . Figure 4 presents the free energy obtained from the SCFT calculations, as a function of pore radius

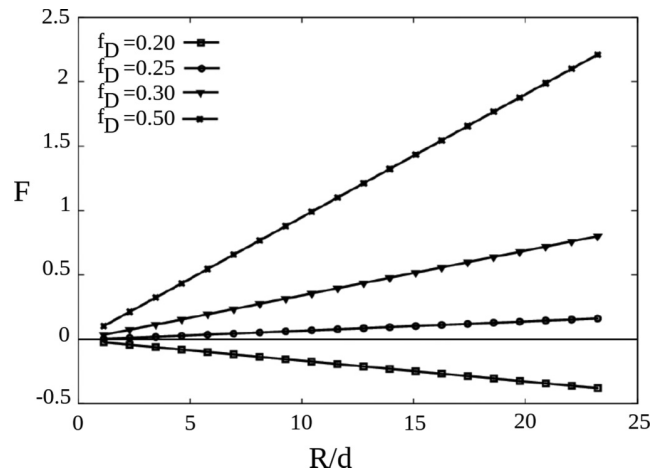


FIG. 4. The free energy as a function of pore radius R for blends with $\chi_{AB} = \chi_{ED} = \chi_{AD} = \chi_{BE} = \chi_{BC} = \chi_{CD} = 30$, $f_A = f_B$, $\kappa_C = 1$, and various ED -molecular architectures. The molecular fraction of the D species is defined as $f_D = N_D/N_{AB}$. The pore radius R is measured in units of R_g and is normalized with respect to the bilayer thickness d , given as $d \sim 4.3R_g$.

for a model system with $\chi_{AB} = \chi_{ED} = \chi_{AD} = \chi_{BE} = \chi_{BC} = \chi_{CD} = 30$, $\chi_{AE} = \chi_{BD} = \chi_{AC} = \chi_{CE} = 0$, $f_A = f_B$, $\kappa_C = 1$, $\mu_{AB} = \mu_{ED}$, and different ED -molecular architectures. By adjusting f_D while keeping the length of the E -block constant, we change the geometry of the ED -molecules from a cylindrical- to a cone-shaped structure. The results can then be used to examine the effects of mixing cylindrical- and cone-shaped lipids on the line tension.

Figure 4 shows the free energy of 1:1 mixtures of cylindrical- and cone-shaped molecules as a function of pore radius R . The first feature to notice is that the line tension, which is proportional to the slope of the free-energy curve, decreases with an increase in the asymmetry (f_D) of the ED -molecules. For a tensionless membrane, the only contribution to the free energy is from the line tension. In this case, the stability of the pore is determined by analyzing the free energy as function of the pore radius. For blends with $f_D = 0.5$, 0.3, and 0.25, the slope of the free energy is positive, corresponding to pores that would shrink upon the release of the pinning constraint. In contrast, blends with $f_D = 0.2$ have a negative line tension, which correspond to pores that would grow in size, resulting in the rupture of the membrane. Most interestingly, binary lipid mixtures with zero line tension would correlate with long-lasting stable pores. These results suggest that an increase in the lifetime of a pore can be obtained by tuning the concentration of cone-shaped detergent molecules within the membrane.

To further explore the effects of lipid asymmetry on the pore line tension, we investigate membranes composed of various concentrations of ED -molecules. By controlling the chemical potential of the ED -diblock copolymers (μ_{ED}), we can adjust the relative composition of the ED -molecules in the membrane. Figure 5 presents the line tension σ as a function of the order parameter ψ for model systems with $\chi_{AB} = \chi_{ED} = \chi_{AD} = \chi_{BE} = \chi_{BC} = \chi_{CD} = 30$, $\chi_{AE} = \chi_{BD} = \chi_{AC} = \chi_{CE} = 0$, $f_A = f_B$, $\kappa_C = 1$, and $f_D = 0.25$, 0.30, and 0.40. The molecular composition within the membrane is characterized by the order parameter ψ , where $\psi = 1$

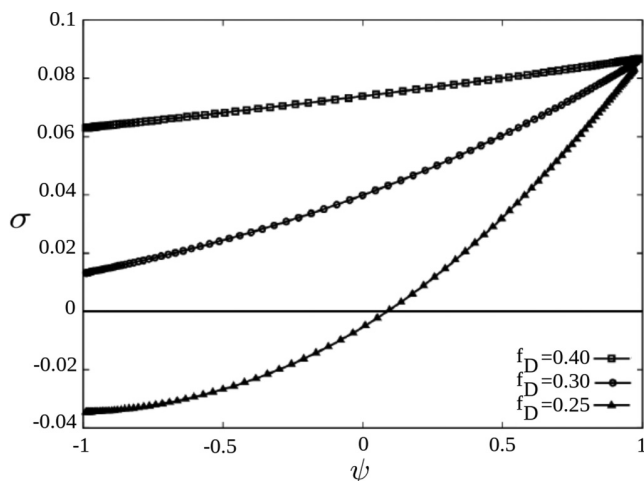


FIG. 5. The line tension σ as a function of order parameter ψ for blends with $\chi_{AB} = \chi_{ED} = \chi_{AD} = \chi_{BE} = \chi_{BC} = \chi_{CD} = 30$, $\chi_{AE} = \chi_{BD} = \chi_{AC} = \chi_{CE} = 0$, $f_A = f_B$, $\kappa_C = 1$, and $f_D = 0.25$, 0.3, and 0.4.

and -1 correspond to membranes composed purely of AB and ED species, respectively. As shown in Fig. 5, membranes composed of asymmetric molecules (cone-shaped) have lower line tension than those composed of symmetric molecules (cylindrical-shaped). A decrease in σ for membranes composed of asymmetric lipids has been reported previously for single-component membranes by Li *et al.* [5]. These authors investigated the effect of molecular fraction f on the line tension for single-component bilayers, and they showed that a decrease in the relative size of the head groups results in a decrease in the line tension [5].

As illustrated in Fig. 5, an increase in the concentration of cone-shaped lipid species in the membrane leads to a decrease in the line tension σ . Furthermore, the decrease of σ is more pronounced for cone-shaped lipids with smaller head groups (characterized by smaller f_D), in that the line tension can be changed from positive to negative. For example, for a binary mixture of symmetric AB - and asymmetric ED -molecules with $f_D = 0.25$, the pure AB and ED membranes have positive and negative line tensions, respectively. As shown in Fig. 5, for this system the line tension vanishes at a critical composition, ψ_c . At this concentration, a pore with a finite radius formed in a tensionless membrane would be stable.

A decrease in the line tension as a function of an increase in the concentration of cone-shaped molecules has been reported in a number of experiments [34–36]. It has been suggested that the decrease in the line tension is caused by the aggregation of the cone-shaped molecules at the pore edge [34–36]. The availability of the SCFT solutions allows us to investigate the segregation of lipid species within the membrane by analyzing the density profile of the lipid species. Figure 6 presents the density profiles for a system with $\chi_{AB} = \chi_{ED} = \chi_{AD} = \chi_{BE} = \chi_{BC} = \chi_{CD} = 30$, $\chi_{AE} = \chi_{BD} = \chi_{AC} = \chi_{CE} = 0$, $f_A = f_B$, $\kappa_C = 1$, $f_D = 0.25$, and $\psi = 0.18$. As shown in Fig. 6, the cone-shaped ED -molecules have a higher concentration at the pore edge. This effect can be seen more clearly in the one-dimensional profile (Fig. 6)

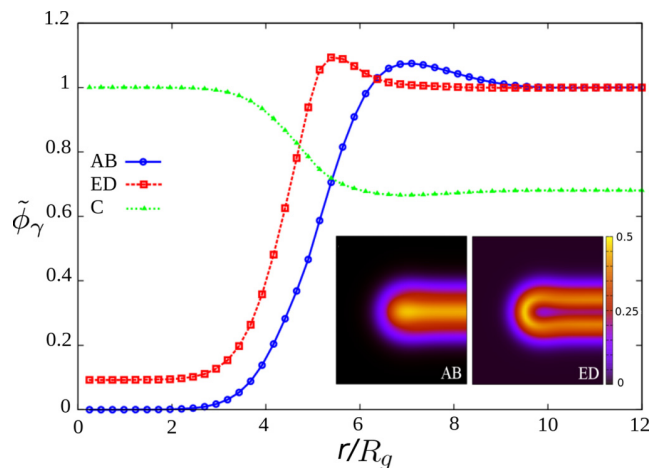


FIG. 6. (Color online) Relative concentrations of the AB , ED , and C molecules $\tilde{\phi}_\gamma$ ($\gamma = AB, ED$, and C) as a function of position for blends with $f_D = 0.25$. Inset: 2D density profiles of the (a) AB and (b) ED blends for $\chi_{AB} = \chi_{ED} = \chi_{AD} = \chi_{BE} = \chi_{BC} = \chi_{CD} = 30$, $\chi_{AE} = \chi_{BD} = \chi_{AC} = \chi_{CE} = 0$, $f_A = f_B$, $\kappa_C = 1$, $f_D = 0.25$, and $\psi = 0.18$.

of the relative concentrations of the molecular species $\tilde{\phi}_\gamma = \phi_\gamma / \phi_{\gamma, \text{bulk}}$ ($\gamma = AB, ED$, and C), which is the concentration of the molecular species normalized by their bulk values for a planar membrane. The results shown here clearly reveal an increase in the concentration of ED -molecules at the pore edge. This observation of molecular segregation to the pore edge provides strong evidence that the mechanism of line tension decrease is the coupling of molecular density with the curvature of the amphiphilic monolayers.

To understand why the segregation of the cone-shaped molecules at the pore edge reduces the line tension, we need to consider the spontaneous curvature of the AB and ED monolayers. When a pore is formed, the hydrophobic tails are exposed to the solvent. To reduce the unfavorable interaction between the hydrophobic tails and solvent, the molecules rearrange to shield the hydrophobic segments. This results in the formation of an edge with a large positive curvature. If the bilayer is composed only of symmetric molecules, with zero spontaneous curvature, the penalty for bending the membrane is large. On the other hand, if cone-shaped molecules with positive spontaneous curvature are added to the membrane, they could aggregate at the pore edge and act as pore stabilizers, thus reducing the line tension.

The above analysis can be extended to the case of species with inverse cone-shaped geometries. In addition to inverse cone-shaped lipids, the shape of cholesterol molecules is often described as an inverse cone-shaped structure. Given the abundance of cholesterol in biological membranes, it is interesting to explore the effects of inverse cone-shaped molecules on the line tension. As a model system for inverse cone-shaped lipids, we calculated the line tension for membranes composed of AB and ED molecules, where $N_A = N_B$ and $N_D > N_E$. Figure 7 gives the line tension of this bilayer system as a function of the order parameter ψ , for blends with $\chi_{AB} = \chi_{ED} = \chi_{AD} = \chi_{BE} = \chi_{BC} = \chi_{CD} = 30$, $\chi_{AE} = \chi_{BD} = \chi_{AC} = \chi_{CE} = 0$, $f_A = f_B$, $\kappa_C = 1$, $f_E = 0.25, 0.35$, and 0.45 . As before, $\psi = 1$ and -1 correspond

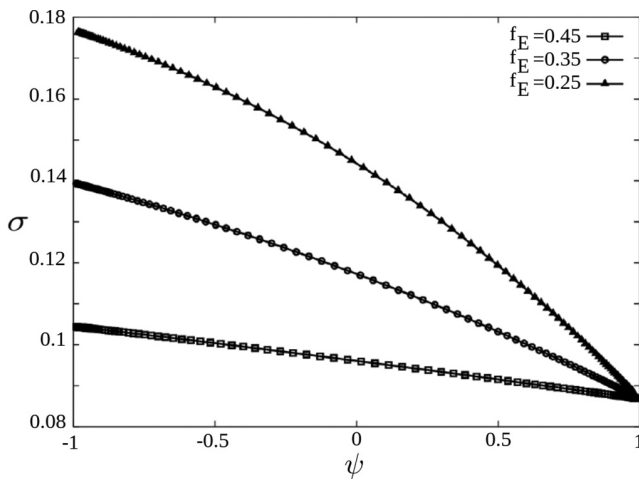


FIG. 7. Line tension σ as a function of order parameter ψ for blends with $\chi_{AB} = \chi_{ED} = \chi_{AD} = \chi_{BE} = \chi_{BC} = \chi_{CD} = 30$, $f_A = f_B$, $\kappa_C = 1$, and $f_E = 0.25, 0.35$, and 0.45 .

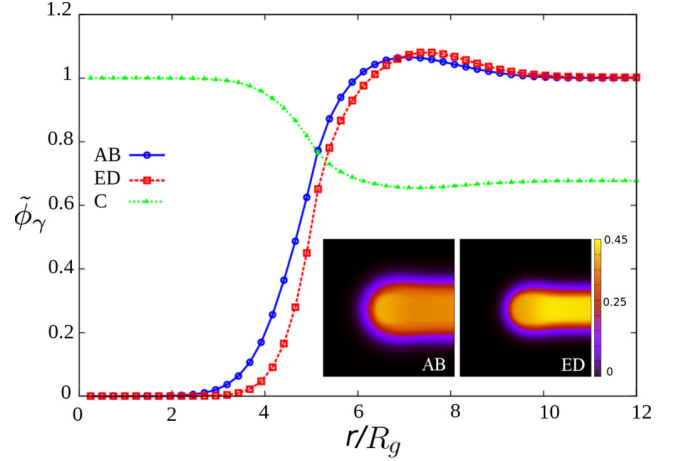


FIG. 8. (Color online) Relative concentrations of the AB , ED , and C molecules $\tilde{\phi}_\gamma$ ($\gamma = AB, ED$, and C) as a function of position. Inset: 2D density profiles of the (a) AB and (b) ED blends for $\chi_{AB} = \chi_{ED} = \chi_{AD} = \chi_{BE} = \chi_{BC} = \chi_{CD} = 30$, $f_A = f_B$, $\kappa_C = 1$, $f_E = 0.25$, and $\psi = 0.3$.

to membranes composed of pure AB and ED molecules, respectively.

The results shown in Fig. 7 reveal that an increase in the concentration of the inverse cone-shaped molecules (ED -molecules) leads to an increase in the line tension of the membrane edge. The increase of the line tension is more pronounced for ED -molecules with a larger block asymmetry. To understand why inverse cone-shaped molecules result in an increase in the line tension, we will focus on the distribution of the AB and ED species within the bilayer. In Fig. 8, we present the density profiles for the AB , ED and C molecules. In contrast with the case of cone-shaped ED -molecules, there is a depletion of the ED -molecules at the pore edge. This effect is shown more clearly in the one-dimensional density profile, where the relative concentrations of the molecules $\tilde{\phi}_\gamma$ ($\gamma = AB, ED$, and C) are plotted as a function of the position. The aggregation of the ED -molecules away from the pore edge is caused by the mismatch between the spontaneous curvature of the ED -molecules and that of the pore edge. This indicates that pore formation in systems with a high concentration of inverse cone-shaped molecules is highly unfavorable.

Experiments on the effects of cholesterol molecules on the stability of membranes indicate that an increase in the concentration of cholesterol molecules results in a more stable membrane [43–45]. For example, Koronkiewicz and Kalinowski showed that the critical radius, at which the membrane ruptures, increases for membranes with higher cholesterol concentration [45]. For a bilayer membrane with a finite surface tension, the free energy as given by the continuum model can be written as $f_H = 2\sigma\pi r - \gamma\pi r^2$, resulting in a critical radius of $r_c = 2\sigma/\gamma$. Therefore, the critical radius is proportional to the line tension σ . As shown in Fig. 7, the line tension increases with an increase in the concentration of the inverse cone-shaped molecules. For a system with finite surface tension, this corresponds to an increase in the critical pore radius r_c . These results indicate that an increase in the concentration of inverse cone-shaped molecule such as

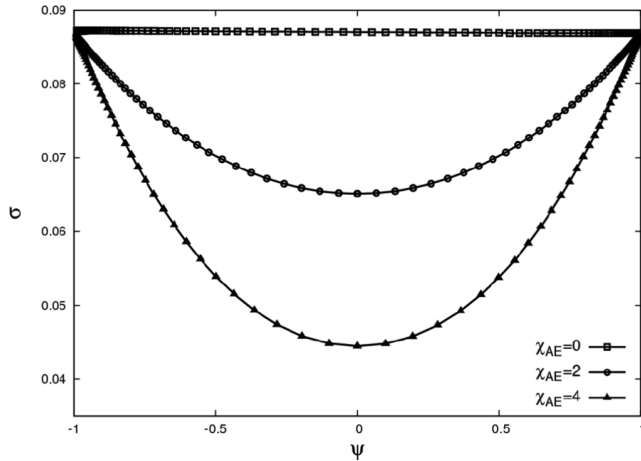


FIG. 9. The line tension σ as a function of the order parameter ψ for blends with $\chi_{AB} = \chi_{ED} = \chi_{AD} = \chi_{BE} = \chi_{BC} = \chi_{CD} = 30$, $f_A = f_B = f_E = f_D$, and $\kappa_C = \kappa_{ED} = 1$ for $\chi_{AE} = 0, 2$, and 4.

cholesterol would correspond to an increase in the energy associated with creating a pore, therefore preventing pore formation and stabilizing the membrane.

Finally, we investigate the effects of head-group interactions on the line tension of multicomponent bilayers. We begin by considering a repulsive interaction between the A/E blocks (head groups) for symmetric blends with $N_{AB} = N_{ED} = N_C$. Figure 9 gives the line tension σ as a function of the order parameter ψ , for blends with $\chi_{AB} = \chi_{ED} = \chi_{AD} = \chi_{BE} = \chi_{BC} = \chi_{CD} = 30$, $\chi_{BD} = \chi_{AC} = \chi_{CE} = 0$, $f_A = f_B = f_E = f_D$, $\kappa_C = \kappa_{ED} = 1$, and $\chi_{AE} = 0, 2$, and 4. In this figure, the line tension for blends with $\chi_{AE} = 0$ is taken as a reference. It is interesting to point out that mixing symmetric molecules with repulsive head group interactions leads to a decrease in the line tension, with a minimum at $\psi = 0$. We can understand the decrease in the line tension for a mixed system by considering the properties of a pore modeled as a folded monolayer. Using a two-dimensional continuum model, Li *et al.* considered the line tension of a pore created by folding a monolayer onto itself, forming a pore edge similar to that seen in Fig. 3(b) [5]. Using this approach, the authors derived an expression for the line tension as a function of the monolayer properties,

$$\sigma = \pi \kappa_M \frac{1 - 4c_0\delta}{2\delta}, \quad (3.1)$$

where κ_M , c_0 , and δ are the bending modulus, spontaneous curvature, and thickness of the monolayer, respectively [5,46]. For a symmetric system such as a single-component AB bilayer, the spontaneous curvature of the monolayer c_0 is zero. In a mixed AB/ED system, the effect of the repulsive head group interaction would result in the formation of an effective cone-shaped molecule, shown schematically in Fig. 10. The nonzero spontaneous curvature for the cone-shaped molecule results in a decrease in the line tension as shown in Fig. 9. These results indicate that the line tension of a membrane can be regulated by introducing molecules with repulsive head group interactions.

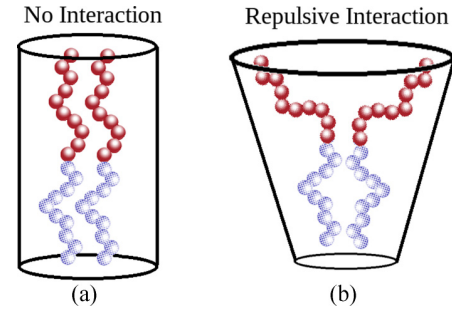


FIG. 10. (Color online) Schematic diagram showing the effect of repulsive head group interaction on the overall geometrical shape of the lipids.

IV. CONCLUSION

Using the self-consistent field theory, we have investigated the line tension or edge energy of self-assembled multicomponent bilayer membranes, focusing on the effects of composition, geometrical shape, and interactions of lipid species. The lipid species in the bilayer were modeled as amphiphilic AB and ED diblock copolymers in a solvent, modeled as C -homopolymers. Solutions of the SCFT equations are obtained for a bilayer membrane with a pore of fixed size. By fitting the SCFT free energy of the pore to the Helfrich model, we have extracted the line tension of the membrane. We then examined the effects of the composition, geometrical shape, and interactions of lipid species on the line tension.

We first investigated bilayer systems composed of cylindrical, cone-, and inverse cone-shaped lipid species, focusing on the effects of relative lipid composition on the line tension of the self-assembled bilayer membranes. Our results revealed that an increase in the concentration of the cone-shaped lipids results in a decrease in the line tension. The mechanism underlying the reduction in the line tension was found to be related to the segregation of the molecules within the membrane. Lipid segregation is driven to relieve the stress caused by the large positive curvature of the pore edge. The local curvature of the pore matches more closely to the spontaneous curvature of the cone-shaped lipids, resulting in the aggregation of the cone-shaped species at the pore edge. The overall effect of adding cone-shaped lipids to the bilayer is consistent with experimental and computational studies [34–36]. In contrast to the behavior of cone-shaped lipids, we discovered that an increase in the concentration of the inverse cone-shaped molecules results in an increase in the pore line tension. The underlying mechanism for this increase, similar to the cone-shaped lipid system, is the segregation of lipids within the bilayer. In contrast, however, the spontaneous curvature of the inverse cone-shaped lipids is different from that of the pore edge. This results in a depletion of the inverse cone-shaped molecules from the pore edge. Experiments have also shown that an increase in the concentration of inverse cone-shaped molecules such as cholesterol could result in an increase in the line tension of the membrane, causing it to be more stable [34]. Finally, we considered the effects of repulsive interaction between the head groups of symmetric lipid species. We discovered that an increase in the repulsive interaction between the head groups results in a decrease in the

pore line tension. This effect was understood to be caused by the formation of effective cone-shaped lipid aggregates, which we know to lower the line tension.

Although the coarse-grained model ignores many molecular details of lipids, the results and conclusion from the current study provide a qualitative understanding of the interplay between the lipid segregation and local curvature. In particular, the results provide clear evidence that the segregation of the lipids can lead to the increase or decrease of the line tension, depending on the geometry of the molecules. The predicted trend of the line tension as a function of the concentration of the second lipids is in good agreement with available

experiments. Although this trend of line tension could be understood intuitively, the current study places the mechanism of the line tension behavior in a multicomponent lipid system on a solid theoretical base.

ACKNOWLEDGMENTS

This work was supported by the Natural Sciences and Engineering Research Council (NSERC) of Canada. The computation was made possible by the facilities of the Shared Hierarchical Academic Research Computing Network (SHARCNET).

-
- [1] B. Alberts *et al.*, *Molecular Biology of the Cell: 6th Edition* (Garland Science, New York, 2014).
- [2] P. Bashkurov, K. Chekashkina, S. Akimov, P. Kuzmin, and V. Frolov, *Biochem. (Moscow) Suppl. Ser. A* **5**, 205 (2011).
- [3] A.-F. Bitbol, D. Constantin, and J.-B. Fournier, *PLoS ONE* **7**, e48306 (2012).
- [4] J. F. Nagle, *Faraday Disc.* **161**, 11 (2013).
- [5] J. Li, K. A. Pastor, A.-C. Shi, F. Schmid, and J. Zhou, *Phys. Rev. E* **88**, 012718 (2013).
- [6] D. P. Siegel, *Biophys. J.* **65**, 2124 (1993).
- [7] H. Noguchi and M. Takasu, *J. Chem. Phys.* **115**, 9547 (2001).
- [8] M. Müller, K. Katsov, and M. Schick, *J. Chem. Phys.* **116**, 2342 (2002).
- [9] M. Schick, K. Katsov, and M. Müller, *Mol. Phys.* **103**, 3055 (2005).
- [10] R. M. Raphael, R. E. Waugh, S. Svetina, and B. Žekš, *Phys. Rev. E* **64**, 051913 (2001).
- [11] E. Neumann, M. Schaefer-Ridder, Y. Wang, and P. Hofschneider, *EMBO J.* **1**, 841 (1982).
- [12] T. Y. Tsong, *J. Electroanal. Chem. Interf. Electrochem.* **299**, 271 (1990).
- [13] W. Helfrich, *Z. Naturforsch. Teil C* **28**, 693 (1973).
- [14] F. Y. Jiang, Y. Bouret, and J. T. Kindt, *Biophys. J.* **87**, 182 (2004).
- [15] H. Leontiadou, A. E. Mark, and S. J. Marrink, *Biophys. J.* **86**, 2156 (2004).
- [16] J. D. Moroz and P. Nelson, *Biophys. J.* **72**, 2211 (1997).
- [17] S. May, *Eur. Phys. J. E* **3**, 37 (2000).
- [18] R. Molotkovsky and S. Akimov, *Biochem. (Moscow) Suppl. Ser. A* **3**, 223 (2009).
- [19] M. Müller and M. Schick, *J. Chem. Phys.* **105**, 8282 (1996).
- [20] T. V. Tolpekina, W. K. den Otter, and W. J. Briels, *J. Chem. Phys.* **121**, 12060 (2004).
- [21] C. Loison, M. Mareschal, and F. Schmid, *J. Chem. Phys.* **121**, 1890 (2004).
- [22] Z.-J. Wang and D. Frenkel, *J. Chem. Phys.* **123**, 154701 (2005).
- [23] J. de Joannis, F. Y. Jiang, and J. T. Kindt, *Langmuir* **22**, 998 (2006).
- [24] J. Wohler, W. K. den Otter, O. Edholm, and W. J. Briels, *J. Chem. Phys.* **124**, 154905 (2006).
- [25] W. K. den Otter, *J. Chem. Phys.* **131**, 205101 (2009).
- [26] W. Shinoda, T. Nakamura, and S. O. Nielsen, *Soft Matter* **7**, 9012 (2011).
- [27] R. R. Netz and M. Schick, *Phys. Rev. E* **53**, 3875 (1996).
- [28] K. Katsov, M. Müller, and M. Schick, *Biophys. J.* **87**, 3277 (2004).
- [29] H. Pera, J. M. Kleijn, and F. A. M. Leermakers, *J. Chem. Phys.* **142**, 034101 (2015).
- [30] M. Müller and M. Schick, *Phys. Rev. E* **57**, 6973 (1998).
- [31] V. Talanquer and D. W. Oxtoby, *J. Chem. Phys.* **118**, 872 (2003).
- [32] C. L. Ting, D. Appelö, and Z.-G. Wang, *Phys. Rev. Lett.* **106**, 168101 (2011).
- [33] M. Hu, J. J. Briguglio, and M. Deserno, *Biophys. J.* **102**, 1403 (2012).
- [34] E. Karatekin, O. Sandre, H. Guitouni, N. Borghi, P.-H. Puech, and F. Brochard-Wyart, *Biophys. J.* **84**, 1734 (2003).
- [35] P.-H. Puech, N. Borghi, E. Karatekin, and F. Brochard-Wyart, *Phys. Rev. Lett.* **90**, 128304 (2003).
- [36] Y. Sakuma, T. Taniguchi, and M. Imai, *Biophys. J.* **99**, 472 (2010).
- [37] M. Müller, K. Katsov, and M. Schick, *Phys. Rep.* **434**, 113 (2006).
- [38] A.-C. Shi, in *Developments in Block Copolymer Science and Technology*, edited by I. Hamley (Wiley, New York, 2004).
- [39] M. W. Matsen, in *Soft Matter, Volume 1: Polymer Melts and Mixtures*, edited by G. Gompper and M. Schick (Wiley-VCH, Weinheim, 2006).
- [40] G. Fredrickson, *The Equilibrium Theory of Inhomogeneous Polymers* (Oxford University Press, Oxford, UK, 2006).
- [41] J. Strikwerda, *Finite Difference Schemes and Partial Differential Equations* (Society for Industrial and Applied Mathematics, Philadelphia, 2007).
- [42] D. Nelson, T. Piran, and S. Weinberg, *Statistical Mechanics of Membranes and Surfaces*, 2nd ed. (World Scientific, Singapore, 2004).
- [43] D. V. Zhelev and D. Needham, *Biochim. Biophys. Acta—Biomembranes* **1147**, 89 (1993).
- [44] C. Karolis, H. G. Coster, T. C. Chilcott, and K. D. Barrow, *Biochim. Biophys. Acta—Biomembranes* **1368**, 247 (1998).
- [45] S. Koronkiewicz and S. Kalinowski, *Biochim. Biophys. Acta—Biomembranes* **1661**, 196 (2004).
- [46] M. Bergstrom, *J. Chem. Phys.* **118**, 1440 (2003).

5 | Effect of Mobile Ions on the Electric Field Needed to Orient Charged Diblock Copolymer Thin Films

Authors: **Ashkan Dehghan**, Michael Schick and An-Chang Shi

Contribution: I was the principal investigator of this study. In collaboration with Dr. Michael Schick and Dr. An-Chang Shi, I constructed the self-consistent field theory framework for studying the effects of ion concentration on the orientation of domains formed in charged block copolymer thin films. In addition, I developed the computational model for solving the SCFT equations. My contribution also includes writing the first draft of the manuscript, which was edited and reviewed by Dr. Michael Schick and Dr. An-Chang Shi.

[J. Chem. Phys. 143, 134902 (2015)]

This study is the first of two papers which aim to examine techniques for directing the self-assembly of microphases formed in block copolymer thin films. In the first paper, we examine the effects of ion concentration on the strength of the electric field required to reorient lamellae domains in block copolymer thin films. The motivation for this study is to explore the utility of an external electric field as a mechanism for directing the self-assembly of lamellae forming charged AB diblock copolymers. More specifically, we calculate the critical electric field required to reorient lamellae domains from the parallel orientation, favoured by the surface interactions, to the perpendicular orientation. Although the use of an external electric field for directing the self-assembly of block copolymers has proven to be a useful mechanism (59, 60), it remains a challenge to adopt this technique in thin films with heights lower than a critical value. For some systems,

the strength of the electric field required to reorient the domains often results in the dielectric breakdown of the polymeric material (59). For this reason, it is important to explore mechanisms which could lower the strength of the required electric field for realigning the domains. In this paper, we show that the effects of ion concentration on the strength of the critical electric field depend on whether the charged or neutral polymer species interacts favourably with the surfaces.

To study the effects of ion concentration, we construct a self-consistent field theory model of charged diblock copolymers, with negatively charged A and neutral B blocks. The A and B blocks are characterized by two different dielectric constants, κ_A and κ_B . In addition to the negative charge on the backbone of the A polymers, we also introduce free positive counter ions to ensure global charge neutrality. The localization of the positive ions in the system is controlled using the strength of the Flory-Huggins parameter χ_{BI} . Polymer-surface interactions are adjusted by tuning a parameter μ , which controls the strength of the relative interaction between the A and B species and thin film surfaces. Lastly, the strength of the electric field is controlled by tuning the potential difference across the top and bottom electrodes. With this, we examine two scenarios. One, in which the neutral polymer species interacts favourably with the top and bottom surfaces and second, where the charged polymer species do.

We discover that the effects of added mobile ions on the electric field required to reorient the lamellar domains from the parallel to the perpendicular orientation depends on whether the neutral or charged polymer species is favoured by the surfaces. In the case where neutral polymer species is favoured, the added mobile ions reduce the critical electric field. This effect is more significant in melts where the mobility of the ions is restricted to the charged domains, i.e. large χ_{BI} values. We show that the reduction in the critical electric field is due to the difference in the magnitude of charge separation between the parallel and perpendicular morphologies. The magnitude of charge separation is greater in melts where ions are confined to the charged domains.

On the other hand, if the charged polymer species is favoured by the surfaces, the addition of ions increases the critical electric field. As before, an increase in χ_{BI} is shown to enhance this effect, resulting in an even greater critical electric field. In this scenario, there is no significant difference in the magnitude of charge separation between the parallel and perpendicular morphologies. However, in the parallel orientation, both negative and positive charges can coat the top and bottom electrodes. On the other hand, this is only

partially possible in the perpendicular morphology. Therefore, the parallel orientation is favoured over the perpendicular phase.

Effect of mobile ions on the electric field needed to orient charged diblock copolymer thin films

Ashkan Dehghan,¹ M. Schick,² and An-Chang Shi¹

¹*Department of Physics and Astronomy, McMaster University, Hamilton, Ontario L8S 4M1, Canada*

²*Department of Physics, University of Washington, Seattle, Washington 98195, USA*

(Received 11 June 2015; accepted 15 September 2015; published online 5 October 2015)

We examine the behavior of lamellar phases of charged/neutral diblock copolymer thin films containing mobile ions in the presence of an external electric field. We employ self-consistent field theory and focus on the aligning effect of the electric field on the lamellae. Of particular interest are the effects of the mobile ions on the critical field, the value required to reorient the lamellae from the parallel configuration favored by the surface interaction to the perpendicular orientation favored by the field. We find that the critical field depends strongly on whether the neutral or charged species is favored by the substrates. In the case in which the neutral species is favored, the addition of charges decreases the critical electric field significantly. The effect is greater when the mobile ions are confined to the charged lamellae. In contrast, when the charged species is favored by the substrate, the addition of mobile ions stabilizes the parallel configuration and thus results in an increase in the critical electric field. The presence of ions in the system introduces a new mixed phase in addition to those reported previously. © 2015 AIP Publishing LLC. [<http://dx.doi.org/10.1063/1.4931826>]

I. INTRODUCTION

Block copolymers are commonly utilized because of their ability to form self-assembled structures with wavelengths that scale as the size of the polymers. This is generally on the order of 10-100 nm. Such a property offers the possibility of many applications such as nanolithographic templates, nanostructured networks, stimuli-responsive materials, and well-ordered arrays of metal nanowires.^{1,2} The challenge encountered when using thin films of block copolymers is that the creation of highly ordered, long-range, single-domain structures is often made difficult by interactions at the surface of the polymer film. These interactions often result in the formation of microdomains self-assembled parallel to the air or substrate interfaces. In many applications, however, the perpendicular orientation is the desired one. This problem has motivated the implementation of techniques for directing the self-assembly of block copolymers or for realigning the morphologies from the parallel to the perpendicular orientation.

A number of methods have been developed for directing the self-assembly of block copolymers and have been reviewed recently.³ Among them are the use of pre-patterned substrates,⁴⁻⁷ topographically modified substrates,⁸⁻¹⁰ and external stimuli such as an electric field.¹¹⁻¹⁶ The electric field brings about alignment due to a difference in the dielectric constant of the different blocks of the polymers. The effects of the strength of this field, of the polymer-substrate interactions, and of the film thickness have been the subject of several experiments.¹⁷⁻²⁰ For example, Xu *et al.* investigated the effects of an external electric field on the cylinder forming diblock copolymers in thin films.²¹ They showed that redirecting the formation of cylinders from the parallel

configuration, caused by the selective polymer/substrate interaction, to the perpendicular orientation was made possible by application of the field.²¹ In a theoretical study, Tsori and Andelman examined the alignment of microdomains formed by symmetric polystyrene-*b*-poly(methyl methacrylate) (PS-*b*-PMMA) in the presence of an external electric field as a function of film thickness and polymer/surface interactions.¹³ They noted that the ability of the electric field to induce the self-assembly of microdomains in the direction parallel to it depends strongly on the film thickness. For some systems, the electric field required to reorient the morphologies might well result in the dielectric breakdown of the material.

To induce the formation of perpendicularly oriented microdomains in thin films by means of smaller electric fields, Tsori *et al.* suggested adding mobile ions.^{22,23} The reasoning is that the electrostatic potential energy of a dipole moment per unit volume, \mathbf{P} , in an electric field, \mathbf{E} , is $-\mathbf{P} \cdot \mathbf{E}$. The battery keeps the total electric field across the film constant. Because the dipole moment depends upon the separation of charges, the addition of mobile charges is expected to increase this separation and thereby increase the difference in the energy of the parallel and perpendicular orientations. The unstated assumption is that the increase in dipole moment is larger in the perpendicular orientation than in the parallel one. They also suggested that Li ions, present in the system from the anionic polymerization process, might be responsible for the success in bringing about reorientation of the microdomains. Any significant role that ions play can easily be discerned by applying an orienting, frequency-dependent, electric field. At low frequencies, the effect of free ions would be manifest and would vanish at higher frequencies. It was noted²⁴ that there was no frequency dependence in some successfully oriented films of PS-PMMA.²⁵ Nonetheless, when lithium chloride was

intentionally added to the system, the effect due to the free ions was quite clear.²⁵ Equally clear was the effect of doping a PS-PMMA system with lithium triflate, a salt which dissolves almost completely in the PMMA and much less so in the PS.²⁶

The reasons for the success of free ions in reducing the value of the electric field needed to reorient the self-assembled domains and the generality of the result is less clear. Wang *et al.* attribute the success to a complexation of Li ions with carbonyl groups in the PMMA which enhances the difference between the dielectric constants of the PMMA and PS blocks.²⁵ In contrast, Kohn *et al.* take an approach²⁶ more in the spirit of the original suggestion of Tsoi *et al.* in that they treat their system as a simplified one, consisting of alternating dielectric and conducting slabs. They calculate the torque on the interfaces due to the mobile ions. In a similar spirit, Putzel *et al.* considered a toy model consisting of alternating layers of two materials, A and B, characterized by different dielectric constants.¹⁴ The A layers were uniformly charged, with mobile counter ions providing charge neutrality. The substrate preferred the B layers. They investigated the effect of selectively localizing the counter ions within one of the two blocks. They found that if the counter ions were confined such that *each* layer of A material was electrically neutral, then the value of the electric field needed to bring about a perpendicular orientation was indeed decreased by the addition of ions. This was attributed to the fact that only in the perpendicular configuration could an extensive polarization be brought about, i.e., an induced dipole moment per unit volume with a charge separation on the order of the film thickness. However, if the counter ions were free to migrate so that the system as a whole was electrically neutral but that individual layers of A were not, then the addition of charges did not necessarily decrease the field needed to reorient the system. Indeed they found that if the substrate preferred the A layers, then addition of ions could well *increase* the field needed for reorientation.

In this paper, we consider a system of lamellar forming AB diblock copolymers. The A polymers are partially charged and the system contains mobile counter ions which provide charge neutrality (Figure 1). Similar systems have been considered previously,²⁷⁻³¹ although their objective was to determine the effect of the charges on the phase diagram of the polymeric systems, not the effect of an external electric field on one of the microphases, as is the case here. In our study, the free energy of the system is obtained by employing self-consistent field theory (SCFT), as in several of the previous calculations.^{28,30,31} As a consequence, the location of all charges is determined by a Poisson-Boltzmann equation. We also consider the effects of localization of charge within one block or the other and of the preference of the substrate for the blocks. We find for the case in which the substrate prefers the uncharged B polymers, as in the PMMA-PS system in which the PS is preferentially adsorbed,³² the critical field needed to reorient the system decreases markedly even with the small concentration of ions utilized in experiment, typically parts in 10^{-3} . Were the substrate to prefer the charged polymer, however, we find that the addition of free ions increases the field needed to reorient the system, in agreement with Putzel *et al.*¹⁴ Such a prediction could be easily tested.

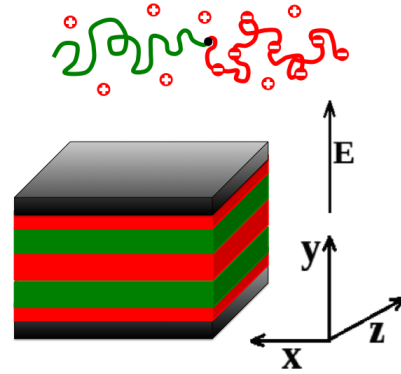


FIG. 1. A schematic diagram showing the model system examined in this work.

II. THEORETICAL MODEL

We consider a system in volume Ω of n_{AB} AB diblock copolymers with negatively charged A blocks and neutral B blocks. The index of polymerization is N_{AB} , so that the monomer density is $\rho_0 = n_{AB}N_{AB}/\Omega$. There are n_I mobile positive counter ions with density $\rho_I = n_I/\Omega$. We define dimensionless densities for polymers and ions as

$$\begin{aligned}\hat{\Phi}_A(\mathbf{r}) &= \frac{N_{AB}}{\rho_0} \sum_{i=1}^{n_{AB}} \int_0^f ds \delta(\mathbf{r} - \mathbf{R}_i^A(s)), \\ \hat{\Phi}_B(\mathbf{r}) &= \frac{N_{AB}}{\rho_0} \sum_{i=1}^{n_{AB}} \int_f^1 ds \delta(\mathbf{r} - \mathbf{R}_i^B(s)), \\ \hat{\Phi}_I(\mathbf{r}) &= \frac{1}{\rho_I} \sum_{i=1}^{n_I} \delta(\mathbf{r} - \mathbf{r}_i^I),\end{aligned}\quad (2.1)$$

where f is the fraction of A in the AB diblock copolymer chain. In the above equation, $\mathbf{R}^A(s)$ and $\mathbf{R}^B(s)$ are space curves specifying the position of polymer segment s along the chain. Similarly, \mathbf{r}^I represents the position of the ions in the system. We assume that the free ions are positively charged and that there is a uniform negative charge density on the A blocks. The degree of ionization of the A block is P_A and, as noted above, is quite small in experiment. Charge neutrality implies that the densities of ions and polymers is related by $\rho_I = P_A f \rho_0$. In our study, we ignore ion pairs.²⁹ The polymers are confined between plates separated by a distance L , with a potential difference V_0 between them, one which is maintained by a battery. The electrostatic energy of the system, which includes the battery, is a functional of the charge densities,

$$\begin{aligned}U[\hat{\Phi}_I, \hat{\Phi}_A] &= -\frac{1}{2} \int d\mathbf{r} \epsilon(\mathbf{r}) [\nabla V(\mathbf{r})]^2 \\ &\quad + \rho_0 P_A f \int d\mathbf{r} eV(\mathbf{r}) [\hat{\Phi}_I(\mathbf{r}) - \frac{\hat{\Phi}_A(\mathbf{r})}{f}],\end{aligned}\quad (2.2)$$

where e is the unit of charge and $V(\mathbf{r})$ is the electric potential which itself is a functional of the charge densities via the Maxwell equation,

$$\nabla \cdot [\epsilon(\mathbf{r}) \nabla V(\mathbf{r})] = -e P_A f \rho_0 [\hat{\Phi}_I(\mathbf{r}) - \hat{\Phi}_A(\mathbf{r})/f]. \quad (2.3)$$

The dielectric constant, $\epsilon(\mathbf{r})$, is position-dependent because the concentration of the two blocks varies in space. We

approximate the local dielectric constant by its volume-fraction weighted-average $\epsilon(\mathbf{r}) = \epsilon_0[\kappa_A \hat{\Phi}_A(\mathbf{r}) + \kappa_B \hat{\Phi}_B(\mathbf{r})]$. This approximation is clearly correct in the limits in which the volume fraction of one component approaches zero or unity. It captures the essential variation and has the advantage of simplicity, which is why it is commonly employed.^{24,29} We assume that the dielectric constants are independent of the applied field and take $\kappa_A = 6.0$, appropriate for PMMA, and $\kappa_B = 2.5$ appropriate for PS.

In addition to the electrostatic energy, there is also the energy of interaction between the A and B monomers with strength given by a Flory parameter χ_{AB} and the surface interaction of the polymers with the plates, $h(\mathbf{r})$. Furthermore, to test the idea that increased confinement of the mobile charges should have a large effect on the critical value of the aligning field, we control the relative solubility of the mobile charges by introducing an *ad hoc* repulsive interaction between them and the B monomers, an interaction of a strength we denote χ_{BI} .

The total energy functional is

$$\begin{aligned} H[\hat{\Phi}_A, \hat{\Phi}_B, \hat{\Phi}_I] &= U[\hat{\Phi}_I, \hat{\Phi}_A] + k_B T \rho_0 \int d\mathbf{r} [\chi_{AB} \hat{\Phi}_A(\mathbf{r}) \hat{\Phi}_B(\mathbf{r}) \\ &+ \chi_{BI} \hat{\Phi}_B(\mathbf{r}) \hat{\Phi}_I(\mathbf{r}) \\ &- k_B T \rho_0 \int d\mathbf{r} h(\mathbf{r}) [\hat{\Phi}_A(\mathbf{r}) - \hat{\Phi}_B(\mathbf{r})]. \end{aligned} \quad (2.4)$$

The thermodynamic properties of the system are conveniently described in the canonical ensemble, with fixed volume, temperature, and concentrations. The partition function is

$$\begin{aligned} Z &= \frac{1}{\lambda_I^{3n_I} n_I! \lambda_{AB}^{3n_{AB}} n_{AB}!} \left[\int \prod_{i=1}^{n_{AB}} D[\mathbf{R}_i^{AB}(s)] P_{AB}[\mathbf{R}_i^{AB}(s)] \right] \\ &\times \left[\int \prod_{i=1}^{n_I} d\mathbf{r}_i^I \int D[V(\mathbf{r})] \exp(-\beta H[\hat{\Phi}_A, \hat{\Phi}_B, \hat{\Phi}_I, V]) \right] \\ &\times \delta(\hat{\Phi}_A(\mathbf{r}) + \hat{\Phi}_B(\mathbf{r}) - 1), \end{aligned} \quad (2.5)$$

where $\beta \equiv 1/k_B T$, and λ_{AB} and λ_I are the thermal de Broglie wavelengths of the polymers and ions, respectively. We have assumed that the system is incompressible and have ignored the volume of the mobile ions. The polymers are treated as flexible Gaussian chains with configurations weighted by the Wiener measure,

$$P_{AB}[\mathbf{R}_i^{AB}(s)] \propto \exp\left[-\frac{3}{2N_{AB}b_o^2} \int_0^1 ds \left(\frac{d\mathbf{R}_i^{AB}(s)}{ds}\right)^2\right], \quad (2.6)$$

where b_o is the Kuhn length of the polymers.

We obtain the free energy of this system within the SCFT approximation. There are excellent reviews of this approximation as it is applied to polymeric systems³³⁻³⁵ and clear explications of its applications to systems with applied electric fields.^{15,24,35} For completeness, we provide a brief derivation in the [Appendix](#). As outlined there, within self-consistent field theory, $\beta F_{scft}/n_{AB}$, the free energy per polymer in units of $k_B T$, can be written as

$$\begin{aligned} \frac{\beta F_{scft}}{n_{AB}} &= -\ln\left(\frac{Q_{AB}}{n_{AB}}\right) - \frac{1}{\Omega} \int d\mathbf{r} \chi_{AB} N_{AB} \Phi_A(\mathbf{r}) \Phi_B(\mathbf{r}) \\ &+ \frac{1}{\Omega} \int d\mathbf{r} [\beta e V(\mathbf{r}) P_A N_{AB} f \Phi_I(\mathbf{r}) \\ &+ P_A N_{AB} f \Phi_I(\mathbf{r}) \ln \Phi_I(\mathbf{r})]. \end{aligned} \quad (2.7)$$

Here, $\Phi_I(\mathbf{r})$ is the ensemble average value of $\hat{\Phi}_I(\mathbf{r})$, the dimensionless density of the counter ions, in the presence of an electric potential $V(\mathbf{r})$,

$$\Phi_I(\mathbf{r}) = \frac{\exp[-\beta e V(\mathbf{r})]}{(1/\Omega) \int d\mathbf{r} \exp[-\beta e V(\mathbf{r})]}, \quad (2.8)$$

so that the last two terms in the above free energy are simply the free energy of the counter ions. The first term in the free energy, F_{scft} , is the free energy per polymer in the single polymer ensemble. As the latter double-counts all binary interactions, it has to be corrected by the binary interactions of the second term. The functions $\Phi_A(\mathbf{r})$ and $\Phi_B(\mathbf{r})$ are the ensemble-average values of the local volume fractions $\hat{\Phi}_A(\mathbf{r})$ and $\hat{\Phi}_B(\mathbf{r})$ in the single polymer chain ensemble with partition function Q_{AB} given below. Within self-consistent field theory, the potential is related via the Maxwell equation to the thermodynamic averages of the charge densities,

$$\nabla \cdot [\epsilon(\mathbf{r}) \nabla V(\mathbf{r})] = -e P_A f \rho_0 [\Phi_I(\mathbf{r}) - \Phi_A(\mathbf{r})/f], \quad (2.9)$$

and the local dielectric constant is now approximated by

$$\epsilon(\mathbf{r}) = \epsilon_0[\kappa_A \Phi_A(\mathbf{r}) + \kappa_B \Phi_B(\mathbf{r})]. \quad (2.10)$$

The partition function of the single polymer ensemble is obtained from the end-integrated propagator, $q(\mathbf{r}, s)$, which satisfies the modified diffusion equation,

$$\frac{\partial q(\mathbf{r}, s)}{\partial s} = [R_g^2 \nabla^2 - i W_A(\mathbf{r})] q(\mathbf{r}, s) \quad 0 \leq s \leq f \quad (2.11)$$

$$= [R_g^2 \nabla^2 - i W_B(\mathbf{r})] q(\mathbf{r}, s) \quad f < s \leq 1, \quad (2.12)$$

where R_g is the polymer's radius of gyration, and the fields are given by

$$\begin{aligned} \frac{i W_A(\mathbf{r})}{N_{AB}} &= \chi_{AB} \Phi_B(\mathbf{r}) - \frac{\kappa_A}{8\pi\rho_0\ell} [\nabla \beta e V(\mathbf{r})]^2 \\ &- P_A \beta e V(\mathbf{r}) - h(\mathbf{r}) - i \frac{\xi(\mathbf{r})}{N_{AB}}, \end{aligned} \quad (2.13)$$

$$\begin{aligned} \frac{i W_B(\mathbf{r})}{N_{AB}} &= \chi_{AB} \Phi_A(\mathbf{r}) + \chi_{BI} \Phi_I(\mathbf{r}) - \frac{\kappa_B}{8\pi\rho_0\ell} [\nabla \beta e V(\mathbf{r})]^2 \\ &+ h(\mathbf{r}) - i \frac{\xi(\mathbf{r})}{N_{AB}}, \end{aligned} \quad (2.14)$$

where $\ell \equiv \beta e^2/4\pi\epsilon_0$ is the Bjerrum length. The propagator satisfies the initial condition $q(\mathbf{r}, 0) = 1$. It is also convenient to define the propagator, $q^\dagger(\mathbf{r}, s)$, integrated from the other end of the polymer. It satisfies

$$\frac{\partial q^\dagger(\mathbf{r}, s)}{\partial s} = -[R_g^2 \nabla^2 - i W_A(\mathbf{r})] q^\dagger(\mathbf{r}, s) \quad 0 \leq s \leq f \quad (2.15)$$

$$= -[R_g^2 \nabla^2 - i W_B(\mathbf{r})] q^\dagger(\mathbf{r}, s) \quad f < s \leq 1, \quad (2.16)$$

with the boundary condition $q^\dagger(\mathbf{r}, 1) = 1$. The single polymer partition function is then obtained from

$$Q_{AB}[W_a, W_B] = \frac{1}{\lambda_{AB}^3} \int d\mathbf{r} q(\mathbf{r}, 1), \quad (2.17)$$

and the ensemble averages of the dimensionless monomer densities from

$$\Phi_A(\mathbf{r}) = \frac{\Omega}{\lambda_{AB}^3 Q_{AB}} \int_0^f ds q(\mathbf{r}, s) q^\dagger(\mathbf{r}, s), \quad (2.18)$$

$$\Phi_B(\mathbf{r}) = \frac{\Omega}{\lambda_{AB}^3 Q_{AB}} \int_f^1 ds q(\mathbf{r}, s) q^\dagger(\mathbf{r}, s). \quad (2.19)$$

The field $i\xi(\mathbf{r})$ in Eqs. (2.13) and (2.14) is a Lagrange multiplier adjusted so that the incompressibility condition

$$\Phi_A(\mathbf{r}) + \Phi_B(\mathbf{r}) = 1 \quad (2.20)$$

is satisfied locally. Equations (2.8), (2.9), and (2.18) constitute the Poisson-Boltzmann equation.

The Maxwell equation (2.9) and five equations (2.13), (2.14), and (2.18)–(2.20) determine self-consistently the electrostatic potential, $V(\mathbf{r})$, and the five unknown fields $W_A(\mathbf{r})$, $W_B(\mathbf{r})$, $\Phi_A(\mathbf{r})$, $\Phi_B(\mathbf{r})$, and $\xi(\mathbf{r})$. They are solved in two dimensions using a combination of pseudo-spectral and finite-difference methods with appropriate initial and boundary conditions for a given phase.^{36,37}

We fix the potential difference across the thin film by setting the value of electrostatic potential at the top and bottom surfaces to $V_{\text{top}} = 0$ and $V_{\text{bottom}} = V_0$. In addition, we keep the height of the film constant at $L = 2d_0$, where d_0 is the natural period of the lamellae for neutral AB diblock copolymers in bulk. We choose the height to be an integer value of d_0 as the parallel configuration is then most stable.^{38,39} Therefore, the calculated value of the electric field needed to reorient the film will be an upper bound. We take the strength of interaction between the A and B species to be $\chi_{AB}N_{AB} = 20$. Finally, we must specify the interaction, $h(\mathbf{r})$, between the polymers and the substrate. The interactions are complex and their theoretical description is difficult, as noted by Messina *et al.* in their review.⁴⁰ However, our interest here is not in the origin of this attraction between substrate and polymer, but in the value of an imposed electric field needed to overcome the effect of this interaction which favors the parallel configuration. Hence, we approximate the interaction by the simple function $h(\mathbf{r})$ which takes the value μ at the plates and which is zero otherwise.

III. RESULTS

In this section, we present our results on the phase behavior of the charged AB diblock copolymers as a function of electric field strength, charge density, and surface interactions. The blocks are lamellae forming with equal polymerization index so the volume fraction, f , of A monomer is $1/2$. We consider two scenarios. In the first, the neutral B species interacts favorably with the top and bottom surfaces, which results in the aggregation of the B segments to a thickness of about $d_0/4$ at both substrate interfaces (Fig. 1). In the second, the charged A species interacts favorably with the top and bottom substrates.

We now consider the first scenario. In this case, the polymer/substrate interaction favors the parallel morphology with the B species aggregated at the top and bottom surfaces. One can bring about a phase transition from the parallel to the perpendicular phase by applying an external field

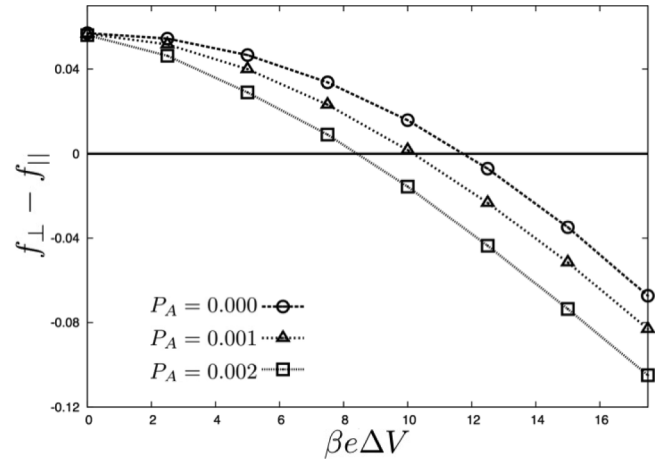


FIG. 2. Difference in the free energy between the perpendicular and the parallel phases as a function of applied voltage for copolymers characterized by $\chi_{AB}N_{AB} = 20$, $\chi_{BI}N_{AB} = 0$, $\kappa_A = 6.0$, $\kappa_B = 2.5$, and $\mu = -1$.

perpendicular to the substrate. Figure 2 presents the free energy difference between the perpendicular and parallel morphologies as a function of dimensionless electric potential $\beta e \Delta V$ for neutral and charged systems. Here, we consider copolymers in which the fraction, P_A , of polymer which is ionized is small, $P_A = 0.0, 0.001$, and 0.002 . This is comparable to experiment.^{26,32} We note that for both neutral and charged thin films, the parallel phase has the lowest free energy at small values of ΔV . An increase in the applied voltage results in a phase transition from the parallel to the perpendicular phase at some critical voltage ΔV_c .

From Figure 2, we see that the addition of mobile charges does indeed lower the voltage required to orient the lamellae from the parallel to the perpendicular orientation. Furthermore, the reduction can be large, even for small amounts of added free charge. With the parameters chosen in the figure, addition of only two parts per thousand of mobile ions reduces the critical voltage by about 30%. This can be understood in terms of the polarization in the two orientations. In the case considered here, the positive counter ions are free to move throughout the system; however, the negative charges are bound to the A chains and thus are confined within the A domains. In the presence of an applied external field, charge separation in the perpendicular phase is of the order of the film thickness $L = 2d_0$, where d_0 is the period of the AB system in bulk. In the parallel orientation, however, the interposition of a layer of the neutral B polymers of thickness $d_0/4$ between the anode and the nearest lamella of negatively charged A polymers results in a separation of charge which is no greater than $L - d_0/4 = 7d_0/4$, significantly smaller than that in the perpendicular phase. Therefore, the addition of charge favors the perpendicular phase and lowers the voltage required to reorient the lamellae domains. Note however that the difference in charge separation in the two orientations, $d_0/4$, does not scale with the film thickness as the total free energy does. Hence as the thickness of the film increases, we expect the magnitude of the reduction in critical field due to the ions to decrease.

To further examine the effect of charge separation on the critical voltage, we consider a system in which the positive counter ions are increasingly confined to the A domains. We

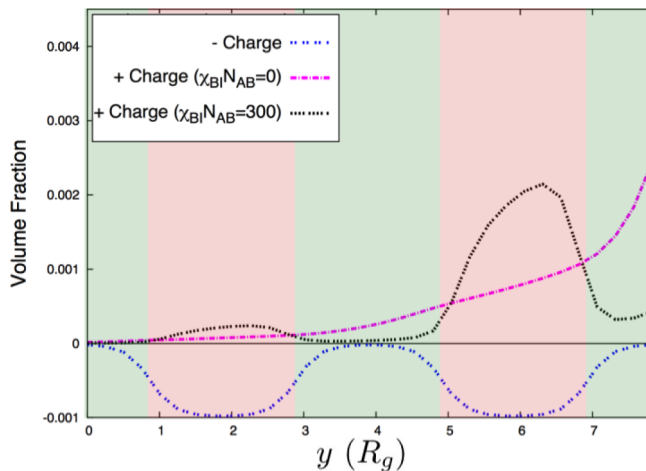


FIG. 3. One dimensional charge distribution for the charged AB system with $P_A = 0.001$, $\chi_{AB}N_{AB} = 20$, $\kappa_A = 6.0$, and $\kappa_B = 2.5$ with $\chi_{BI} = 0$ and $\chi_{BI} = 300$. The positive and negative electrodes are at $y = 0$ and $y = 8R_g$, respectively. The AB polymer distribution is shown as red/green shades, respectively, where in this case, B species are attracted by the substrates.

achieve this by introducing a repulsive interaction, $\chi_{BI}N_{AB}$, between the positive counter ions and the B monomers. As shown in Fig. 3, an increase in $\chi_{BI}N_{AB}$ results in a depletion of the positive ions from the domain near the negative electrode, thus resulting in a smaller separation of charge. The constraint of the confinement increases the free energy of both orientations at a rate proportional to the average overlap of ions and B monomers. It is not difficult to see that this overlap is large in the parallel configuration at the plate at which the ions tend to aggregate, a plate covered by B polymers. The free energy of this configuration, favored in the absence of an applied field, rapidly increases with ion confinement. The overlap is much lower in the perpendicular orientation; hence, the free energy advantage of the parallel phase rapidly decreases with the consequence that the critical voltage needed to bring about reorientation decreases.

The effect of confinement is evident from Fig. 4 which shows the critical voltage ΔV_c as a function of the fraction, P_A , of free ions for various values of the interaction parameter $\chi_{BI}N_{AB}$. As can be seen, the effect of the confinement of the

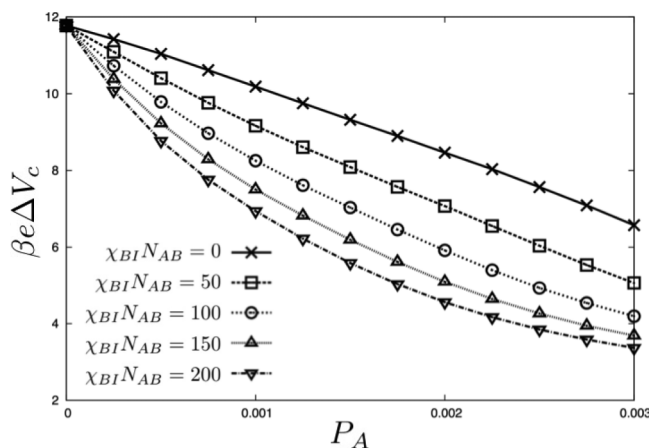


FIG. 4. The critical voltage ΔV_c plotted as a function of the degree of ionization P_A for a system with $\chi_{AB}N_{AB} = 20$, $\kappa_A = 6.0$, $\kappa_B = 2.5$, and $\mu = -1$.

ions is quite large. In terms of charge separation, we expect it to scale with the film thickness L in the perpendicular configuration, but to be independent of L in the confined, parallel configuration. Hence in this case, the difference in charge separation does scale with film thickness, and we expect the reduction in critical field due to the ions to persist as the film thickness increases.

We now consider the effects of the strength of the surface interactions, μ , on the voltage required to reorient the lamellae morphologies. Larger magnitudes of the negative surface field, μ , correspond to a greater attractive interaction between the substrate and the B monomers relative to the A monomers. We begin with the simple case of neutral AB diblock copolymer thin films, subjected to an applied external voltage. Figure 5 presents the phase diagram of the neutral AB diblock copolymer thin films in the $\beta e \Delta V - \mu$ plane. Here, we consider three distinct phases: the parallel (Para), the perpendicular (Perp), and the mixed (Mix) phases. The mixed phase is composed of parallel and perpendicular morphologies (see Figure 6). For systems with $\mu = 0$, application of an infinitesimal electric field results in the instability of the parallel phase. As expected, a non-vanishing surface field stabilizes the parallel phase. The critical voltage required to reorient the lamellae from the parallel to the perpendicular phase increases as the strength of the surface interaction increases as expected. There exist a critical surface interaction μ_c beyond which an increase in the voltage results in a phase transition from the parallel to the mixed phase. In this region of the phase space, the surface interactions are strong enough to induce the formation of a thin partial wetting layer of B species at both surfaces. Away from the substrate, however, the electric field results in the formation of perpendicular domains. Because of this surface layer of B monomers, the cost of reorienting the lamellae to align with the field is not as great as in the simple perpendicular phase. Hence, the rate at which the critical field increases with surface field is less in going from the parallel configuration to the mixed phase than it is in going from the parallel phase to the simple perpendicular phase. This is an effect that cannot be captured by the toy models employed

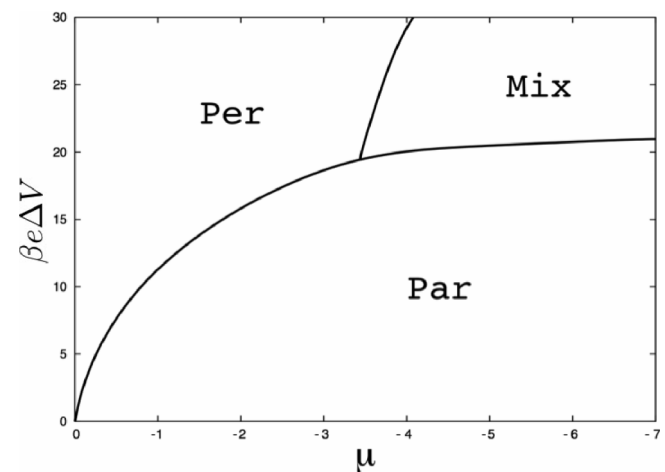


FIG. 5. Phase diagram for the neutral AB system with $P_A = 0$, $\chi_{AB}N_{AB} = 20$, $\chi_{BI}N_{AB} = 0$, $\kappa_A = 6.0$, and $\kappa_B = 2.5$ in the $\beta e \Delta V - \mu$ plane. The Per, Par, and Mix phases correspond to the perpendicular, parallel, and mixed phases, respectively.

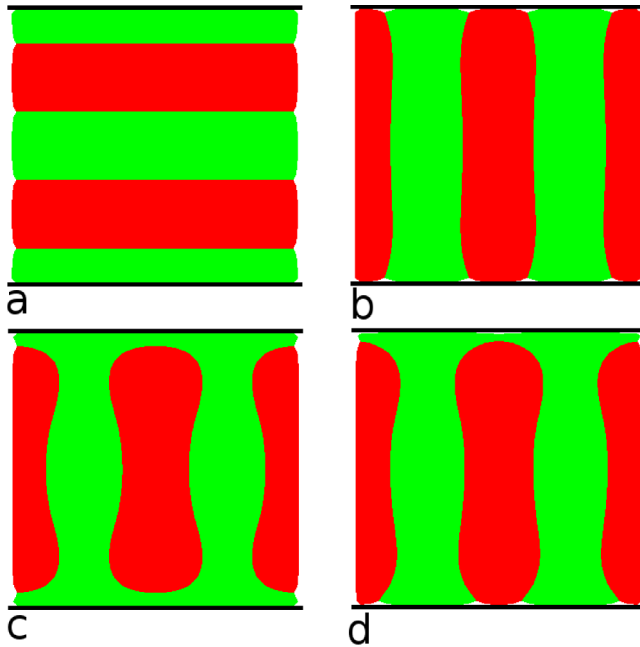


FIG. 6. Density profiles for the (a) parallel, (b) perpendicular, (c) mixed, and (d) partially mixed phases. Here, B species are green and A species are red. The top/bottom electrodes are negatively/positively charged.

previously.¹⁴ Figures 6(a)–6(c) show the density profiles for the parallel, the perpendicular, and the mixed phases.

To the above uncharged system, we add a uniform negative charge distribution to the A blocks and positive counter ions. The effect on the phase diagram in the $\beta e\Delta V - \mu$ plane is shown in Figure 7 for a system with $P_A = 0.001$. As in the neutral system, at $\mu = 0$ the parallel phase becomes unstable when subjected to an infinitesimally small voltage. A non-zero μ stabilizes the parallel phase and results in an increase in the critical voltage. What is new in the charged system is the presence of a partially mixed phase (denoted P-Mix in Figure 7), which appears between the perpendicular and the mixed phases. To determine the difference between the two mixed phases, we examine their density profiles.

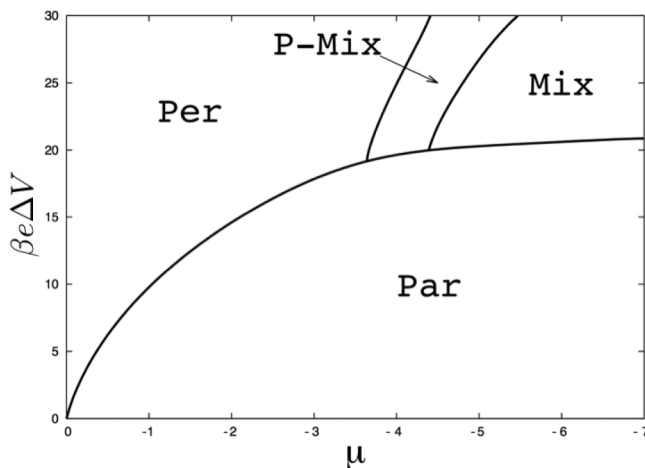


FIG. 7. Phase diagram for the charged AB system with $P_A = 0.001$, $\chi_{AB}N_{AB} = 20$, $\chi_{BI}N_{AB} = 0$, $\kappa_A = 6.0$, and $\kappa_B = 2.5$ in the $\Delta V - \mu$ plane. The Per, Par, Mix, and P-Mix phases correspond to the perpendicular, parallel, mixed, and partially mixed phases, respectively.

Figures 6(c) and 6(d) present the density profiles for the mixed and partially mixed phases, respectively. In the charged system, the parallel, perpendicular, and mixed phases are similar to those observed in the neutral system. The difference between the two mixed phases is seen as a difference in surface behavior. The electrostatic interaction between the negative A segments and the charged electrodes favors a partial wetting of the positively charged plate (bottom surface) by the A monomers, whereas the surface interaction, μ , favors the partial wetting of both top and bottom surfaces by the B species. The presence of charge introduces an asymmetry which results in the formation of the partially mixed phase, Figure 6(d). For larger surface fields, the asymmetry is less important and the B species will partially wet both top and bottom surfaces, Figure 6(c).

We now consider the scenario in which the charged A species is attracted to the top and bottom surfaces. In this case, in the absence of an external electric field, the parallel phase with the A species partially wetting the polymer/substrate interface is the most stable structure. We begin by analyzing the phase transition between the parallel and perpendicular morphologies as a function of applied external voltage. Figure 8 presents the difference in the perpendicular and parallel free energies as a function of external voltage ΔV for neutral and charged thin films with $P_A = 0, 0.001$ and 0.002 , respectively. As expected, for both neutral and charged copolymers, the parallel phase has the lowest free energy at small values of applied external voltage. Increase in ΔV results in a phase transition from the parallel to perpendicular phase at some critical ΔV_c value. In contrast to the previous case, in which the neutral B polymers were attracted to the surfaces, adding charge now *increases* the critical voltage required to reorient the lamellae from the parallel to the perpendicular orientation. An increase in P_A further *stabilizes* the parallel phase. To examine this effect, we analyze the charge distribution within the system.

In the previous case with the neutral B species partially wetting the substrate interfaces, the charge separation in the parallel phase was smaller than the charge separation in the perpendicular phase, which resulted in a decrease in ΔV_c with

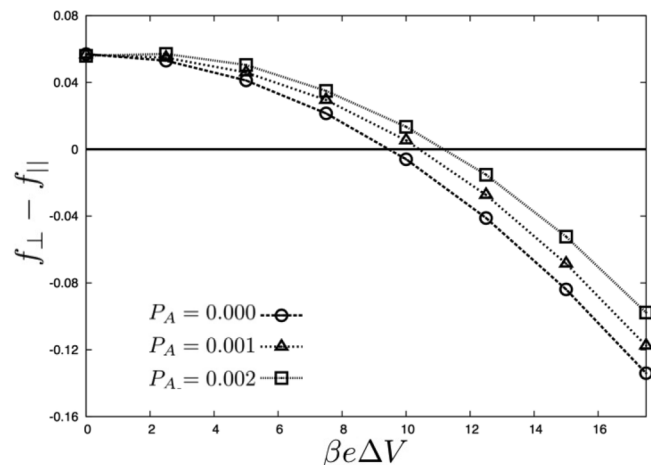


FIG. 8. Difference in the free energy between the perpendicular and the parallel phases for a system with $\chi_{AB}N_{AB} = 20$, $\chi_{BI}N_{AB} = 0$, $\kappa_A = 6.0$, $\kappa_B = 2.5$, and $\mu = 1$.

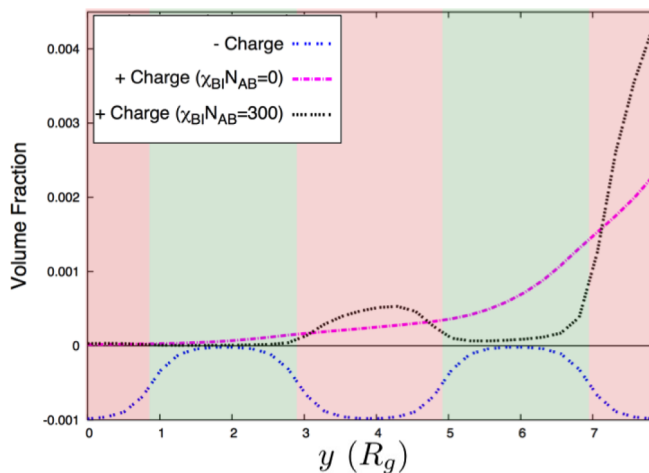


FIG. 9. One dimensional charge distribution for the charged AB system with $P_A = 0.001$, $\chi_{AB}N_{AB} = 20$, $\kappa_A = 6.0$, and $\kappa_B = 2.5$ with $\chi_{BI} = 0$ and $\chi_{BI} = 300$. The positive and negative electrodes are at $y = 0$ and $y = 8R_g$, respectively. The AB polymer distribution is shown as red/green shades, respectively, where in this case, A species are attracted by the substrates.

the addition of free ions. In the present scenario, the charged A species partially wet the top and bottom surfaces in the parallel configuration, which in the presence of an applied external voltage would result in a charge separation of the order of film thickness L . This is comparable to the magnitude of charge separation in the perpendicular phase. In fact, in a charged system the parallel configuration is more favorable since both positive and negative charges coat the entire top and bottom plates, while this is only possible to a lesser extent in the perpendicular phase. For this reason, an increase in P_A stabilizes the parallel configuration and thus increases the critical voltage ΔV_c .

We further explore this idea by considering the effect of charge confinement on the critical voltage. As before, we confine the ions by introducing a repulsive interaction between the positive ions and B polymer. The effect of this confinement is shown in Figure 9. An increase in $\chi_{BI}N_{AB}$ results in a greater aggregation of positive ions at the negative electrode and hence a greater separation of charge thereby stabilizing the phase. Again the effect of the repulsive interaction on the free energy

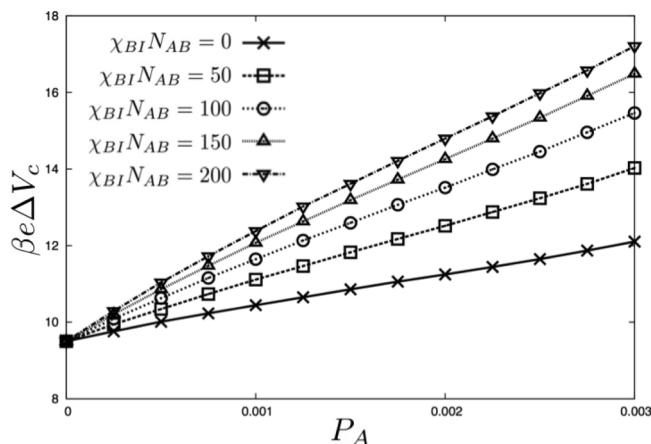


FIG. 10. The critical voltage ΔV_c plotted as a function of the degree of ionization P_A for a system with $\chi_{AB}N_{AB} = 20$, $\kappa_A = 6.0$, $\kappa_B = 2.5$, and $\mu = 1$.

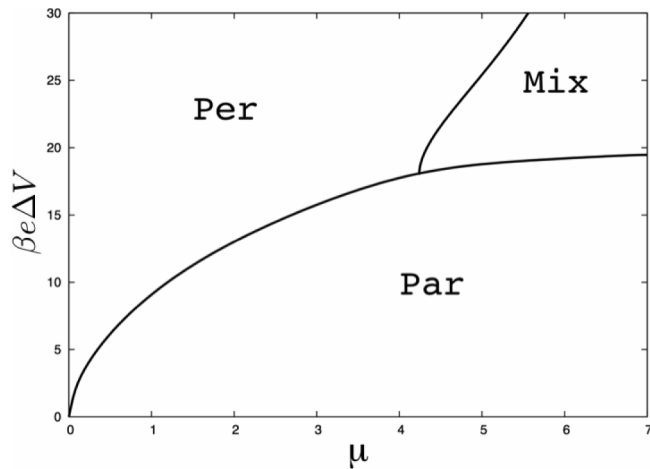


FIG. 11. Phase diagram for the neutral AB system with $P_A = 0$, $\chi_{AB}N_{AB} = 20$, $\chi_{BI}N_{AB} = 0$, $\kappa_A = 6.0$, and $\kappa_B = 2.5$ in the $\Delta V - \mu$ plane. The Per, Par, and Mix phases correspond to the perpendicular, parallel, and mixed phases, respectively.

is proportional to the ensemble average of the overlap of ions and B monomers. In the parallel orientation in which the ions are attracted to one plate which is covered by A monomers, the overlap is small so that the free energy is not increased significantly. The overlap is clearly larger in the perpendicular orientation so the free energy of this phase does increase significantly with the imposition of this interaction. Hence, the free energy advantage of the parallel phase increases with the confinement of the ions to the A blocks. Figure 10 shows the critical voltage ΔV_c as a function of the degree of ionization P_A for various $\chi_{BI}N_{AB}$ values.

We now consider the effect of surface interaction on the voltage required to reorient the lamellae domains from the parallel to the perpendicular orientation. As before, we first consider the phase behavior of neutral AB diblock thin films and then extend our study to the case with charge. Figure 11 presents the phase diagram for the neutral AB system ($P_A = 0$) for a system with $\chi_{AB}N_{AB} = 20$, $\chi_{BI}N_{AB} = 0$, $\kappa_A = 6.0$, and $\kappa_B = 2.5$ in the $\beta e \Delta V - \mu$ plane. The phase behavior seen here is similar to that observed in the case in which the neutral

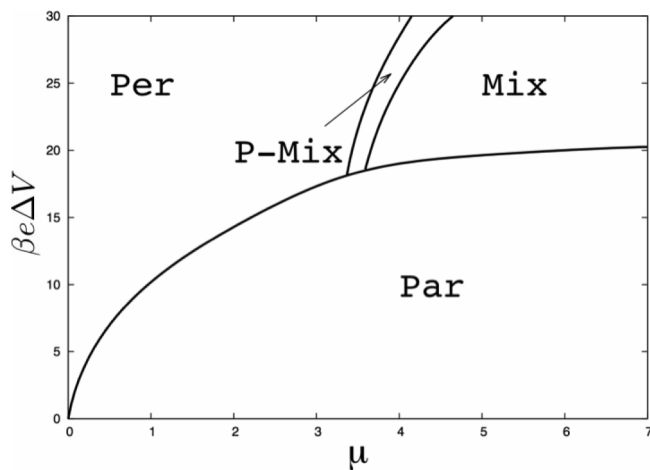


FIG. 12. Phase diagram for the charged AB system with $P_A = 0.003$, $\chi_{AB}N_{AB} = 20$, $\chi_{BI}N_{AB} = 0$, $\kappa_A = 6.0$, and $\kappa_B = 2.5$ in the $\beta e \Delta V - \mu$ plane. The Per, Par, Mix, and P-Mix phases correspond to the perpendicular, parallel, mixed, and partially mixed phases, respectively.

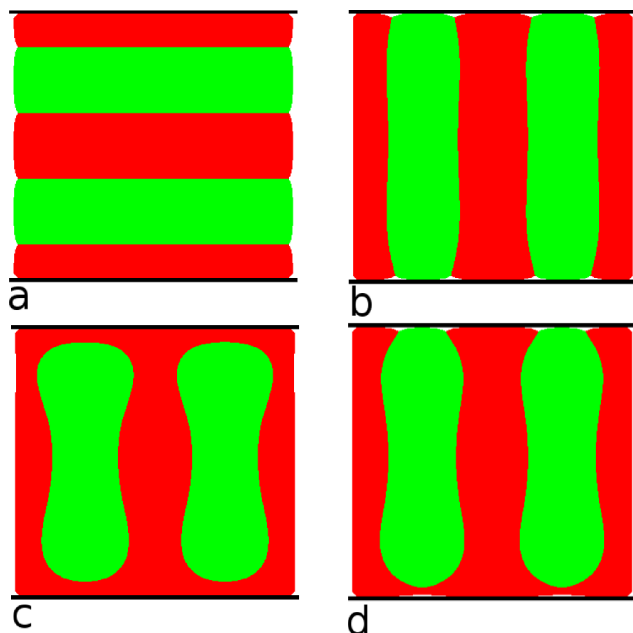


FIG. 13. Density profiles for the (a) parallel, (b) perpendicular, (c) mixed, and (d) partially mixed phases. Here, B species are colored green and A species are colored red. The top/bottom electrodes are negatively/positively charged.

B species was attracted to the substrates, Figure 5. When the applied external voltage is small, the parallel configuration has the lowest free energy. As we increase ΔV , depending on the strength of the surface interaction μ , two scenarios are possible. When the surface interaction is weak, we observe a phase transition from the parallel to the perpendicular phase. When the surface interaction is strong, the phase transition is between the parallel and the mixed phases.

We now turn to the phase behavior of the charged AB diblock copolymer thin films. Figure 12 presents the phase behavior of the charged AB system with $P_A = 0.003$, $\chi_{AB}N_{AB} = 20$, $\chi_{BI}N_{AB} = 0$, $\kappa_A = 6.0$, and $\kappa_B = 2.5$ in the ΔV - μ plane. The phase behavior seen here is similar to that given in Figure 7, in which the addition of free ions results in the formation of a new partially mixed phase. The density profiles for the parallel, perpendicular, mixed, and partially mixed phases are presented in Figure 13. As before, the addition of charge breaks the symmetry in the effective interaction between the negatively charged A polymers and the positive/negative electrodes. In this scenario, there is a favorable electrostatic and surface interaction between the negatively charge A polymers and positively charged bottom substrate, while there is only the favorable surface interaction between the A species and the negatively charged top surface. At intermediate surface interactions, the A polymers partially wet the bottom surface; however, the extent of such wetting is less at the top plate. At large values of μ , the surface interactions dominate and the A polymers completely cover the top and bottom surfaces resulting in the formation of the mixed phase.

IV. CONCLUSION

We have examined the effect of the addition of free ions on the magnitude of the external voltage required to reorient

a lamellae phase from the parallel configuration to a phase in which domains form perpendicular to the substrates. It was originally suggested by Tsori *et al.*^{22,23} that such an addition would reduce the critical voltage ΔV_c . A toy model,¹⁴ which consisted of rigid dielectric media, not block copolymers, indicated that this could be the case provided that certain conditions were met. In particular, Putzel *et al.* suggested that adding charge to a system in which the charged domains are attracted to the surfaces could in fact increase the critical voltage.¹⁴

In our study, we have examined the behavior of a dielectric material which consists of block copolymers. We have considered two different scenarios, one in which the neutral B blocks are favored by the top and bottom surfaces and the other where the charged A blocks are favored. In both cases, we have examined the effect of adding charge on the critical voltage required to reorient the lamellae from the parallel to the perpendicular morphology. We have also examined the phase behavior of the system as a function of voltage and surface interactions for both neutral and charged films.

In the first case, in which the neutral B polymers were attracted to the surfaces we found that adding charge significantly lowered the critical voltage required to reorient the lamellae from the parallel to the perpendicular orientation. We argued that the decrease in the critical voltage is due to the difference in the magnitude of charge separation in the parallel and perpendicular orientations. We further examined the effect of charge separation on the critical voltage by confining the positive counter ions to the charged A domains. In the confined case in which the difference in magnitude of charge separation between the parallel and perpendicular phase was increased, we found that adding charge would result in much greater reduction in the critical voltage. These results are in accord with experiment.^{25,26}

We then considered a scenario in which the charged A polymers were attracted to the substrate surfaces. In this case, adding charge further stabilized the parallel phase and thus resulted in an increase in the critical voltage. We argued that in this scenario, there is no difference in the magnitude of charge separation between the parallel and perpendicular phases. However, in the parallel phase, both the negative and positive ions could coat the entire top and bottom plates, while this coverage is only partial in the perpendicular phase. When the positive counter ions are confined to the A domains, we found that an increase in their density results in an increase in the critical voltage. This interesting behavior should be amenable to experimental verification.

ACKNOWLEDGMENTS

M.S. would like to thank David Andelman for seminal conversations. This work was supported by the Natural Sciences and Engineering Research Council (NSERC) of Canada, the U.S.-Israel Binational Science Foundation (BSF) under Grant No. 2012060, and the National Science Foundation under Grant No. DMR-1203282. The computation was made possible by the facilities of the Shared Hierarchical Academic Research Computing Network (SHARCNET).

APPENDIX: THEORETICAL FRAMEWORK

We begin with partition function Eq. (2.5),

$$Z = \left(\frac{1}{\lambda_I^{3n_I} n_I! \lambda_{AB}^{3n_{AB}} n_{AB}!} \right) \times \left[\int \prod_{i=1}^{n_{AB}} D[\mathbf{R}_i^{AB}(s)] P_{AB}[\mathbf{R}_i^{AB}(s)] \right] \times \left[\int \prod_{i=1}^{n_I} d\mathbf{r}_i^I \right] \exp(-\beta H[\hat{\Phi}_A, \hat{\Phi}_B, \hat{\Phi}_I]) \times \delta(\hat{\Phi}_A(\mathbf{r}) + \hat{\Phi}_B(\mathbf{r}) - 1), \quad (\text{A1})$$

where

$$H[\hat{\Phi}_A, \hat{\Phi}_B, \hat{\Phi}_I] = U[\hat{\Phi}_I, \hat{\Phi}_A] + k_B T \rho_0 \times \int d\mathbf{r} [\chi_{AB} \hat{\Phi}_A(\mathbf{r}) \hat{\Phi}_B(\mathbf{r}) + \chi_{BI} \hat{\Phi}_B(\mathbf{r}) \hat{\Phi}_I(\mathbf{r})] - k_B T \rho_0 \int d\mathbf{r} h(\mathbf{r}) [\hat{\Phi}_A(\mathbf{r}) - \hat{\Phi}_B(\mathbf{r})] \quad (\text{A2})$$

and

$$U[\hat{\Phi}_I, \hat{\Phi}_A] = -\frac{1}{2} \int \epsilon(\mathbf{r}) [\nabla V(\mathbf{r})]^2 d\mathbf{r} + \rho_0 P_A f \times \int eV(\mathbf{r}) [\hat{\Phi}_I(\mathbf{r}) - \frac{\hat{\Phi}_A(\mathbf{r})}{f}] d\mathbf{r}. \quad (\text{A3})$$

The electrostatic potential is itself a functional of $\hat{\Phi}_A$ and $\hat{\Phi}_I$ as it is a solution of the Maxwell equation

$$\nabla \cdot [\epsilon(\mathbf{r}) \nabla V(\mathbf{r})] = -e P_A f \rho_0 [\hat{\Phi}_I(\mathbf{r}) - \hat{\Phi}_A(\mathbf{r})/f], \quad (\text{A4})$$

with a boundary condition of the specified voltages on the plates. Given that Maxwell's equations for the electric and displacement fields have been used to derive the electrostatic energy, Eq. (A3), it may not be too surprising that this energy is an extremum with respect to the potential V , i.e., $\delta U[V]/\delta V = 0$ leads to Eq. (A4). We now derive the SCFT approximation to the free energy. To make the self-consistent field approximation transparent, it is convenient to rewrite the partition function by introducing auxiliary fields $W_A(\mathbf{r})$ and $\Phi_A(\mathbf{r})$, and $W_B(\mathbf{r})$ and $\Phi_B(\mathbf{r})$ via the identities

$$\int DW_A D\Phi_A \exp \left\{ \frac{n_{AB}}{\Omega} \int d\mathbf{r} iW_A(\mathbf{r}) [\Phi_A(\mathbf{r}) - \hat{\Phi}_A(\mathbf{r})] \right\} = 1, \quad (\text{A5})$$

$$\int DW_B D\Phi_B \exp \left\{ \frac{n_{AB}}{\Omega} \int d\mathbf{r} iW_B(\mathbf{r}) [\Phi_B(\mathbf{r}) - \hat{\Phi}_B(\mathbf{r})] \right\} = 1. \quad (\text{A6})$$

Similarly, we utilize

$$\int D\Phi_I DW_I \exp \left\{ \rho_I \int d\mathbf{r} iW_I(\mathbf{r}) [\Phi_I(\mathbf{r}) - \hat{\Phi}_I(\mathbf{r})] \right\} = 1. \quad (\text{A7})$$

With the introduction of these fields, we rewrite the incompressibility constraint in the form

$$\delta(\hat{\Phi}_A(\mathbf{r}) + \hat{\Phi}_B(\mathbf{r}) - 1) = \int D\xi \exp \left\{ \frac{n_{AB}}{\Omega} \int d\mathbf{r} i\xi(\mathbf{r}) [\Phi_A(\mathbf{r}) + \Phi_B(\mathbf{r}) - 1] \right\}. \quad (\text{A8})$$

Utilizing the above identities, we can rewrite the partition function in the form

$$Z = \int DW_A D\Phi_A DW_B D\Phi_B DW_I D\Phi_I D\xi DV \exp \{-\beta \mathcal{F}[W_A, \Phi_A, W_B, \Phi_B, W_I, \Phi_I, \xi]\}, \quad (\text{A9})$$

where

$$\begin{aligned} \beta \mathcal{F} = & -n_I \ln(Q_I[iW_I]/n_I) - n_{AB} \ln(Q_{AB}[iW_A, iW_B]/n_{AB}) \\ & - f P_A \rho_0 \int d\mathbf{r} iW_I(\mathbf{r}) \Phi_I(\mathbf{r}) - \beta \rho_0 \int d\mathbf{r} \frac{1}{2\rho_0} \epsilon(\mathbf{r}) (\nabla V(\mathbf{r}))^2 + \beta f P_A \rho_0 \int d\mathbf{r} V(\mathbf{r}) e[\Phi_I(\mathbf{r}) - \Phi_A(\mathbf{r})/f] \\ & + \rho_0 \int d\mathbf{r} [\chi_{AB} \Phi_A(\mathbf{r}) \Phi_B(\mathbf{r}) + \chi_{BI} \Phi_B(\mathbf{r}) \Phi_I(\mathbf{r})] - \rho_0 \int d\mathbf{r} h(\mathbf{r}) [\Phi_A(\mathbf{r}) - \Phi_B(\mathbf{r})] \\ & - \frac{n_{AB}}{\Omega} \int d\mathbf{r} [iW_A(\mathbf{r}) \Phi_A(\mathbf{r}) + iW_B(\mathbf{r}) \Phi_B(\mathbf{r}) + i\xi(\mathbf{r}) (\Phi_A(\mathbf{r}) + \Phi_B(\mathbf{r}) - 1)]. \end{aligned} \quad (\text{A10})$$

In the above equation, $Q_{AB}[iW_A, iW_B]$ is the partition function of a single polymer chain in the fields iW_A and iW_B , and $Q_I[iW_I]$ is the partition function of a single ion in the field iW_I ,

$$Q_I[iW_I] \equiv \frac{\Omega}{\lambda_I^3} \int d\mathbf{r} \frac{\exp\{-iW_I(\mathbf{r})\}}{\Omega}. \quad (\text{A11})$$

In addition, the charge neutrality condition, $\rho_I = P_A f \rho_0$, has been used. The electrostatic potential, $V(\mathbf{r})$, is obtained from the Maxwell equation

$$\nabla \cdot [\epsilon(\mathbf{r}) \nabla V(\mathbf{r})] = -e P_A f \rho_0 [\Phi_I(\mathbf{r}) - \Phi_A(\mathbf{r})/f], \quad (\text{A12})$$

which is completely equivalent to Eq. (A4) because of the identities Eqs. (A5) and (A7). Thus, at this point, the electrostatic potential varies with the distinct configurations of charges.

The above transformations are exact, but the integrals cannot be carried out in general. Self-consistent field theory results from extremizing the functional $\beta\mathcal{F}$ with respect to the seven functions on which it depends. Extremizing with respect to W_A and W_B , we obtain

$$\Phi_A(\mathbf{r}) = \langle \hat{\Phi}_A(\mathbf{r}) \rangle, \quad (\text{A13})$$

$$\Phi_B(\mathbf{r}) = \langle \hat{\Phi}_B(\mathbf{r}) \rangle, \quad (\text{A14})$$

where $\langle \hat{\Phi}_A(\mathbf{r}) \rangle$ is the average of $\hat{\Phi}_A(\mathbf{r})$ in the ensemble of a single polymer in the fields iW_A and iW_B , and similarly for $\langle \hat{\Phi}_B(\mathbf{r}) \rangle$. Variation with respect to W_I yields

$$\Phi_I(\mathbf{r}) = \frac{\exp[-iW_I(\mathbf{r})]}{(1/\Omega) \int \exp[-iW_I(\mathbf{r})] d\mathbf{r}}. \quad (\text{A15})$$

Extremizing with respect to Φ_A , Φ_B , and Φ_I and utilizing the fact that \mathcal{F} , like the electrostatic energy U , is an extremum with respect to variations in the potential V ensuring that $\{\delta\mathcal{F}/\delta V[\Phi_A, \Phi_I]\} \{\delta V/\delta \Phi_\alpha\} = 0, \alpha = A, B, I$, we obtain

$$\begin{aligned} \frac{iW_A(\mathbf{r})}{N_{AB}} &= \chi_{AB}\Phi_B(\mathbf{r}) - \frac{\kappa_A}{8\pi\ell\rho_0}[\nabla\beta eV(\mathbf{r})]^2 \\ &\quad - P_A\beta eV(\mathbf{r}) - h(\mathbf{r}) - i\frac{\xi(\mathbf{r})}{N_{AB}}, \end{aligned} \quad (\text{A16})$$

$$\begin{aligned} \frac{iW_B(\mathbf{r})}{N_{AB}} &= \chi_{AB}\Phi_A(\mathbf{r}) + \chi_{BI}\Phi_I(\mathbf{r}) \\ &\quad - \frac{\kappa_B}{8\pi\ell\rho_0}[\nabla\beta eV(\mathbf{r})]^2 + h(\mathbf{r}) - i\frac{\xi(\mathbf{r})}{N_{AB}}, \end{aligned} \quad (\text{A17})$$

$$iW_I(\mathbf{r}) = \beta eV(\mathbf{r}). \quad (\text{A18})$$

Finally, variation with respect to ξ produces

$$\Phi_A(\mathbf{r}) + \Phi_B(\mathbf{r}) = 1. \quad (\text{A19})$$

The value of the electrostatic potential averaged over all configurations of the charges, $\langle V[\hat{\Phi}_A, \hat{\Phi}_I] \rangle$, is approximated in self-consistent field theory by the value of the same functional evaluated at the ensemble average values of the charge densities $V[\langle \hat{\Phi}_A \rangle, \langle \hat{\Phi}_I \rangle]$.

Similarly, the free energy in the self-consistent field approximation, F_{scft} , is the value of the functional \mathcal{F} above evaluated with the functions that satisfy the self-consistent equations

$$\frac{\beta F_{scft}}{n_{AB}} = -P_A f N_{AB} \ln(Q_I/n_I) - \ln(Q_{AB}/n_{AB}) \quad (\text{A20})$$

$$\begin{aligned} & - \frac{1}{\Omega} \int d\mathbf{r} \chi_{AB} N_{AB} \Phi_A(\mathbf{r}) \Phi_B(\mathbf{r}) \\ & - \frac{1}{\Omega} \int d\mathbf{r} i \xi(\mathbf{r}). \end{aligned} \quad (\text{A21})$$

We can eliminate the explicit appearance of the partition function Q_I by the use of Eqs. (A18) and (A15)

$$-\ln Q_I/n_I = \beta eV(\mathbf{r}) + \ln\left(\frac{\Phi_I(\mathbf{r})\lambda_I^3}{\Omega}\right) + \ln n_I. \quad (\text{A22})$$

We multiply the above by $n_I\Phi_I(\mathbf{r})$ and integrate over the volume to obtain the free energy of the ions, F_I ,

$$\begin{aligned} F_I &= -k_B T n_I \ln Q_I/n_I \\ &= \rho_I \int d\mathbf{r} \Phi_I(\mathbf{r}) [eV(\mathbf{r}) + k_B T \ln \Phi_I(\mathbf{r})] \\ &\quad + n_I k_B T \ln\left(\frac{n_I \lambda_I^3}{\Omega}\right). \end{aligned} \quad (\text{A23})$$

We substitute this into Eq. (A20) and again use charge neutrality to obtain

$$\begin{aligned} \frac{\beta F_{scft}}{n_{AB}} &= -\ln(Q_{AB}/n_{AB}) \\ &\quad - \frac{1}{\Omega} \int d\mathbf{r} \chi_{AB} N_{AB} \Phi_A(\mathbf{r}) \Phi_B(\mathbf{r}) \end{aligned} \quad (\text{A24})$$

$$\begin{aligned} & + P_A f N_{AB} \int d\mathbf{r} [\beta eV(\mathbf{r}) \Phi_I(\mathbf{r}) + \Phi_I(\mathbf{r}) \ln \Phi_I(\mathbf{r})] \\ & + n_I \ln\left(\frac{n_I \lambda_I^3}{\Omega}\right), \end{aligned} \quad (\text{A25})$$

where we have set to zero the integral over the volume of $\xi(\mathbf{r})$. This is the expression we seek for the free energy of the system within self-consistent field theory. We shall ignore the last term as it is a constant in the canonical ensemble.

- ¹T. Thurn-Albrecht, J. Schotter, G. Kästle, N. Emley, T. Shibauchi, L. Krusin-Elbaum, K. Guarini, C. Black, M. Tuominen, and T. Russell, *Science* **290**, 2126 (2000).
- ²M. Park, C. Harrison, P. M. Chaikin, R. A. Register, and D. H. Adamson, *Science* **276**, 1401 (1997).
- ³C. Leidel, C. W. Pester, M. Ruppel, V. S. Urban, and A. Böker, *Macromol. Chem. Phys.* **213**, 259 (2012).
- ⁴S. O. Kim, H. H. Solak, M. P. Stoykovich, N. J. Ferrier, J. J. de Pablo, and P. F. Nealey, *Nature* **424**, 411 (2003).
- ⁵M. P. Stoykovich, M. Müller, S. O. Kim, H. H. Solak, E. W. Edwards, J. J. De Pablo, and P. F. Nealey, *Science* **308**, 1442 (2005).
- ⁶S. O. Kim, B. H. Kim, D. Meng, D. O. Shin, C. M. Koo, H. H. Solak, and Q. Wang, *Adv. Mater.* **19**, 3271 (2007).
- ⁷D. O. Shin, B. H. Kim, J.-H. Kang, S.-J. Jeong, S. H. Park, Y.-H. Lee, and S. O. Kim, *Macromolecules* **42**, 1189 (2009).
- ⁸S. Park, D. H. Lee, J. Xu, B. Kim, S. W. Hong, U. Jeong, T. Xu, and T. P. Russell, *Science* **323**, 1030 (2009).
- ⁹D. Sundrani, S. Darling, and S. Sibener, *Nano Lett.* **4**, 273 (2004).
- ¹⁰R. A. Segalman, H. Yokoyama, and E. J. Kramer, *Adv. Mater.* **13**, 1152 (2001).
- ¹¹T. Morkved, M. Lu, A. Urbas, E. Ehrichs, H. Jaeger, P. Mansky, and T. Russell, *Science* **273**, 931 (1996).
- ¹²K. Amundson, E. Helfand, X. Quan, and S. D. Smith, *Macromolecules* **26**, 2698 (1993).
- ¹³Y. Tsori and D. Andelman, *Macromolecules* **35**, 5161 (2002).
- ¹⁴G. G. Putzel, D. Andelman, Y. Tsori, and M. Schick, *J. Chem. Phys.* **132**, 164903 (2010).
- ¹⁵C.-Y. Lin, M. Schick, and D. Andelman, *Macromolecules* **38**, 5766 (2005).
- ¹⁶C.-Y. Lin and M. Schick, *J. Chem. Phys.* **125**, 034902 (2006).
- ¹⁷Q. Tong and S. Sibener, *J. Phys. Chem. C* **118**, 13752 (2014).
- ¹⁸M. Ruppel, C. W. Pester, K. M. Langner, G. J. Sevink, H. G. Schoberth, K. Schmidt, V. S. Urban, J. W. Mays, and A. Boker, *ACS Nano* **7**, 3854 (2013).
- ¹⁹P. Goldberg-Oppenheimer, D. Kabra, S. Vignolini, S. Huttner, M. Sommer, K. Neumann, M. Thelakkat, and U. Steiner, *Chem. Mater.* **25**, 1063 (2013).
- ²⁰S. Elhadj, J. Woody, V. Niu, and R. Saraf, *Appl. Phys. Lett.* **82**, 871 (2003).
- ²¹T. Xu, A. Zvelindovsky, G. Sevink, K. Lyakhova, H. Jinnai, and T. Russell, *Macromolecules* **38**, 10788 (2005).
- ²²Y. Tsori, F. Tournilhac, and L. Leibler, *Macromolecules* **36**, 5873 (2003).
- ²³Y. Tsori, F. Tournilhac, D. Andelman, and L. Leibler, *Phys. Rev. Lett.* **90**, 145504 (2003).
- ²⁴M. Matsen, *Macromolecules* **39**, 5512 (2006).
- ²⁵J.-Y. Wang, T. Xu, J. M. Leiston-Belanger, S. Gupta, and T. P. Russell, *Phys. Rev. Lett.* **96**, 128301 (2006).

- ²⁶P. Kohn, K. Schröter, and T. Thurn-Albrecht, *Phys. Rev. Lett.* **102**, 216101 (2009).
- ²⁷J. Marko and Y. Rabin, *Macromolecules* **25**, 1503 (1992).
- ²⁸R. Kumar and M. Muthukumar, *J. Chem. Phys.* **126**, 214902 (2007).
- ²⁹I. Nakamura, N. Balsara, and Z.-G. Wang, *Phys. Rev. Lett.* **107**, 198301 (2011).
- ³⁰S. Yang, A. Vishnyakov, and A. Neiman, *J. Chem. Phys.* **134**, 054104 (2011).
- ³¹C. Sing, J. W. Zwanikken, and M. O. de la Cruz, *Nat. Mater.* **13**, 694 (2014).
- ³²T. Xu, J. T. Goldbach, J. Leiston-Belanger, and T. P. Russell, *Colloid Polym. Sci.* **282**, 927 (2004).
- ³³M. Matsen, in *Soft Matter Vol 1: Polymer Melts and Mixtures*, edited by G. Gompper and M. Schick (Wiley-VCH, Weinheim, 2006).
- ³⁴F. Schmid, *J. Phys.: Condens. Matter* **10**, 8105 (1998).
- ³⁵A.-C. Shi and J. Noolandi, *Macromol. Theory Simul.* **8**, 214 (1999).
- ³⁶G. H. Fredrickson, V. Ganesan, and F. Drolet, *Macromolecules* **35**, 16 (2002).
- ³⁷G. H. Fredrickson, *The Equilibrium Theory of Inhomogeneous Polymers* (Clarendon, 2006).
- ³⁸M. Turner, *Phys. Rev. Lett.* **69**, 1788 (1992).
- ³⁹M. Matsen, *J. Chem. Phys.* **106**, 7781 (1997).
- ⁴⁰R. Messina, C. Holm, and K. Kremer, *J. Polym. Sci., Part B: Polym. Phys.* **42**, 3557 (2004).

6 | Orienting Block Copolymer Thin Films via Entropy

Authors: Ting-Ya Lo, **Ashkan Dehghan**, Prokopios Georgopoulos, Apostolos Avgeropoulos, An-Chang Shi and Rong-Ming Ho

Contribution: My contribution to this paper was to construct the theoretical model for the multi-arm star block copolymer system and develop the computational method to solve the SCFT equations. I also contributed by writing the theoretical section of the manuscript, which was edited and reviewed by Dr. An-Chang Shi, Ting-Ya Lo and Dr. Rong-Ming Ho.

[Macromolecules. 49, 624 (2016)]

In this study, we examine the effects of entropy on the orientation of polymer domains in block copolymer thin films. Similar to our previous study, the challenge with the use of block copolymers as a viable path for nano-lithography is controlling the orientation of the micro domains (61). The phase behaviour of polymer melts in a thin film geometry is dictated by the polymer-substrate and/or polymer-air interactions. The asymmetry in the interactions between polymer species and the surfaces often results in the formation of micro domains parallel to the air/substrate surfaces. In most applications however, domains ordered perpendicular to the thin film surfaces are desired (62). In this work, we show that the entropic effect can be used as a mechanism to direct the self-assembly of polymer domains in block copolymer thin films.

To investigate the entropic effect, we focus on cylinder and lamellae forming $(AB)_n$ star block copolymers. Here, n corresponds to the number of AB polymers joined together to form the n -arm star block copolymers. As a model system for the experiments, we use Polystyrene-*b*-Poly(dimethylsiloxane), PS-PDMS. The $(PS-PDMS)_n$ star block copolymers are synthesized by joining n PDMS end-groups together. The surface tension γ for the PDMS blocks is much lower than that of PS species. Therefore, it is ener-

getically more favourable for the PDMS species to wet the polymer-air interface. This is confirmed for both lamellae and cylinder forming linear (PS-PDMS)₁ block copolymers using Transmission Electron Microscopy (TEM) and Small Angle X-ray Scattering (SAXS).

The phase behaviour of the 3-arm (PS-PDMS)₃ is investigated using TEM, SAXS and X-ray Photoelectron Spectroscopy (XPS). At the air-polymer interface, we observe a thin wetting layer of PDMS blocks. This is expected and is due to the low surface tension of the PDMS species. The difference in the polymer-substrate interaction between the PDMS and PS species is much smaller, and thus we observe hexagonally packed cylinders formed perpendicular to the polymer-substrate interface. These perpendicularly oriented cylinders propagate through the bulk of the thin film up to the polymer-air interface. At the polymer-air surface however, we observe randomly oriented parallel arrays of cylinders. In contrast to the linear (PS-PDMS)₁ system, which forms parallel arrays of cylinders over the entire range of the thin film, the 3-arm star block copolymers form perpendicular domains except at the polymer-air surface.

We further explore the effects of entropy on the orientation of micro domains by studying lamellae forming (PS-PDMS)_n star block copolymers. Similar to the cylinder forming system, the linear (PS-PDMS)₁ melt forms layers of lamellae parallel to the air and substrate surfaces. For the 3-arm system, our TEM images show a mixture of parallel and perpendicular domains. However, increasing the number of arms to 4, we observe only perpendicular domains. The results for the lamellae and cylinder forming melts support the hypothesis that entropy can be used as a mechanism to reorient domains in block copolymer thin films.

To support the experiments, we construct a self-consistent field theory model for the (PS-PDMS)_n star block copolymer melts, where the PDMS and PS species are modelled as A and B blocks respectively. The polymer-air and polymer-substrate interactions are chosen to qualitatively represent the values measured in the experiments. Similar to the experimental models, we consider cylinder and lamellae forming (AB)_n star block copolymers with n=1, 2, 3 and 4. For each phase, we consider three different morphologies: parallel, perpendicular and mixed. The mixed morphology is composed of perpendicular domains near the polymer-substrate interface and bulk region of the thin film, and parallel domains at the polymer-air surface. The star block copolymers are formed by joining the ends of the A blocks together. The controlling parameter in our study is the magnitude of the relative interaction between the A/B species and the air interface. We define this parameter as $\Delta\chi = \chi_{BAir} - \chi_{AAir}$. To calculate the phase behaviour of the system as a function of $\Delta\chi$,

we compare the free energies of the perpendicular, parallel and mixed phases.

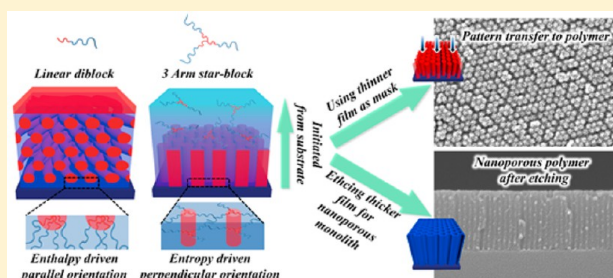
Our calculations show that at small $\Delta\chi$ values, the energetically favourable structure for both cylinder and lamellae forming $(AB)_n$ star block copolymers is the perpendicular phase. As $\Delta\chi$ is increased, we observe a phase transition from the perpendicular to the parallel phase. We note that the critical $\Delta\chi_c$ value at which the thin film undergoes a phase transition from the perpendicular to the parallel phase depends on the $(AB)_n$ architecture. Star block copolymers with larger value for n will transition from the perpendicular to the parallel phase at greater $\Delta\chi_c$ values. This indicates that the entropic penalty for reorienting micro domains from the perpendicular to the parallel alignment is greater for star block copolymers with greater number of arms. Our SCFT results are in qualitative agreement with the experiments and support the hypothesis that the entropy of star block copolymers can be used as a mechanism to orient domains perpendicular to the thin film surfaces.

Orienting Block Copolymer Thin Films via Entropy

Ting-Ya Lo,[†] Ashkan Dehghan,[‡] Prokopios Georgopoulos,^{§,⊥} Apostolos Avgeropoulos,[§] An-Chang Shi,^{*,‡} and Rong-Ming Ho^{*,†}[†]Department of Chemical Engineering, National Tsing Hua University, Hsinchu 30013, Taiwan, R.O.C.[‡]Department of Physics and Astronomy, McMaster University, Hamilton, Ontario L8S 4L8, Canada[§]Department of Materials Science Engineering, University of Ioannina, University Campus, Ioannina 45110, Greece

Supporting Information

ABSTRACT: Controlling the orientation of nanostructured thin films of block copolymers (BCPs) is essential for next-generation lithography using BCPs. According to conventional wisdom, the orientation of BCP thin films is mainly determined by molecular interactions (enthalpy-driven orientation). Here, we show that the entropic effect can be used to control the orientation of BCP thin films. Specifically, we used the architecture of star-block copolymers consisting of polystyrene (PS) and poly(dimethylsiloxane) (PDMS) blocks to regulate the entropic contribution to the self-assembled nanostructures. The study unequivocally demonstrate that for star-block copolymers with the same volume fractions of PS and PDMS, perpendicularly oriented BCP nanostructures could be induced via an entropic effect regulated by the number of arms. Also, the feasibility of using the star-block copolymer thin films for practical applications is demonstrated by using the thin film as a mask for nanolithography or as a template for the fabrication of nanoporous monolith.



INTRODUCTION

In recent decades, block copolymers (BCPs) have been extensively studied due to their ability to self-assemble into various ordered nanostructures with feature size in the 10–100 nm range.^{1,2} Well-defined nanostructures can be tailored by molecular engineering of synthetic BCPs, resulting in promising potentials for various advanced technological applications, in particular next-generation lithography.^{3–6} For many applications, nanostructured thin films with oriented periodic arrays over large areas are desirable. Variations in film thickness,⁷ substrate/polymer interaction,^{8–11} and substrate topography¹² have been exploited to orient and direct the self-assembly of BCP nanostructures. Most engineering applications demand thin films in which the orientation of the structures, such as lamellae or cylinders, is perpendicular to the substrate. Many attempts have been made to obtain perpendicularly oriented BCP nanostructures. While most research to date has focused on controlling the surface by varying chemical properties of the system,^{8–11} less attention has been paid to mechanisms involving intrinsic architectures of BCPs.¹³ For instance, experimental^{14,15} and theoretical¹⁶ evidence indicate that linear ABA triblock copolymers (with relative interfacial energy $\Delta\gamma = \gamma_A - \gamma_B \sim 2$ (mN/m), $\gamma_B < \gamma_A$)¹⁴ are easier than AB diblock copolymers to form nanostructures perpendicular to a substrate. Recently, Kim and co-workers¹⁷ also found that 18-arm poly(methyl methacrylate)-*b*-polystyrene star-block copolymer (with $\Delta\gamma = \gamma_{PS} - \gamma_{PMMA} \sim 3.2$ (mN/m) at 20 °C)¹⁸ will also give an opportunity to form perpendicularly oriented

nanostructure but with low aspect ratio. However, the details of utilizing $(AB)_n$ star-block copolymer to circumvent enthalpic effects for perpendicular nanostructures still remain largely unexplored, and how to achieve the perpendicular orientation with large aspect ratio remains a challenge. Note that the effects of arm numbers and surface energy difference between the constituted block are critical to affect the entropic effect on the orientation of the self-assembled BCP thin film. Furthermore, in order to self-assemble into features smaller than 10 nm, different blocks of the BCP must be highly incompatible or with a very high interaction parameter (χ) that is a fundamental measure of block incompatibility.^{19,20} Orienting such materials is challenging because the blocks generally have disparate polarities. The main barrier for perpendicular orientation is that, in general, any BCP possesses a low surface energy block, which prefers to wet the air free surface (air/polymer interface), and/or a constituted block with preferred interaction to the substrate (polymer/substrate interface) due to the favorable enthalpic interactions. One strategy to overcome the large enthalpic barrier is to use solvent evaporation, which could induce perpendicular orientation of high- χ BCPs due to the gradients of solvent concentration in the swollen polymer film during the drying process.^{21,22} However, the solvent evaporation method usually leads to nonthermal equilibrium

Received: December 11, 2015

Revised: December 23, 2015

Published: January 13, 2016

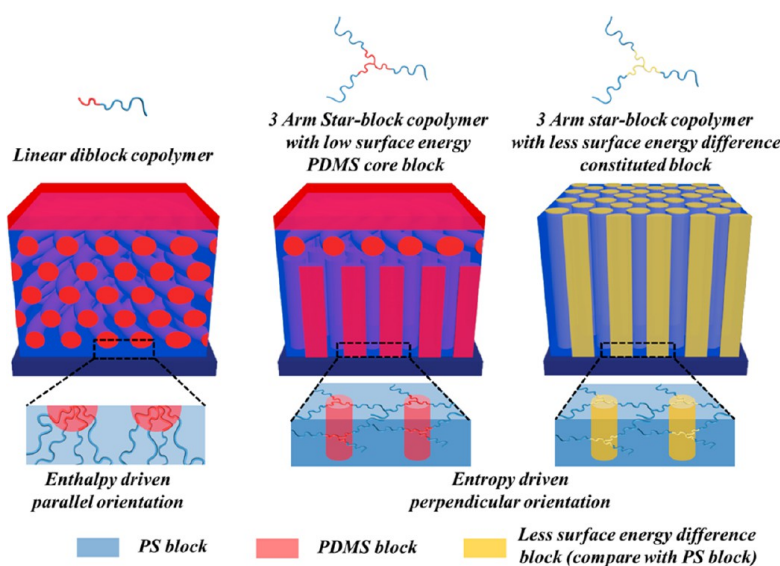


Figure 1. Schematic illustration of entropy-driven orientation of nanostructured thin films using star-block copolymer of the (PS-*b*-PDMS)₃ type and star-block copolymer with less surface energy difference constituted block in comparison to the enthalpy-driven orientation using a simple diblock copolymer (PS-*b*-PDMS).

morphologies, which are less stable against thermal treatment. Consequently, inducing perpendicular orientations of high- χ BCPs by thermal treatment alone would still require control of both interfaces of the film, which is a challenge.

In this study, we explore an approach utilizing BCPs with star-like architecture to regulate entropic contributions of the BCPs at the interfaces. The basic idea is that due to their unique topology, the star architecture of the BCPs provides an extra entropic contribution; as illustrated in Figure 1, this entropic driving force could be strong enough to overcome the selective substrate/polymer interactions, leading to spontaneous formation of perpendicularly oriented BCP nanostructures. As a model system, a series of polystyrene-*b*-poly(dimethylsiloxane) (PS-*b*-PDMS) (a BCP system with a very large χ) and corresponding *n*-arm star-block copolymers (each molecule is formed by joining *n* diblocks together with their PDMS ends) are used to demonstrate the feasibility of the entropy-driven method. Our experimental results demonstrate that the star architecture of the BCPs indeed leads to perpendicularly oriented nanostructures initiated from the substrate. The resulting block copolymer thin films are composed of predominately perpendicularly oriented cylinders or lamellae with, in some cases, a few layers of parallel nanostructures at the BCP/air interface due to the extremely low surface energy of the PDMS, as illustrated in Figure 1. Also, the SCFT simulation was carried out to further investigate the 3D morphologies of the thin films and corresponding metastability with respect to the entropy-driven orientation of the microdomain. The theoretical results indicate that the entropic penalty for reorienting the *n*-armed star-block copolymers to parallel morphologies is larger for BCPs with larger number of arms.

EXPERIMENTAL SECTION

Materials Synthesis. The synthesis of the PS-*b*-PDMS samples was accomplished by sequential anionic polymerization of styrene (Acros Organics, 99%) and hexamethylcyclotrisiloxane (D₃, Acros Organics, 98%), employing high-vacuum techniques as described elsewhere.^{29–31} Styrene was purified by distillation from CaH₂ to

dibutylmagnesium (Sigma-Aldrich, 1 M solution in heptane) and then stored into precalibrated ampules. Hexamethylcyclotrisiloxane (D₃) was inserted in a round-bottom flask, diluted by an equal volume of purified benzene, and stirred over CaH₂. The solution (D₃ and C₆H₆) was transferred into a flask containing polystyryllithium (PS⁽⁻⁾Li⁽⁺⁾) through a short path distillation apparatus, by distillation of the solvent and sublimation of the D₃, where it was stirred in the presence of PS⁽⁻⁾Li⁽⁺⁾ for approximately 2 h at room temperature followed by sublimation and storage at precalibrated ampules. The solvents used for the polymerization were benzene (Riedel de Haen, 99.7%) and tetrahydrofuran (THF, Fisher Scientific, 99.99%). Benzene was purified via distillation from CaH₂ and then stored under vacuum in the presence of PS⁽⁻⁾Li⁽⁺⁾. Tetrahydrofuran was refluxed through metallic sodium and then distilled through CaH₂ and Na/K alloy (3:1) under high-vacuum techniques and was stored under vacuum in calibrated ampules. The initiator used was *sec*-butyllithium (*sec*-BuLi, Sigma-Aldrich, 1.4 M in cyclohexane) after dilution in purified benzene until the wanted concentration was achieved. The termination reagent chosen was trimethylchlorosilane (ClSi(CH₃)₃, Sigma-Aldrich, 99+%) which was distilled from CaH₂ and then stored in ampules. For the synthesis of the star-block copolymers purification of the linking agents trichloromethylsilane (CH₃SiCl₃) (Aldrich, 99+%) and tetrachlorosilane (SiCl₄) (Aldrich, 99+%) was accomplished through distillation from CaH₂ and stored under high vacuum after several freeze-drying cycles. Methanol (Fluka, 99%) was used as the precipitating media of all polymers and also for the termination of the sample aliquots received from the polymerization solution for molecular weight control. Methanol was used without any further purification for the precipitation but with a small quantity of antioxidant 2,6-di-*tert*-butyl-*p*-cresol (Aldrich, 99+%). The sample nomenclature is S_{*x*}-*b*-D_{*y*}, where *x* and *y* notations correspond to the average per number molecular weight \bar{M}_n values of each segment (in kg/mol). In case of the star-block copolymers, the nomenclature is (S_{*x*}-*b*-D_{*y*})_{*n*}, at which *n* corresponds to the number of diblock copolymer chains and is equal to 3 and 4 in the present study.

After the synthesis of the PS-*b*-PDMS⁽⁻⁾Li⁽⁺⁾, to synthesize the whole series of the star-block copolymers ((S_{*x*}-*b*-D_{*y*})₃ and (S_{*x*}-*b*-D_{*y*})₄), the mixture was separated into two different glass apparatuses, and with the use of two different types of chlorosilane coupling agents, trichloromethylsilane (CH₃SiCl₃) and tetrachlorosilane (SiCl₄), the desired star block copolymers were synthesized. It is important to mention that during the synthetic procedure the \bar{M}_n value was checked via small aliquots taken from the reaction solution. It should be

Table 1. Molecular and Structural Characterization of the Linear and Star-Block Copolymers Synthesized

sample code	diblock				star-block				bulk state morphology
	\bar{M}_n^{PS} (kg/mol)	\bar{M}_n^{PDMS} (kg/mol)	D_M	f_{PDMS}^v	\bar{M}_n^{PS} (kg/mol)	\bar{M}_n^{PDMS} (kg/mol)	D_M	n	
(S _{13.7} -b-D _{7.1}) ₁	13.7	7.1	1.03	0.36				1	cylinder
(S _{13.7} -b-D _{7.1}) ₃	13.7	7.1	1.03	0.36	41.1	21.3	1.07	3	cylinder
(S _{9.3} -b-D _{10.1}) ₁	9.3	10.1	1.05	0.54				1	lamellae
(S _{9.3} -b-D _{10.1}) ₃	9.3	10.1	1.05	0.54	27.8	30.3	1.08	3	lamellae
(S _{9.3} -b-D _{10.1}) ₄	9.3	10.1	1.05	0.54	37.0	40.4	1.09	4	lamellae

mentioned that each star-block copolymer series (PS-*b*-PDMS)_{*n*} have the same block copolymer precursor (PS-*b*-PDMS), and also scientific glass blowing was performed in order to create a specific glass reactor. The molecular characterization was carried out by using gel permeation chromatography (GPC) and proton nuclear magnetic resonance (¹H NMR) spectroscopy. The data are given in Table 1.

Sample Preparation. Bulk samples of the PS-*b*-PDMS and star-block copolymers were prepared by the solution-casting method using cyclohexane as solvent at room temperature. After 1 week for sample drying, bulk samples can be obtained. The bulk samples were further dried in vacuum oven for 3 days at 120 °C to remove residual solvent. Subsequently, the bulk samples were thermally treated at 180 °C for 12 h and then rapidly cooled to ambient condition for TEM and SAXS experiments. To examine the architecture effect on the thin-film phase behaviors, a series of BCP thin films with different thickness were prepared from spin coating, followed by thermal annealing. Thin films with thickness of 60, 120, 200, and 350 nm were thermally annealed at 280 °C for 30 min followed by quenching using liquid nitrogen. For morphological identification, the thermally annealed thin-film samples were directly examined by SPM (SPA-400) and GISAXS (beamline BL23A in the National Synchrotron Radiation Research Center (NSRRC), Taiwan) experiments. For TEM observation, thin-film samples were stripped from the functionalized SiO₂ substrate using 1% HF solution for 30 s, then floated onto the surface of water, and finally collected with copper grids. To further examine the surface morphology under the PDMS thin layer, the air surfaces of the samples were treated with CF₄ reactive ion etching (RIE) to remove this thin layer. After CF₄ RIE, the thin-film samples were then further treated with O₂ RIE, giving the required height contrast for FE-SEM (JSM-7401F) observation. Cross-sectional TEM images were also obtained from samples with cutting plane normal to the film by FEI Helios Nanolab 400 dual beam focused ion beam (FIB). The effects of block copolymer architecture on the orientation of lamellae- and cylinder-forming BCPs were investigated using self-consistent field theory (SCFT) calculations.^{32–34}

Instrumentation Details. Ultrathin microsections (50–60 nm) of solution-cast PS-*b*-PDMS and star-block copolymer bulk samples were obtained by ultracryomicrotomy at –160 °C using a Reichert Ultracut microtome. Bright field TEM images were obtained from the microtoming and thin-film samples without staining due to the significant mass–thickness contrast from the strong scattering of the silicon-containing microdomains. Transmission electron microscopy (TEM) experiments were performed on a (JEOL-2100) TEM instrument operating at an accelerating voltage of 200 kV. Field emission scanning electron microscopy (FE-SEM) observations were performed on a JEOL JSM-7401F using accelerating voltages of 5 keV. The samples were mounted to brass shims using carbon adhesive and then sputter-coated with 2–3 nm of platinum. Tapping-mode SPM images of thin-film samples were also obtained. A Seiko SPA-400 AFM with a Seiko SPI-3800N probe station was utilized at room temperature. A silicon tip was used in dynamic force mode experiments with a spring force of 5 N/m and a scan rate of 1 Hz. The GISAXS experiments were conducted at beamline BL23A in the National Synchrotron Radiation Research Center (NSRRC), Taiwan. A monochromatic beam with $\lambda = 1.033$ Å was used, and the incident angle was 0.12. Scattering intensity profiles were determined for the scattering intensity (*I*) versus the scattering vector (*q*), where $q = (4\pi/\lambda) \sin(\theta/2)$ and θ is the scattering angle. The oxygen reactive ion etching (RIE) treatment for oxidation was carried out by a RF-power

of 100 W at the pressure of 75 mTorr for 20 s. The CF₄ RIE for etching PDMS was generated by RF power of 50 W for 40 s at which the involving gas of CF₄ and O₂ was in a ratio of 2:1 and the pressure was 150 mTorr. The cross-section thin-film sample was sliced by a FEI Helios Nanolab 400 dual beam focused ion beam (FIB). Before FIB cutting, a protection layer (~200 nm) was deposited, and low accelerating voltage (5 keV) was used to reduce milling damage. With appropriate sectioning conditions, the problems of the deformation and damage to soft material can be significantly alleviated. A cross-section (20 μm wide by 5 μm tall by ~60 nm thick) sample was cut and attached to an Omniprobe copper liftout grid for TEM imaging. XPS measurements were made using a Thermo VG-Scientific Sigma Probe spectrometer that was equipped with a hemispherical electron analyzer. The operating conditions for XPS were as follows: Mg Kα anode, 15 kV, 7.2 mA; incident angle, 45°; angle of collection, 45°; analysis diameter, 400 μm.

RESULTS AND DISCUSSION

Silicon-containing BCPs are most attractive for soft lithography due to their small feature dimension and high etching contrast. However, the silicon-containing BCPs are also notoriously known to be difficult to orient their nanostructures normal to the thin film substrate. The surface tension of PDMS ($\gamma_{\text{PDMS}} = 19.9$ mN/m at room temperature) is significantly lower than that of PS ($\gamma_{\text{PS}} = 40.7$ mN/m at room temperature).^{23,24} Owing to this large enthalpic contribution, neither perpendicular cylinders nor lamellae have ever been reported for thin films of silicon-containing linear diblock copolymers as thermal equilibrium states. In this study, a series of PS-*b*-PDMS diblock copolymers and their corresponding *n*-armed counterparts, star-block copolymers of the (PS-*b*-PDMS)_{*n*} type (each molecule is formed by joining *n* diblocks together with their PDMS ends), are used as model systems to examine the architecture effect on the orientation of the nanostructured thin films of BCPs. Table 1 details the sample codes and characteristics of the linear diblock and *n*-armed star-block copolymers used in this study. A brief description of the synthesis is given in the Experimental Section. The nomenclature used to describe the samples is (S_{*x*}-*b*-D_{*y*})_{*n*} in which the subscripts “*x*” and “*y*” are the molecular weights of each block (in units of kg mol^{–1}), and the subscript “*n*” represents the number of arms. Each molecule is formed by joining *n* diblocks together through their PDMS living ends and specific chlorosilane reagents (trichloromethylsilane or tetrachlorosilane for the samples of the (PS-*b*-PDMS)₃ or (PS-*b*-PDMS)₄ types, respectively).

Figure 2A,C shows TEM images of the (S_{13.7}-*b*-D_{7.1})₁ and (S_{13.7}-*b*-D_{7.1})₃ bulk samples without staining because the intrinsic difference in electron density of the PS and PDMS blocks provides adequate bright field contrast. Both TEM images can be identified as hexagonally packed cylinders of PDMS in the PS matrix. The corresponding one-dimensional (1D) SAXS profiles (Figure 2B,D) further confirm the cylinder phase. The domain spacing (*d*) of the periodic structure is

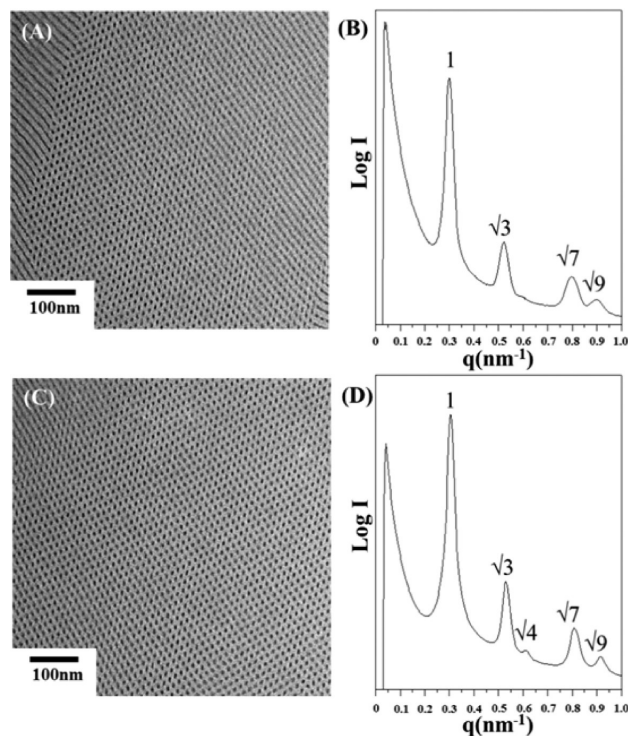


Figure 2. Bulk state TEM micrographs and corresponding 1D SAXS profiles of linear diblock copolymer $(S_{13.7}\text{-}b\text{-}D_{7.11})_1$ (A, B) and three-arm star-block copolymer $(S_{13.7}\text{-}b\text{-}D_{7.11})_3$ (C, D).

estimated as 21.0 and 20.6 nm from the position of the primary scattering peak (according to the relationship $q = 2\pi/d$) for the $(S_{13.7}\text{-}b\text{-}D_{7.11})_1$ and $(S_{13.7}\text{-}b\text{-}D_{7.11})_3$, respectively. In contrast to

diblock copolymers, the star-shape architecture may slightly change the phase boundaries of the BCP phase diagram.^{25,26} However, the volume fractions of all the samples used in this study ($f_{\text{PDMS}}^v = 0.36$ and 0.54) are located away from the boundary of two phases in the phase diagram. Accordingly, the architecture of the copolymers from linear to star will not significantly alter the phase behavior of the two samples in the bulk state in this study. To examine the effect of BCP architecture on thin-film phase behavior, a series of BCP thin films with different thicknesses were prepared by spin coating, followed by thermal annealing. Figure 3A–C shows the TEM images for the $(S_{13.7}\text{-}b\text{-}D_{7.11})_1$ thin films with thickness of approximately 120, 200, and 340 nm, respectively. The samples were annealed at 280 °C for 30 min, followed by quenching using liquid nitrogen. After thermal annealing, all of the TEM images exhibit the characteristic alternating black and white stripe-like texture, suggesting that a parallel cylinder phase is formed, as expected due to the strong enthalpic interaction at the interface. In comparison, thin films of the three-armed star-block copolymer $(S_{13.7}\text{-}b\text{-}D_{7.11})_3$ prepared under the same conditions (identical thickness and annealing temperature) exhibit significant changes of thin-film phase behavior due to the architecture effect. As shown in Figure 3D–F, hexagonally packed dark-dot pattern is observed, indicating that the cylinder axis is normal to the thin film. The morphologies near the interface might be strongly affected by the effect of interfacial interactions, but their details cannot be resolved by TEM projections. To examine the detailed morphology at both interfaces, thermally annealed $(S_{13.7}\text{-}b\text{-}D_{7.11})_3$ thin films with a thickness of 340 nm were used as a representative and examined by scanning probe microscopy (SPM). No obvious morphological features could be identified from the top-view SPM image, whereas the bottom-view SPM image shows hexagonally packed arrays (Figure 4), suggesting that there is a

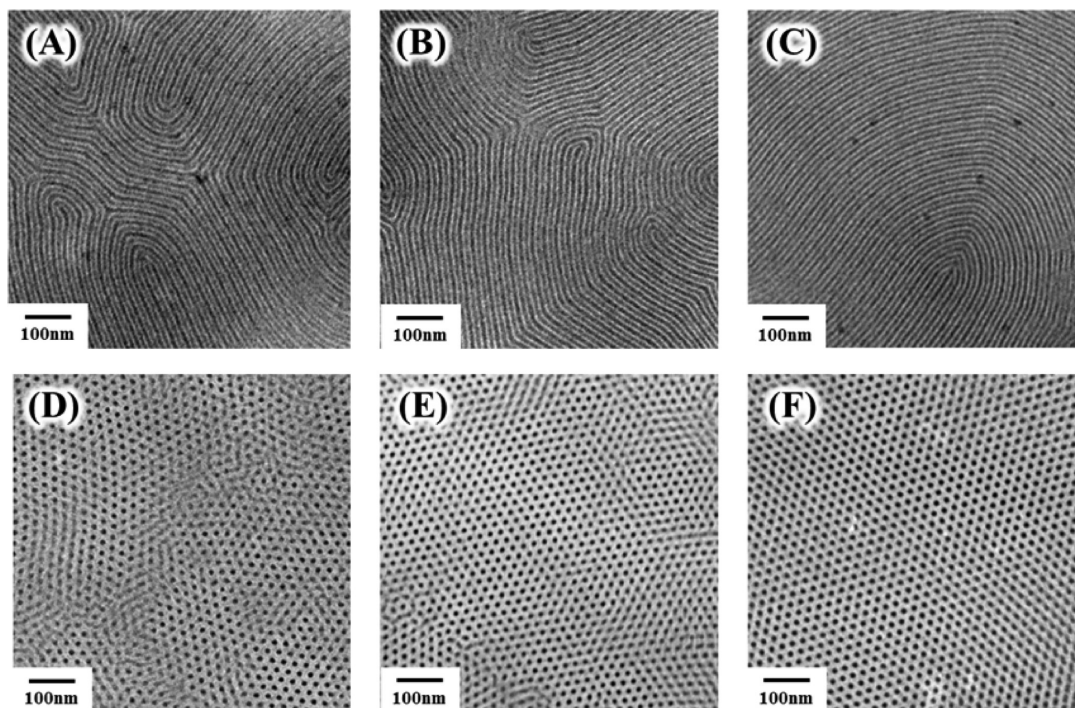


Figure 3. TEM images for the $(S_{13.7}\text{-}b\text{-}D_{7.11})_1$ (A, B, C) and $(S_{13.7}\text{-}b\text{-}D_{7.11})_3$ (D, E, F) thin films after thermal annealing at 280 °C for 30 min followed by quenching using liquid nitrogen with thicknesses of 120 (A, D), 200 (B, E), and 340 nm (C, F), respectively.

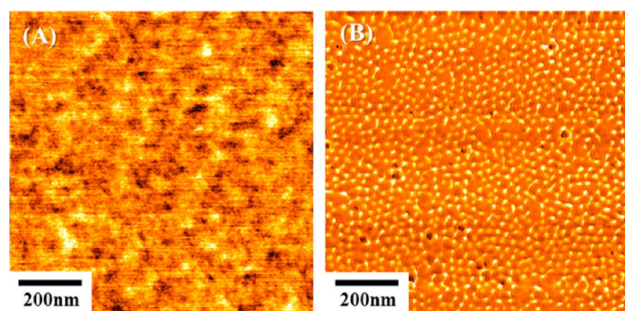


Figure 4. Tapping mode SPM (A) top-view and (B) bottom-view phase images of $(S_{13.7-b-D_{7.11}})_3$ thin film after thermal annealing at 280 °C for 30 min with a thicknesses of 340 nm.

thin-layer of PDMS at the air surface due to its low surface energy. The presence of a thin layer of PDMS at the air/polymer interface was further confirmed by X-ray photoelectron spectroscopy (XPS) experiments. Figure 5 shows a

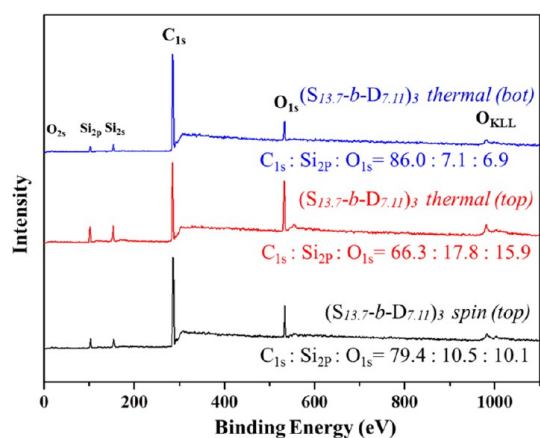


Figure 5. XPS survey spectra of $(S_{13.7-b-D_{7.11}})_3$ thin film top surface before (black) and after (red) thermal annealing; bottom surface after thermal annealing (blue).

survey scan spectrum of the top and bottom surfaces of the thin-film sample. In addition to the carbon (285 eV) signal, the oxygen (533 eV) and Si 2p (103.4 eV) peaks are attributed to the PDMS block. To characterize the proportion of PDMS block for each surface, the atomic composition ratio was calculated from the XPS results. Based on the XPS results, the surface composition of the PDMS block at the top surface before thermal annealing is approximately 47%. However, the composition of the PDMS block is increasing to 74% after thermal annealing. The increasing of the PDMS proportion at the top surface is attributed to a thin-layer of PDMS segregate at the air surface after thermal annealing due to its low surface energy. The time-evolution top-view SPM images further confirms the formation of a thin-layer of PDMS segregate at the air surface after thermal annealing (Figure S1). By contrast, the surface composition of the PDMS block at the bottom surface after thermal annealing is approximately 33%, which is really closed to the intrinsic composition of the PDMS block for the $(S_{13.7-b-D_{7.11}})_3$ sample. This XPS result further confirms the formation of perpendicular cylinders from the substrate without any wetting layer. To further examine the surface morphology underneath the thin PDMS layer, CF_4 reactive ion etching (RIE) was used to remove the PDMS layer. After CF_4 RIE, the

samples were further treated with O_2 RIE,²⁷ giving the required height contrast for FE-SEM observations. As illustrated in Figure 6A, an interesting result can be found for the case of the $(S_{13.7-b-D_{7.11}})_3$ thin film. A randomly oriented stripe morphology can be observed from the top view, suggesting the formation of parallel cylinders. To examine the bottom-view morphology, the thin-film sample was stripped from the SiO_2 substrate using 1% HF solution for 30 s and then floated on the surface of water. The floated thin-film sample was then collected on the reverse side using another clean Si wafer for morphological observations.²⁸ In contrast to the top-view image, the bottom-view FE-SEM image (Figure 6B) exhibits a hexagonal packed cylinder morphology with perpendicular orientation as verified by XPS results (Figure 5). These results confirm the formation of perpendicular cylinders initiated from the substrate without substrate modification. Cross-sectional TEM images (Figure 6C), obtained by cutting in the plane normal to the film, reveal that perpendicular cylinders indeed extend from the substrate, with one or two layers of parallel cylinders at the air/polymer interface. The stability of the forming mixed morphology was examined by flipping the annealed film sample over and then thermal annealing again. As shown in Figure S2, the parallel cylinders will be formed at the free surface (bottom side for the first round) whereas perpendicular cylinders can be formed at the wafer substrate (top side for the first round). These results further confirm that the polymer chains at the annealing temperature (280 °C) have sufficient mobility for the rearrangement of the forming morphologies.

The long-range orientation order of the nanostructured thin films was investigated using grazing incidence SAXS (GISAXS). For the 340 nm $(S_{13.7-b-D_{7.11}})_1$ film without thermal annealing treatment, a clear diffraction ring can be observed, indicating a structure with randomly oriented cylinders (Figure S3A). After thermal annealing at 280 °C for 30 min, the GISAXS pattern of the $(S_{13.7-b-D_{7.11}})_1$ thin film contains many diffraction spots without any semicircular lines. Those diffraction spots indicate that the cylinders are oriented parallel to the substrate (Figure 6D). Taking into account the diffraction peaks due to the presence of the two X-ray beams, i.e., the transmitted and reflected beams, the q_y^{R1} , q_y^{R2} , and q_y^{R3} spots can be assigned as the diffraction peaks of the {10}, {11}, and {20} planes, respectively, attributed to the reflected X-ray beam. In contrast, the q_y^{T1} , q_y^{T2} , and q_y^{T3} spots can be assigned as the diffraction peak of the {10}, {11}, and {20} planes, respectively, resulting from the transmitted X-ray beam. Similarly, for the 340 nm $(S_{13.7-b-D_{7.11}})_3$ film without thermal annealing, a clear diffraction ring is observed (Figure S4A). Unlike the results from the $(S_{13.7-b-D_{7.11}})_1$ thin film, the in-plane diffraction pattern (constant q_z) of the $(S_{13.7-b-D_{7.11}})_3$ thin film shows the out-of-plane intensity along q_z after thermal annealing at 280 °C for 30 min due to the form factor of the perpendicular cylinder (Figure 6E). The diffraction peaks are calculated at the relative q_y values of $1:\sqrt{3}:\sqrt{4}:\sqrt{7}:\sqrt{9}$, at which the q_y scans were extracted for $q_z = 0.55 \text{ nm}^{-1}$ (Figure S4D). In agreement with the cross-sectional TEM results, a weak peak can be observed near $q_y^{par} = 0.252 \text{ nm}^{-1}$ as well as a sharp peak at $q_y^{per} = 0.303 \text{ nm}^{-1}$, demonstrating eventually the formation of PDMS parallel cylinders. The cylinders in the parallel and perpendicular directions show that the relative q value of $q_y^{par}:q_y^{per} = 1:2/\sqrt{3}$.¹⁴ The first peak for the perpendicular orientation, i.e., q_y^{per} , occurs at 0.303 nm^{-1} , corresponding to a (10) plane spacing of 20.7 nm. This value is in good agreement

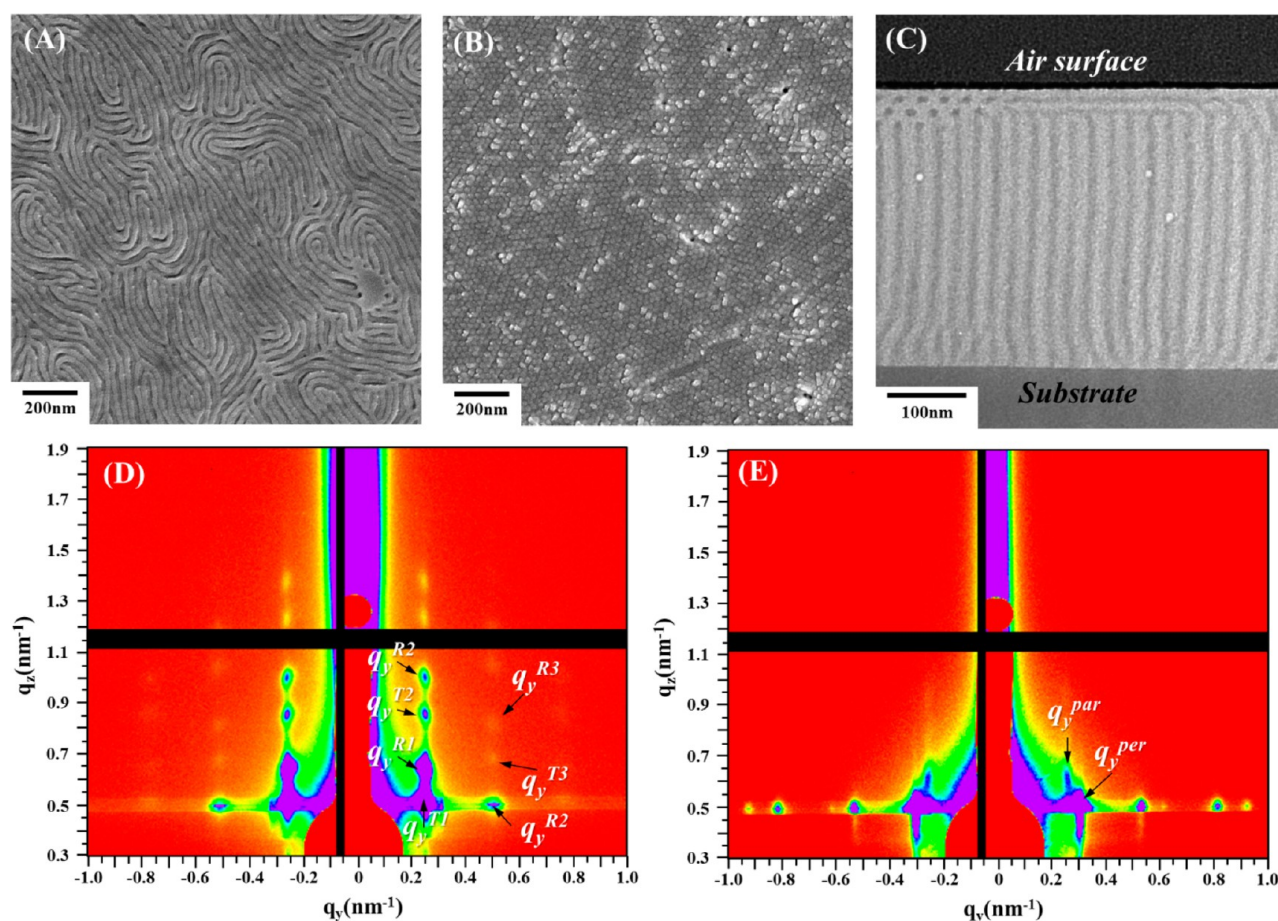


Figure 6. 340 nm thick $(S_{13,7}\text{-}b\text{-}D_{7,1})_3$ films after thermal annealing at 280 °C for 30 min. (A) Top-view and (B) bottom-view FE-SEM image of the thin film sample after RIE treatment. (C) Cross-sectional TEM image. 2D GISAXS pattern of (D) $(S_{13,7}\text{-}b\text{-}D_{7,1})_1$ and (E) $(S_{13,7}\text{-}b\text{-}D_{7,1})_3$ thin-film samples with thickness of 340 nm after thermal annealing at 280 °C for 30 min.

with the SAXS data from the bulk sample ($d_{\text{bulk}} \sim 20.6$ nm). To further demonstrate the mechanism of entropy-driven orientation, another set of PS-*b*-PDMS samples (diblock copolymer $(S_{9,3}\text{-}b\text{-}D_{10,1})_1$, three-arm star-block copolymer $(S_{9,3}\text{-}b\text{-}D_{10,1})_3$ and four-arm star-block copolymer $(S_{9,3}\text{-}b\text{-}D_{10,1})_4$) were examined using similar experimental approaches. From the TEM and SAXS results (Figure 7), all three samples exhibit lamellar morphologies in the bulk state. It should be noted that the samples were prepared under the same conditions as the samples of the $(S_{13,7}\text{-}b\text{-}D_{7,1})_n$ with $n = 1, 3$. After thermal annealing, the linear diblock sample $(S_{9,3}\text{-}b\text{-}D_{10,1})_1$ shows a parallel lamellar structure, as evidenced from the TEM results (Figure 8A). By increasing the number of arms for the BCP sample, the TEM image of the three-armed star-block copolymer $(S_{9,3}\text{-}b\text{-}D_{10,1})_3$ exhibits coexistence of parallel and perpendicular lamellar patterns (Figure 8B). As the number of arms increases to four, the TEM image of the shows an alternating black and white stripe-like texture, indicating that the lamellar sheet is perpendicular to the substrate (Figure 8C). The corresponding GISAXS pattern (Figure 8D–F) confirms the long-range orientation of the lamellar structured thin films. Similar to the results of cylinder structured thin films, cross-sectional TEM image of the four-armed star-block copolymer $(S_{9,3}\text{-}b\text{-}D_{10,1})_4$ thin film reveals that perpendicular lamellar structure is initiated from substrate and extended for hundreds of nanometers, but a few layers of parallel lamellae at the air/

polymer interface are still formed due to the low surface energy of the PDMS (Figure 9).

The different behavior of the nanostructured thin films composed of linear diblock copolymer and star-block copolymer could be understood by comparing the free energy of the thin films with different orientation of the nanostructures. In general, thin films of lamellae- or cylinder-forming BCPs would prefer a parallel orientation in which the microdomains are parallel to the substrate, thus maximizing the favorable substrate–polymer interaction. For a linear diblock copolymer, perpendicular cylinders or lamellae could be formed only if the substrate–block interactions, or the interfacial energies of the constituted blocks, are closely matched. On the other hand, in the case of the star-block copolymers, a perpendicular orientation of the nanostructured thin films can be obtained even for BCPs, such as PS-*b*-PDMS, having a relative large difference in the interfacial energies. This unexpected phenomenon can be understood by considering the topology of the linear block and star-block copolymers. It is noted that in contrast to the middle block, the end block possesses high tendency to allocate at the air surface or the interface due to entropy consideration. For a star-block copolymer, wetting of the low surface energy middle block to the air surface or the substrate is thermodynamically favored due to the enthalpy consideration that will reduce the tendency of the end block allocation at the air surface, giving the parallel

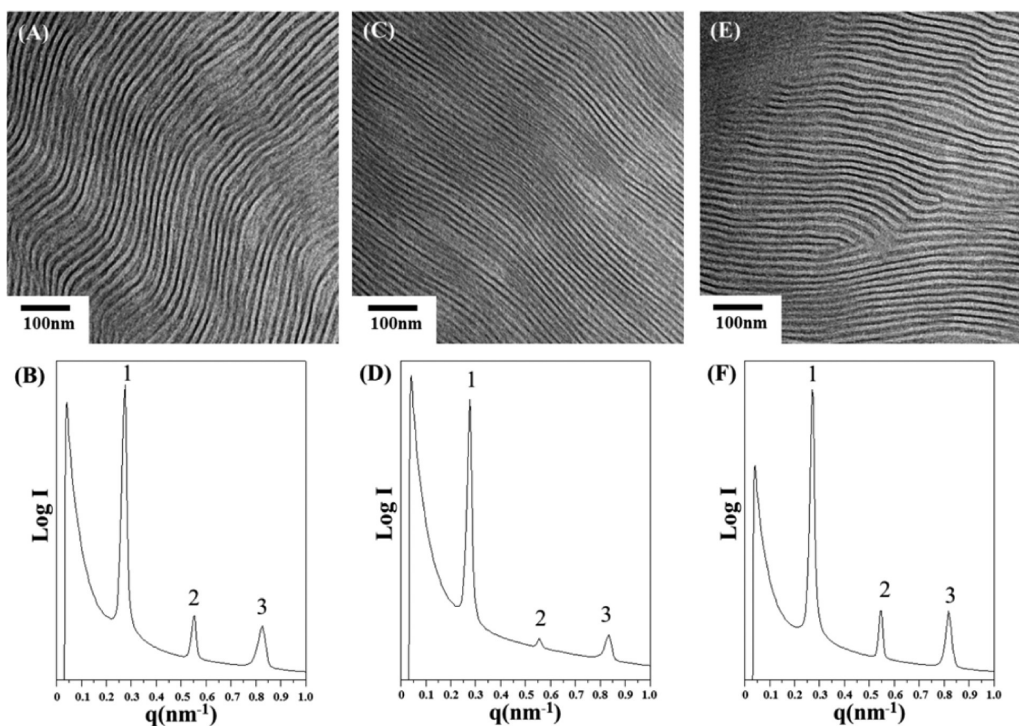


Figure 7. Bulk state TEM micrographs and corresponding 1D SAXS profiles of linear diblock copolymer ($S_{9,3}\text{-}b\text{-}D_{10,1}$)₁ (A, B), three-arm star-block copolymer ($S_{9,3}\text{-}b\text{-}D_{10,1}$)₃ (C, D), and four-arm star-block copolymer ($S_{9,3}\text{-}b\text{-}D_{10,1}$)₄ (E, F).

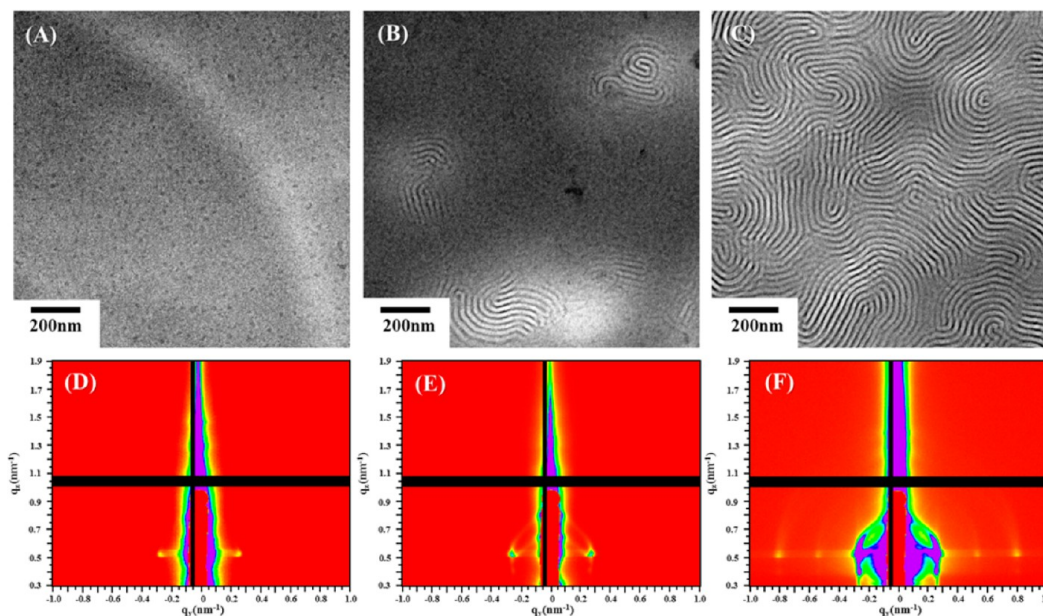


Figure 8. TEM images and corresponding 2D GISAXS pattern of for the ($S_{9,3}\text{-}b\text{-}D_{10,1}$)₁ (A, D), ($S_{9,3}\text{-}b\text{-}D_{10,1}$)₃ (B, E), and ($S_{9,3}\text{-}b\text{-}D_{10,1}$)₄ (C, F) thin films after thermal annealing at 280 °C for 3 h with a thicknesses of 340 nm.

orientation of the cylinders and lamellae as observed (Figure 1). In contrast to a linear block copolymer, a star-block copolymer possesses higher number of chain ends that will cause the higher entropic penalty in the parallel orientation. As a result, with the increase in the arm number, it is possible to give the perpendicular orientation at which the wetting tendency of low surface middle block can be overcome by the annihilation of entropy penalty. Our experiments on the PS-*b*-PDMS system clearly demonstrate that the entropic effect due to the star

architecture can be strong enough to overcome the enthalpic interactions at the interface, in particular from the substrate, resulting in the spontaneous formation of perpendicularly oriented lamellae or cylinders. It is noticed that the cross-sectional TEM results show that the air free surface is composed of one or two layers parallel cylinders. This surface layer is presumably due to the very low surface energy of the PDMS block. The interfacial energy of PS or PDMS for the substrate upon thermal annealing at 280 °C was estimated

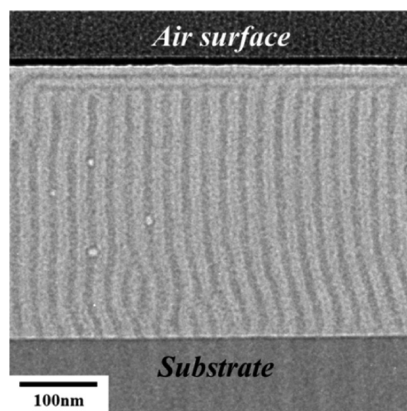


Figure 9. Cross-sectional TEM image of 340 nm thick $(S_{9.3}\text{-}b\text{-}D_{10.1})_4$ films after thermal annealing at 280 °C for 3 h.

using the equation $\gamma_{12} = \gamma_1 + \gamma_2 - W_{12}$, where γ_1 is the surface tension of PS or PDMS, γ_2 is the surface tension of the SiO_2 substrate, and W_{12} is the work of adhesion of PS or PDMS with the SiO_2 substrate. The resulting interfacial energy difference between PS and PDMS for the SiO_2 substrate ($\gamma_{\text{PDMA-sub}}^{280^\circ\text{C}} - \gamma_{\text{PS-sub}}^{280^\circ\text{C}} = 3.6 \text{ mN/m}$) is much smaller than the interfacial energy difference for the air surface ($\gamma_{\text{PS-air}}^{280^\circ\text{C}} - \gamma_{\text{PDMA-air}}^{280^\circ\text{C}} = 7.7 \text{ mN/m}$), indicating that the PDMS has a high affinity to the air surface (see Supporting Information for details). Summarizing our experiments on the cylinder- and lamellae-forming PS–PDMS block copolymers, we can conclude that the entropic effect due to topology of the star copolymers could be strong enough to suppress the enthalpic interactions, resulting in perpendicularly oriented nanostructured thin films initiated from the substrate. Furthermore, self-consistent field theory (SCFT) simulations were also performed in order to understand the orientation changes of the microdomains with different arm numbers. On the basis of the SCFT calculation, the qualitative predictions indicate that a perpendicular morphology at small $\Delta\chi N$ and a parallel morphology at large $\Delta\chi N$ while the crossover between the two occurs at increasing $\Delta\chi N$ with increasing arm number. Accordingly, the SCFT calculation shows that the transition from the perpendicular to the parallel phase occurs at larger interfacial energy differences for copolymers with greater number of arms. The theoretical studies of the corresponding block copolymer systems provide further understanding of the entropy-driven orienting effect via varying the number of arms of the star (see Supporting Information for details).

For practical applications, especially for the use of BCP thin film as a mask for nanolithography, it is necessary to acquire nanostructures with high aspect ratio (specifically, perpendicular cylinders and lamellae) throughout the entire film thickness with long-range ordering. Note that the formation of a few layers of parallel microdomains from the self-assembly of PS–PDMS with thermal equilibrium morphologies is inevitable due to the extremely low surface energy of the PDMS. As successfully demonstrated by Ross and co-workers,²¹ the high-aspect-ratio nanostructures could be obtained by removing the parallel microdomains at the air/polymer interface through a high power CF_4/O_2 RIE treatment followed by O_2 RIE treatment at which both PS and PDMS could be simultaneously degraded under appropriate conditions first, and then the PDMS will be oxidized by the RIE treatment in a continuous process. To examine the feasibility of using the star-block copolymer thin films for pattern transfer, the $(S_{13.7}\text{-}b\text{-}D_{7.1})_3$

sample was spin coated on a SiO_2 substrate and then thermally annealed at 280 °C for 30 min, followed by quenching using liquid nitrogen. The thermal annealed $(S_{13.7}\text{-}b\text{-}D_{7.1})_3$ thin film was stripped from the SiO_2 substrate using 1% HF solution for 30 s and transferred to a PS homopolymer substrate. To demonstrate the feasibility of pattern transfer, a thinner sample (approximately 120 nm) of the perpendicular aligned cylinder structure was prepared. With the high power CF_4/O_2 RIE treatment to remove the parallel oriented nanostructures on the top surface followed by O_2 RIE treatment to remove the PS matrix and simultaneously convert the PDMS to SiO_x for subsequently transferring of nanopattern to the underlying PS substrate, well-ordered perpendicular PS cylinders with hexagonal arrays can be successfully obtained as shown in Figure 10A,B. Furthermore, it is feasible to use the

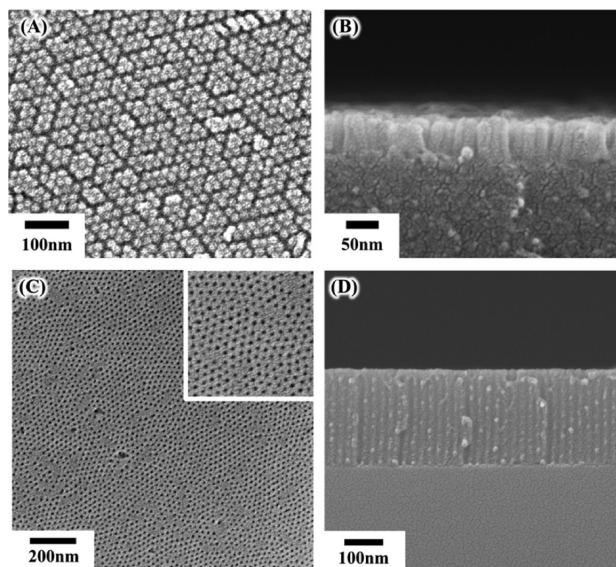


Figure 10. (A) Top-view and (B) cross-sectional SEM images of the perpendicular PS cylinders with hexagonal arrays fabricated by using the SiO_x as a mask for pattern transfer. (C) Top-view and (D) cross-sectional SEM images of nanoporous PS monolith fabricated from a two-step etching process.

thermally annealed $(S_{13.7}\text{-}b\text{-}D_{7.1})_3$ thin films with thicker thickness for the fabrication of nanoporous monolith. The thermally annealed film sample with thickness of 340 nm was first treated with a high power CF_4/O_2 RIE to remove the parallel layers on the top surface, followed by etching away the PDMS cylinders with the 1% HF aqueous solution for 1 h to acquire the perpendicular nanochannels. As shown in Figure 10C,D, well-ordered hexagonally packed cylinder nanochannels (with aspect ratio of approximately 30) can be formed; the fabricated nanoporous monolith can be used as a membrane for further applications. The resultant PS cylinders with hexagonal arrays and the formation of nanoporous PS with well-ordered hexagonally packed nanochannels demonstrate the feasibility to exploit the self-assembled star-block copolymers for pattern transfer and membrane applications.

CONCLUSIONS

In summary, a novel entropy-based mechanism to direct the orientation of cylinder or lamellar morphologies in BCP thin films was demonstrated. Specifically, it was shown that

spontaneous perpendicular alignment of cylinder and lamellar structures can be obtained by simply increasing the number of arms of the star-block copolymers composed of n diblock copolymer chains. The entropic effect due to the topology of the star copolymers can be strong enough to induce perpendicular morphologies of BCPs, as demonstrated in the PS-*b*-PDMS system, in which the PS and PDMS blocks exhibit a large difference in interfacial energies. The perpendicular nanostructured thin film with thin thickness can be used as a mask for nanolithography whereas the one with thick thickness can be used as a template for the fabrication of nanoporous monolith. The study offers a new approach using the architecture of star-block copolymers for controlled orientation of self-assembled BCP in the thin-film state and demonstrates the feasibility of using the star-block copolymer thin films for practical applications.

■ ASSOCIATED CONTENT

Supporting Information

The Supporting Information is available free of charge on the ACS Publications website at DOI: 10.1021/acs.macromol.5b02685.

Materials synthesis, instrumentation details, X-ray photoelectron spectroscopy data, interfacial energy difference between PS and PDMS at elevated temperature and theoretical framework (PDF)

■ AUTHOR INFORMATION

Corresponding Authors

*Tel 886-3-5738349; Fax 886-3-5715408; e-mail rmho@mx.nthu.edu.tw (R.-M.H.).

*Tel 905-525-9140; Fax 905-521-2773; e-mail shi@mcmaster.ca (A.-C. S.).

Present Address

[†]P.G.: Helmholtz-Zentrum Geesthacht, Institute of Polymer Research, Max-Planck-Straße 1, 21502 Geesthacht, Germany.

Notes

The authors declare no competing financial interest.

■ ACKNOWLEDGMENTS

The authors thank the National Science Council of the Republic of China, Taiwan, for financially supporting this research under Grant NSC 101-2221-E-007-038-MY3 and MOST 104-2633-M-007-001. A part of this work (synthesis and molecular characterization of the samples by P.G. and A.A.) was funded by the European Union Seventh Framework Program (FP7/2007-2013), as part of the LAMAND Project (Grant Agreement No. 245565). The research of A.G. and A.-C.S. is support by the Natural Science and Engineering Research Council (NSERC) of Canada. The SCFT computation was made possible by the facilities of the Shared Hierarchical Academic Research Computing Network (SHARCNET). We thank Dr. U.S. Jeng of the National Synchrotron Radiation Research Center (NSRRC) for his help in GISAXS experiments.

■ REFERENCES

(1) Bates, F. S.; Fredrickson, G. H. Block copolymers - Designer soft materials. *Phys. Today* **1999**, *52*, 32–38.
(2) Park, C.; Yoon, J.; Thomas, E. L. Enabling nanotechnology with self-assembled block copolymer patterns. *Polymer* **2003**, *44*, 6725–6760.

(3) Park, M.; Harrison, C.; Chaikin, P. M.; Register, R. A.; Adamson, D. H. Block copolymer lithography: Periodic arrays of similar to 10(11) holes in 1 square centimeter. *Science* **1997**, *276*, 1401–1404.

(4) Stoykovich, M. P.; Muller, M.; Kim, S. O.; Solak, H. H.; Edwards, E. W.; de Pablo, J. J.; Nealey, P. F. Directed assembly of block copolymer blends into nonregular device-oriented structures. *Science* **2005**, *308*, 1442–1446.

(5) Hawker, C. J.; Russell, T. P. Block copolymer lithography: Merging “bottom-up” with “top-down” processes. *MRS Bull.* **2005**, *30*, 952–966.

(6) Tavakkoli, K. G. A.; Gotrik, K. W.; Hannon, A. F.; Alexander-Katz, A.; Ross, C. A.; Berggren, K. K. Templating Three-Dimensional Self-Assembled Structures in Bilayer Block Copolymer Films. *Science* **2012**, *336*, 1294–1298.

(7) Knoll, A.; Horvat, A.; Lyakhova, K. S.; Krausch, G.; Sevink, G. J. A.; Zvelindovsky, A. V.; Magerle, R. Phase behavior in thin films of cylinder-forming block copolymers. *Phys. Rev. Lett.* **2002**, *89*, 035501.

(8) Mansky, P.; Russell, T. P.; Hawker, C. J.; Mays, J.; Cook, D. C.; Satija, S. K. Interfacial segregation in disordered block copolymers: Effect of tunable surface potentials. *Phys. Rev. Lett.* **1997**, *79*, 237.

(9) Kim, S. O.; Solak, H. H.; Stoykovich, M. P.; Ferrier, N. J.; de Pablo, J. J.; Nealey, P. F. Epitaxial self-assembly of block copolymers on lithographically defined nanopatterned substrates. *Nature* **2003**, *424*, 411–414.

(10) Ryu, D. Y.; Shin, K.; Drockenmuller, E.; Hawker, C. J.; Russell, T. P. A generalized approach to the modification of solid surfaces. *Science* **2005**, *308*, 236–239.

(11) Bates, C. M.; Seshimo, T.; Maher, M. J.; Durand, W. J.; Cushen, J. D.; Dean, L. M.; Blachut, G.; Ellison, C. J.; Willson, C. G. Polarity-Switchable Top Coats Enable Orientation of Sub-10-nm Block Copolymer Domains. *Science* **2012**, *338*, 775–779.

(12) Bitá, I.; Yang, J. K. W.; Jung, Y. S.; Ross, C. A.; Thomas, E. L.; Berggren, K. K. Graphoepitaxy of self-assembled block copolymers on two-dimensional periodic patterned templates. *Science* **2008**, *321*, 939–943.

(13) Bates, F. S.; Hillmyer, M. A.; Lodge, T. P.; Bates, C. M.; Delaney, K. T.; Fredrickson, G. H. Multiblock Polymers: Panacea or Pandora's Box? *Science* **2012**, *336*, 434–440.

(14) Khanna, V.; Cochran, E. W.; Hexemer, A.; Stein, G. E.; Fredrickson, G. H.; Kramer, E. J.; Li, X.; Wang, J.; Hahn, S. F. Effect of chain architecture and surface energies on the ordering behavior of lamellar and cylinder forming block copolymers. *Macromolecules* **2006**, *39*, 9346–9356.

(15) Vu, T.; Mahadevapuram, N.; Perera, G. M.; Stein, G. E. Controlling Domain Orientations in Thin Films of AB and ABA Block Copolymers. *Macromolecules* **2011**, *44*, 6121–6127.

(16) Matsen, M. W. Architectural Effect on the Surface Tension of an ABA Triblock Copolymer Melt. *Macromolecules* **2010**, *43*, 1671–1674.

(17) Jang, S.; Lee, K.; Moon, H. C.; Kwak, J.; Park, J.; Jeon, G.; Lee, W. B.; Kim, J. K. Vertical Orientation of Nanodomains on Versatile Substrates through Self-Neutralization Induced by Star-Shaped Block Copolymers. *Adv. Funct. Mater.* **2015**, *25*, 5414–5419.

(18) Wu, S. Surface and interfacial tensions of polymer melts. II. Poly(methyl methacrylate), poly(*n*-butyl methacrylate), and polystyrene. *J. Phys. Chem.* **1970**, *74*, 632–638.

(19) Jung, Y. S.; Chang, J. B.; Verploegen, E.; Berggren, K. K.; Ross, C. A. A Path to Ultranarrow Patterns Using Self-Assembled Lithography. *Nano Lett.* **2010**, *10*, 1000–1005.

(20) Cushen, J. D.; et al. Oligosaccharide/Silicon-Containing Block Copolymers with 5 nm Features for Lithographic Applications. *ACS Nano* **2012**, *6*, 3424–3433.

(21) Son, J. G.; Gotrik, K. W.; Ross, C. A. High-Aspect-Ratio Perpendicular Orientation of PS-*b*-PDMS Thin Films under Solvent Annealing. *ACS Macro Lett.* **2012**, *1*, 1279–1284.

(22) Kim, E.; et al. A Top Coat with Solvent Annealing Enables Perpendicular Orientation of Sub-10 nm Microdomains in Si-Containing Block Copolymer Thin Films. *Adv. Funct. Mater.* **2014**, *24*, 6981–6988.

- (23) Ji, S.; Liu, C. C.; Son, J. G.; Gotrik, K.; Craig, G. S. W.; Gopalan, P.; Himpfel, F. J.; Char, K.; Nealey, P. F. Generalization of the Use of Random Copolymers To Control the Wetting Behavior of Block Copolymer Films. *Macromolecules* **2008**, *41*, 9098–9103.
- (24) Ross, C. A.; Jung, Y. S.; Chuang, V. P.; Ilievski, F.; Yang, J. K. W.; Bitá, I.; Thomas, E. L.; Smith, H. I.; Berggren, K. K.; Vancso, G. J.; Cheng, J. Y. Si-containing block copolymers for self-assembled nanolithography. *J. Vac. Sci. Technol. B* **2008**, *26*, 2489–2494.
- (25) Matsen, M. W.; Schick, M. Microphase Separation in Starblock Copolymer Melts. *Macromolecules* **1994**, *27*, 6761–6767.
- (26) Matsen, M. W. Effect of Architecture on the Phase Behavior of AB-Type Block Copolymer Melts. *Macromolecules* **2012**, *45*, 2161–2165.
- (27) Jung, Y. S.; Ross, C. A. Orientation-controlled self-assembled nanolithography using a polystyrene-polydimethylsiloxane block copolymer. *Nano Lett.* **2007**, *7*, 2046–2050.
- (28) She, M. S.; Lo, T. Y.; Ho, R. M. Long-Range Ordering of Block Copolymer Cylinders Driven by Combining Thermal Annealing and Substrate Functionalization. *ACS Nano* **2013**, *7*, 2000–2011.
- (29) Zilliox, J. G.; Roovers, J. E. L.; Bywater, S. Preparation and Properties of Polydimethylsiloxane and Its Block Copolymers with Styrene. *Macromolecules* **1975**, *8*, 573–578.
- (30) Bellas, V.; Iatrou, H.; Hadjichristidis, N. Controlled Anionic Polymerization of Hexamethylcyclotrisiloxane. Model Linear and Miktoarm Star Co- and Terpolymers of Dimethylsiloxane with Styrene and Isoprene. *Macromolecules* **2000**, *33*, 6993–6997.
- (31) Lo, T. Y.; Ho, R. M.; Georgopoulos, P.; Avgeropoulos, A.; Hashimoto, T. Direct Visualization of Order–Order Transitions in Silicon-Containing Block Copolymers by Electron Tomography. *ACS Macro Lett.* **2013**, *2*, 190–194.
- (32) Hamley, I. *Developments in Block Copolymer Science and Technology*; Wiley: New York, 2004; Chapter 8.
- (33) Fredrickson, G. H. *The Equilibrium Theory of Inhomogeneous Polymers*; Clarendon: Oxford, 2006.
- (34) Miao, B.; Yan, D.; Wickham, R. A.; Shi, A. C. The nature of phase transitions of symmetric diblock copolymer melts under confinement. *Polymer* **2007**, *48*, 4278–4287.

Supporting Information for:

Orienting Block Copolymer Thin Films via Entropy

Ting-Ya Lo¹, Ashkan Dehghan², Prokopios Georgopoulos³†, Apostolos Avgeropoulos³, An-Chang Shi^{2} and Rong-Ming Ho^{1*}*

¹ Department of Chemical Engineering, National Tsing Hua University, Hsinchu 30013, Taiwan, R.O.C.

² Department of Physics and Astronomy, McMaster University, Hamilton, Ontario, Canada

³ Department of Materials Science Engineering, University of Ioannina, University Campus, Ioannina 45110, Greece

† Present address: Helmholtz-Zentrum Geesthacht, Institute of Polymer Research, Max-Planck-Straße 1, 21502 Geesthacht, Germany

Interfacial Energy Difference between PS and PDMS at Elevated Temperature

To investigate the wettability of the constituted block on different interfaces, the interfacial energy differences between PS and PDMS for the substrate ($\gamma_{\text{PDMS-sub}}^{280\text{oC}} - \gamma_{\text{PS-sub}}^{280\text{oC}}$) and air surface ($\gamma_{\text{PS-air}}^{280\text{oC}} - \gamma_{\text{PDMS-air}}^{280\text{oC}}$) were estimated. It is well documented that the surface tension of polymers varies linearly with temperature with a slope given by $d\gamma/dT$.^{1,2} Consequently, the surface tensions of the PS and PDMS at 280°C were estimated using the $d\gamma_{\text{PS}}/dT \sim -0.076$ (mN/m°C)³ and $d\gamma_{\text{PDMS}}/dT \sim -0.048$ (mN/m°C),⁴ respectively. Table S1 summarize the polar and dispersion components of the surface energies for the PS and PDMS homopolymers at room temperature and at 280°C

Table S1. γ^d and γ^p values for the PS and PDMS materials at room temperature and 280°C.

	Room temperature		At 280°C	
Materials	γ^d (mN/m)	γ^p (mN/m)	γ^d (mN/m)	γ^p (mN/m)
SiO2	21.9	50	21.9	50
PDMS	19	0.8	6.7	0
PS	33.9	6.8	14.4	0

Meanwhile, the interfacial energies of PS and PDMS for the substrate upon thermal annealing at 280°C were estimated as^{1,2}

$$\gamma_{12} = \gamma_1 + \gamma_2 - W_{12} \quad \text{Eq[1]}$$

Where γ_1 is the surface tension of PS or PDMS, γ_2 is the surface tension of the SiO₂ substrate, and W_{12} is the work of adhesion of PS or PDMS with the SiO₂ substrate. The work of adhesion (W_{12}) of PS or PDMS with the SiO₂ substrate was obtained using the geometric-mean equation as^{1,2}

$$W_{12} = 2(\gamma_1^d \gamma_2^d)^{\frac{1}{2}} + 2(\gamma_1^p \gamma_2^p)^{\frac{1}{2}} \quad \text{Eq[2]}$$

Where the terms with superscript p and d are referred to the polar and dispersion components of surface tensions, respectively. Consequently, the interfacial energy of PS or PDMS for the substrate can be calculated by

$$\gamma_{PDMS-SiO_2}^{280^\circ C} = \gamma_{PDMS}^{280^\circ C} + \gamma_{SiO_2}^{280^\circ C} - W_{PDMS-SiO_2}^{280^\circ C} \quad \text{Eq[3]}$$

$$\gamma_{PS-SiO_2}^{280^\circ C} = \gamma_{PS}^{280^\circ C} + \gamma_{SiO_2}^{280^\circ C} - W_{PS-SiO_2}^{280^\circ C} \quad \text{Eq[4]}$$

Finally the $\Delta \gamma$ value for the substrate and for the air surface were calculated as $\Delta \gamma_{\text{sub}} = \gamma_{PDMS-sub}^{280^\circ C} - \gamma_{PS-sub}^{280^\circ C} = 3.6$ (mN/m) and $\Delta \gamma_{\text{air}} = \gamma_{PS-air}^{280^\circ C} - \gamma_{PDMS-air}^{280^\circ C} = 7.7$ (mN/m), respectively.

Theoretical Framework

In this section, we present a brief description of the Self-Consistent Field Theory (SCFT). A more comprehensive description of the SCFT formalism can be found in the literature.^{5,6} In what follows, we use linear AB-diblock copolymers as a model system to describe the SCFT. Generalizing the theory to $(AB)_n$ star-block copolymers is straightforward. We consider a system of n AB-diblock copolymers of length N , in a thin film of height h . The monomer-monomer interactions are modeled using the Flory-Huggins parameter χ . We will also introduce a parameter $h_\alpha(r)$ to control the polymer/substrate and polymer/air interactions, where the subscript $\alpha = \{A, B\}$. The asymmetry in the air and substrate interactions is modeled by allowing $h_\alpha(r)$ to be different for each polymer species.

We define the densities of the polymers at position r in the system as

$$\phi_A(r) = \frac{1}{\rho} \sum_{i=1}^n \int_0^{f_{AN}} \delta(r - R_i^A(s)), \quad \text{Eq[1]}$$

$$\phi_B(r) = \frac{1}{\rho} \sum_{i=1}^n \int_0^{f_{BN}} \delta(r - R_i^B(s)), \quad \text{Eq[2]}$$

where f_A and f_B are the fractions of the A and B in AB-diblock copolymers. In the above equation, $R_i^A(s)$ and $R_i^B(s)$ are space curves determining the position of polymer segment s in the system. In our model, we assume that all polymer species have the same monomer density ρ .

The thermodynamic properties of the system can be most conveniently described using a canonical ensemble at fixed temperature, volume and concentration. Using the above definitions, we can write the partition function as

$$Z = \frac{1}{n!} \int \prod_{i=1}^n D[R_i^{AB}(s)] P[R_i^{AB}(s)] e^{-\beta E[\phi]} \prod_r \delta[\phi_A(r) + \phi_B(r) - 1], \quad \text{Eq[3]}$$

where the delta function is introduced to ensure the incompressibility. Here we assume that polymers are flexible Gaussian chains, with Weiner measure given by

$$P[R_i^{AB}(s)] \propto \exp \left[\frac{-3}{2b^2} \int_0^N ds \left(\frac{dR_i^{AB}(s)}{ds} \right)^2 \right]. \quad \text{Eq[4]}$$

Here, b is the Kuhn length of the polymers, which we assume to be the same for all polymer species.

The energy of the system is consist of two parts $E[\phi] = W[\phi] + H[\phi]$, where $W[\phi]$ is the energy due to the local interactions between the polymers and $H[\phi]$ captures the interactions between the polymers and the air/substrate surfaces. We can write $E[\phi]$ as

$$E[\phi] = \int dr \chi_{AB} \phi_A \phi_B + \sum_{\alpha=A,B} \int dr h_{\alpha}(r) \phi_{\alpha}(r), \quad \text{Eq[5]}$$

where, $h(r)$ controls the polymer/air and polymer/substrate interactions. We assume that surface interactions are short range and write, $h_{\alpha}(r) = \chi_{\alpha}^{Air}$ at the air surface, $h_{\alpha}(r) = \chi_{\alpha}^{Sub}$ at the substrate and $h_{\alpha}(r) = 0$ otherwise. We apply the SCFT formalism [1-2], and rewrite the partition function as

$$Z = \int \prod_{\alpha=A,B} D[\phi_{\alpha}(r)] D[\omega_{\alpha}(r)] \prod_r \delta[\phi_A(r) + \phi_B(r) - 1] \exp \left[\frac{-F[\phi, \omega]}{kT} \right], \quad \text{Eq[6]}$$

where, $\omega_{\alpha}(r)$ are the auxiliary fields. In the above equation, the free energy functional is defined as

$$\begin{aligned}
\frac{F[\phi, \omega]}{kT\rho} &= \int dr \chi_{AB} \phi_A(r) \phi_B(r) \\
&+ \sum_{\alpha=A,B} \left[\int dr h_\alpha(r) \phi_\alpha(r) \right. \\
&\left. - \int dr \omega_\alpha(r) \phi_\alpha(r) \right] - V \frac{1}{N} \ln\left(\frac{Q_{AB}}{\phi}\right), \quad \text{Eq[7]}
\end{aligned}$$

where Q_{AB} is the single chain partition function of the AB-diblock copolymers. We can write Q_{AB} as

$$\begin{aligned}
Q_{AB} &= \frac{1}{V} \int D[R_i^{AB}(s)] P[R_i^{AB}(s)] \delta[R_i^A(N_A) \\
&- R_i^B(N_B)] \exp\left[- \sum_{\alpha=A,B} \int_0^{N_\alpha} ds \omega_\alpha(R_i^\alpha(s))\right]. \quad \text{Eq[8]}
\end{aligned}$$

Here, the delta function ensures the connectivity of the A/B blocks. We will also rewrite the incompressibility condition given in equation [6] by using the identity

$$\begin{aligned}
&\prod_r \delta[\phi_A(r) + \phi_B(r) - 1] \\
&= \int D[\eta(r)] \exp\left[\int dr \eta(r) (\phi_A(r) + \phi_B(r) - 1)\right], \quad \text{Eq[9]}
\end{aligned}$$

where $\eta(r)$ is a Lagrange multiplier.

We can determine the mean field solutions to the free energy functional by demanding that it is stationary with respect to variations in $\phi_\alpha(r)$, $\omega_\alpha(r)$ and $\eta(r)$ fields. This results in the following set of self-consistent field equations

$$\begin{aligned}
\phi_A(r) &= \frac{1}{Q_{AB}N} \int_0^{f_A N} ds q_A(r, s) q_A^\dagger(r, f_A N - s), \\
\phi_B(r) &= \frac{1}{Q_{AB}N} \int_0^{f_B N} ds q_B(r, s) q_B^\dagger(r, f_B N - s), \\
\omega_A(r) &= \chi_{AB} \phi_B(r) + h_A(r) + \eta(r), \\
\omega_B(r) &= \chi_{AB} \phi_A(r) + h_B(r) + \eta(r), \\
\phi_A(r) + \phi_B(r) &= 1.
\end{aligned} \tag{Eq[10]}$$

Here, $q_\alpha(r, s)$ and $q_\alpha^\dagger(r, s)$ are the forward and complementary end-integrated propagators. The propagators can be determine by solving the modified diffusion equations

$$\begin{aligned}
\frac{\partial q_\alpha(r, s)}{\partial s} &= \frac{b_\alpha^2 N}{6} \nabla^2 q_\alpha(r, s) - \omega_\alpha(r), \\
\frac{\partial q_\alpha^\dagger(r, s)}{\partial s} &= \frac{b_\alpha^2 N}{6} \nabla^2 q_\alpha^\dagger(r, s) - \omega_\alpha(r).
\end{aligned} \tag{Eq[11]}$$

We solve the modified diffusion equations using the real-space pseudo-spectral technique with the appropriate initial and boundary conditions.

SCFT Calculations

The effects of block copolymer architecture on the orientation of lamellae- and cylinder-forming BCPs were investigated using Self-Consistent Field Theory (SCFT) calculations. Specifically, the phase behavior of a series of n-armed AB star-block copolymers with n=1, 2, 3 and 4 (each molecule is formed by joining n diblocks together with their A-ends) was studied using SCFT. The case of n=1 corresponds to a linear AB-diblock copolymer. In our model, the A-species interact favorably with the air surface and tend to wet the polymer-air interface. The volume fraction of the A and B blocks and the A-B interaction were chosen such that the n-armed star-block copolymers form lamellar and cylinder phases in bulk. We examined the phase behavior of the n-armed AB star-block copolymers confined to thin films of

thickness $h \approx 2d_0$ and $3d_0$, where d_0 is the period of the bulk lamellar and cylinder phases for the n-armed star-block copolymers. The thickness of the film was chosen such that there would be no structural frustration due to film thickness.⁷ It should be pointed out that, due to the limitation of computational power, the film thickness used in the SCFT calculations is much smaller than the experimental values. Also, it is important to note that the polymer/air and polymer/substrate interaction parameters are chosen to approximate the experimentally measured surface interactions. As a result, the comparison of the theoretical results to experiments is qualitative. Instead, the theoretical study reveals the origin of the entropic effect is the topology of the star-copolymers. The relative polymer-substrate and polymer-air surface interactions were selected to resemble those of the experimental system. Specifically, $\Delta\chi = \chi_{BAir} - \chi_{AAir}$ was chosen as a controlling parameter to tune the relative interaction between air and the A-B species, while the parameters χ_{ASub} , χ_{BSub} , χ_{AB} , f_B and the film thickness h were fixed. For both lamellae- and cylinder-forming systems, we consider the free energies of the parallel, perpendicular and mixed morphologies, where the density profiles for the morphologies studied are shown in **Figure S5**. In the parallel/perpendicular phases, for both lamellae- and cylinder-forming systems, microdomains are formed parallel/perpendicular to the air and substrate interfaces, respectively. In the mixed phase however, owing to the large polymer-air interaction, microdomains are formed parallel to the air surface at the air interface and perpendicular in the bulk region of the film initiated from the substrate.

Morphological transitions between parallel and perpendicularly oriented nanostructures were determined by comparing their free energies calculated from SCFT calculations. In **Figure S6** and **S7**, we show the free energy of the parallel, perpendicular and mixed morphologies for the lamellae- and cylinder-forming 1-, 2-, 3- and 4-arm star-block copolymers as a function of $\Delta\chi$. For both lamellae- and cylinder-forming systems, the perpendicular phase has the lowest free energy at low $\Delta\chi$ values. In this region, the difference between the A- and B-air surface interactions is small, and thus we expect the perpendicular phase to be the stable structure. As $\Delta\chi$ is increased, a phase transition from the perpendicular to parallel phase in both lamella- and cylinder-forming systems can be observed. Note that for both lamella- and cylinder-forming systems, the mixed morphology is a metastable phase with

free energy greater than the perpendicular and parallel phases. We will now examine the critical value of $\Delta\chi$ at which this transition occurs. As the difference in polymer-air interaction between the A and B species is increased ($\Delta\chi$ is increased), it becomes energetically more favorable to orient the microdomains in the parallel configuration. However, there is an entropic penalty for reorienting the microdomains parallel to the surfaces. There exists a critical $\Delta\chi$ beyond which the enthalpic contribution to the free energy outweighs the entropic effect and the parallel phase has the lower free energy. Owing to the entropic penalty for orienting the microdomains parallel to the surfaces for star-block copolymers, the critical $\Delta\chi$ must occur at larger values for chains with greater number of arms. In **Figure S8A and B**, we present the difference in the free energy between the parallel and perpendicular phases (ΔfE) as a function of $\Delta\chi$ for 1-, 2-, 3- and 4-arm star-block copolymers. In both cases, the transition from the perpendicular to the parallel phase occurs at larger $\Delta\chi$ values for copolymers with greater number of arms. These theoretical results clearly indicate that the entropic penalty for reorienting the n-armed star-block copolymers to parallel morphologies is larger for BCPs with larger number of arms. As a result, this theoretical conclusion provides qualitative support to our experimental observations. The effect of chain architecture on the phase behavior of n-arm star-block copolymers can be further understood by examining the distribution of the blocks in the perpendicular phase, which are revealed by the density profiles of the lamellae- and cylinder-forming systems. As shown in **Figure S9A and B** for the case with $\Delta\chi=0$, in both lamellae- and cylinder-forming copolymers, the microdomains extend from the substrate surface to the air interface. On the other hand, a wetting layer with parallel cylinders/lamellae at the air interface is formed at smaller $\Delta\chi$ for the 1- and 2-arm star-block copolymers, but not the 3- and 4-arm copolymers. The theoretical results presented here provide complementary evidence, supporting the entropy-driven orienting effect *via* varying the topology of the star-copolymers. On the basis of the theoretical studies above, it is feasible to suppress the enthalpy interaction at the air/polymer interface for the formation of throughout perpendicularly oriented lamellae or cylinders in the thin-film state from the self-assembly of star-block copolymers with high surface energy core block (as shown in

Figure 1) while there are a few layers of parallel lamellae or cylinders at the air/polymer interface due to the low surface energy of the PDMS core block.

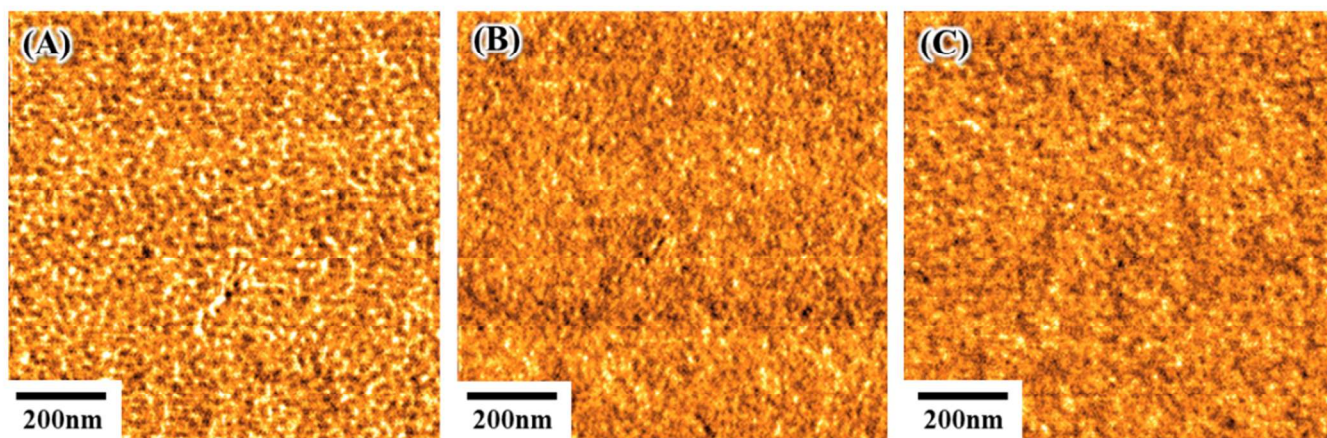


Figure S1. Tapping mode SPM top-view phase images of $(S_{13.7-b-D_{7.11}})_3$ thin film (A) before thermal annealing; and after thermal annealing at 280 °C for (B) 5 min and (C) 10 min with a thicknesses of 340nm.

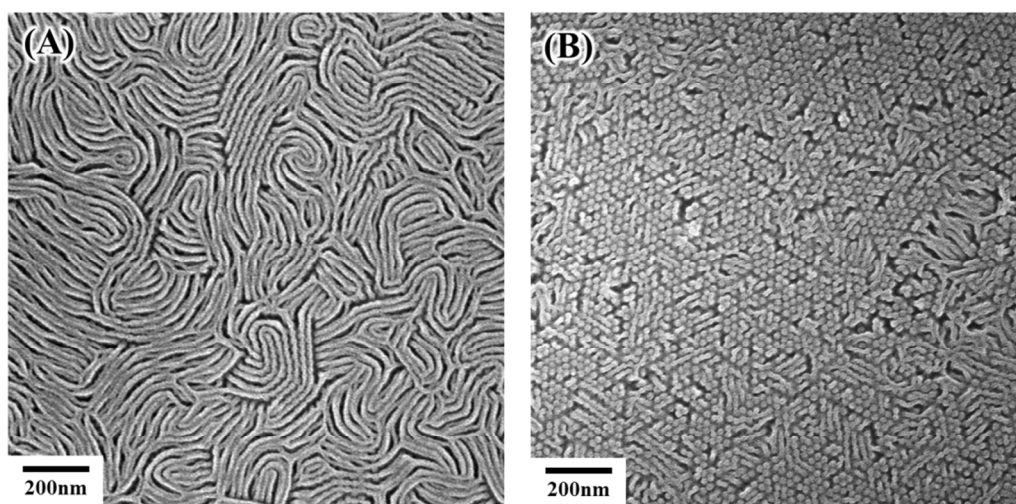


Figure S2. The 340 nm thick $(S_{13.7-b-D_{7.1}})_3$ films after second round thermal annealing process by flipping the annealed film sample over, and then thermal annealing again at 280 °C for 30 min. (A) top-view (bottom side for the 1st round) and (B) bottom-view (top side for the 1st round) FESEM images of the thin-film sample after RIE treatment.

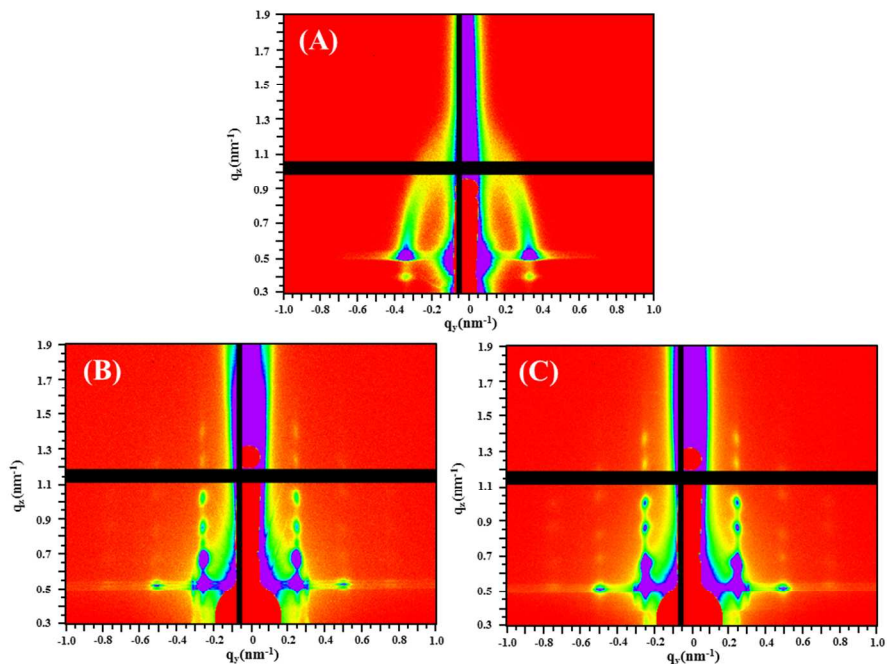


Figure S3. 2D GISAXS pattern of $(S_{13.7-b-D_{7.11}})_1$ thin film before thermal annealing (A) and after thermal annealing at 280 °C for 30 min with thicknesses of (B) 120nm, (C) 200nm, respectively.

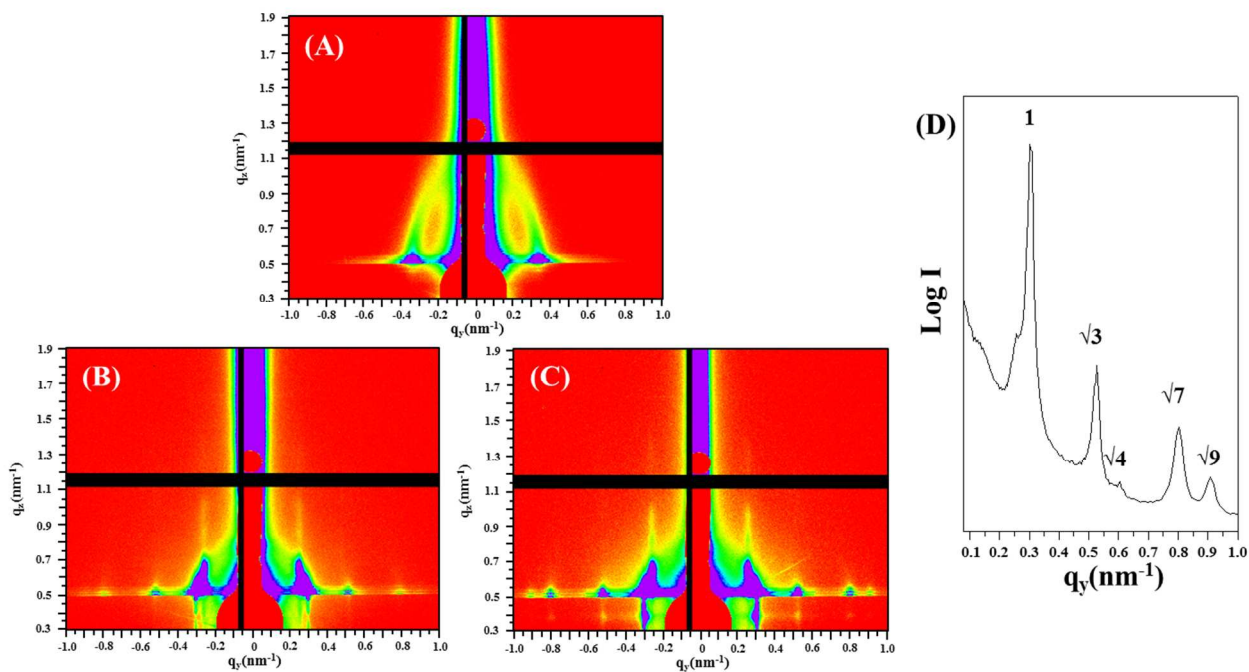


Figure S4. 2D GISAXS pattern of $(S_{13.7-b-D_{7.11}})_3$ thin film before thermal annealing (A) and after thermal annealing at 280 °C for 30 min with thicknesses of (B) 120nm, (C) 200nm, respectively. (D) q_y scans from 2D GISAXS pattern of Fig. 3E (q_y scans were extracted at $q_z = 0.55 \text{ nm}^{-1}$).

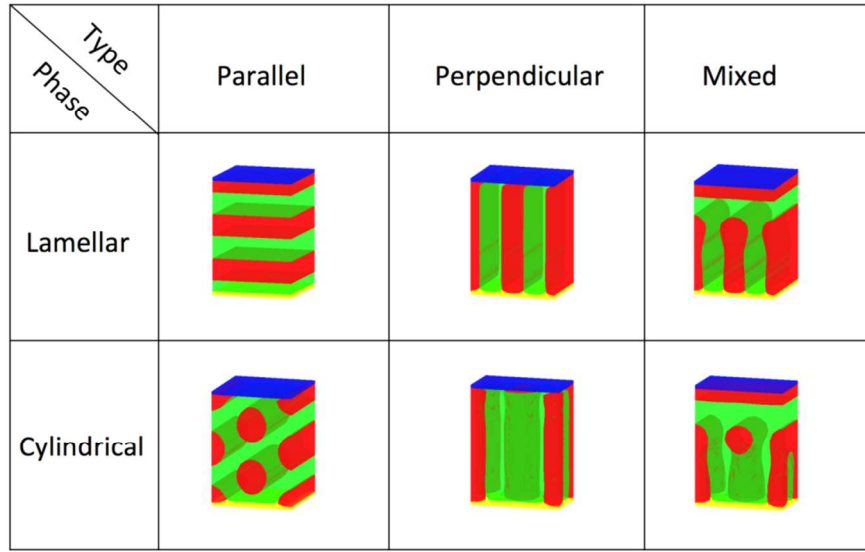


Figure S5. Density profiles demonstrating the parallel, perpendicular and mixed, lamellae- and cylinder-forming morphologies. In the above density profiles, the A- and B-species are represented using the red and green colors, respectively. Similarly, the polymer-air and polymer-substrate interfaces are shown using blue and yellow colors.

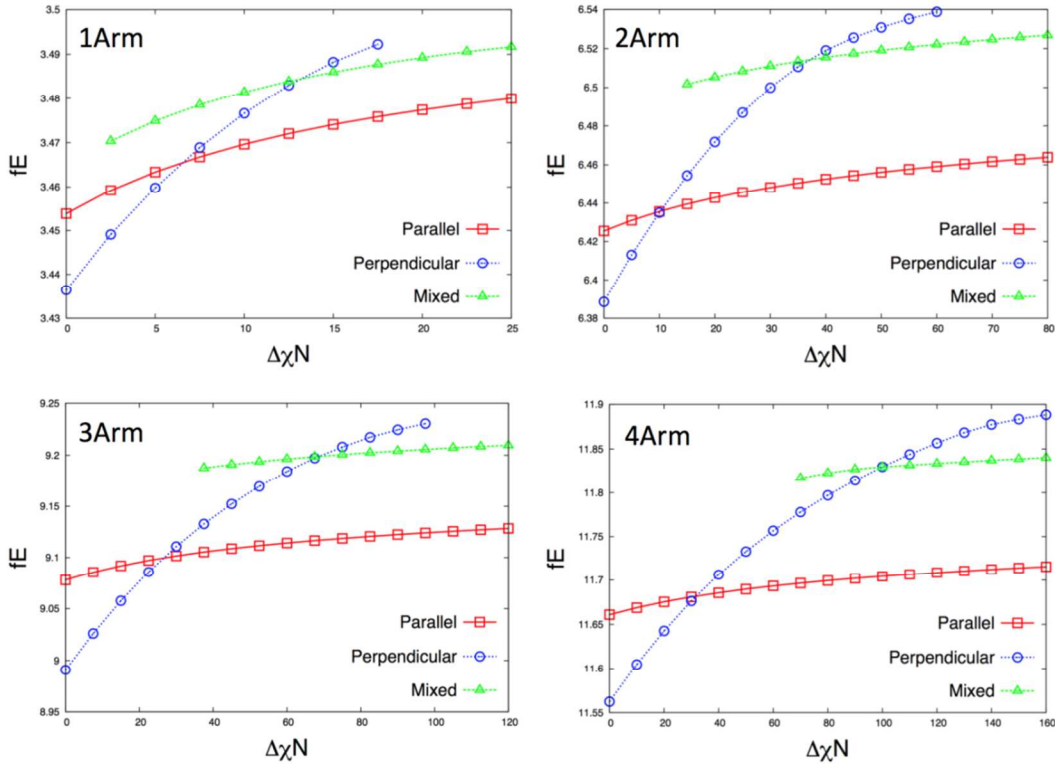


Figure S6. Free energy calculated using SCFT as a function of $\Delta\chi = \chi_{BAir} - \chi_{AAir}$ for the lamellae-forming 1-, 2-, 3- and 4-arm star-block copolymers. We plot the free energy for the parallel, perpendicular and mixed phases for a system with $f_A = 0.5$, $\chi_{AB} = 0.14$, $\chi_{ASub} = 0.08$, $\chi_{BSub} = 0.06$ and $h = 2d_o$.

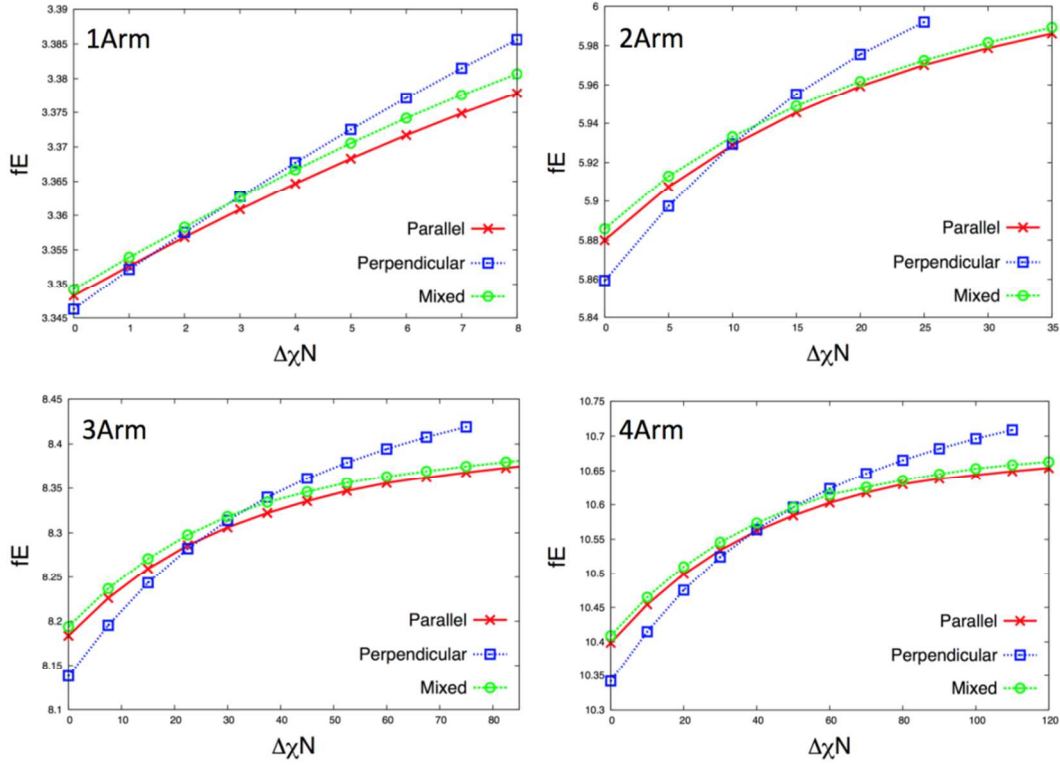


Figure S7. Free energy calculated using SCFT as a function of $\Delta\chi = \chi_{BAir} - \chi_{AAir}$ for the cylinder-forming 1-, 2-, 3- and 4-arm star-block copolymers. We plot the free energy for the parallel, perpendicular and mixed phases for a system with $f_A = 0.35$, $\chi_{AB} = 0.14$, $\chi_{ASub} = 0.08$, $\chi_{BSub} = 0.06$ and $h = 2d_o$.

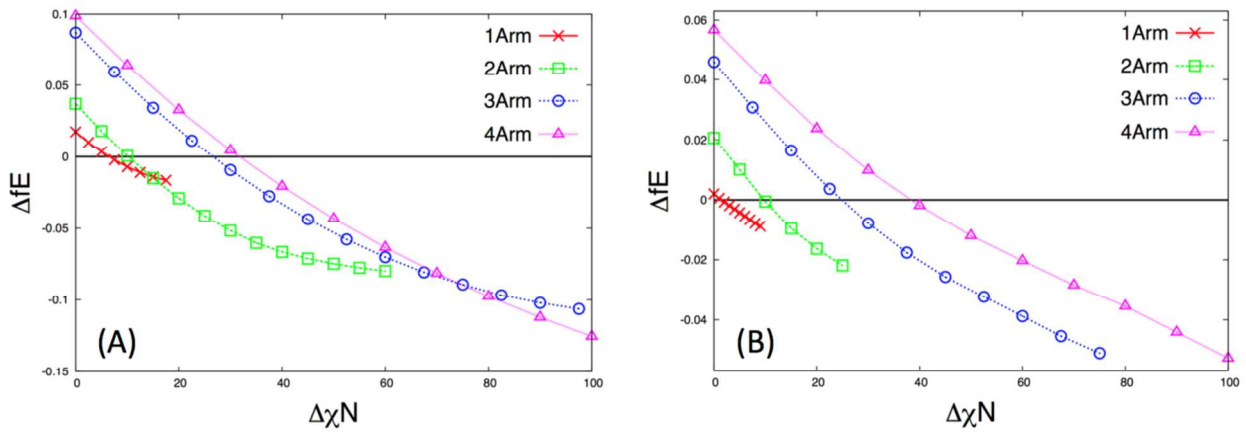


Figure S8. The free energy difference between the parallel and perpendicular phase for (A) the lamellae- and (B) cylinder-forming n -arm star-block copolymer thin films with $h=2d_0$. Here, $\Delta f \equiv f_{\text{parallel}} - f_{\text{perpendicular}}$ plotted as a function of $\Delta\chi \equiv \chi_{BAir} - \chi_{AAir}$.

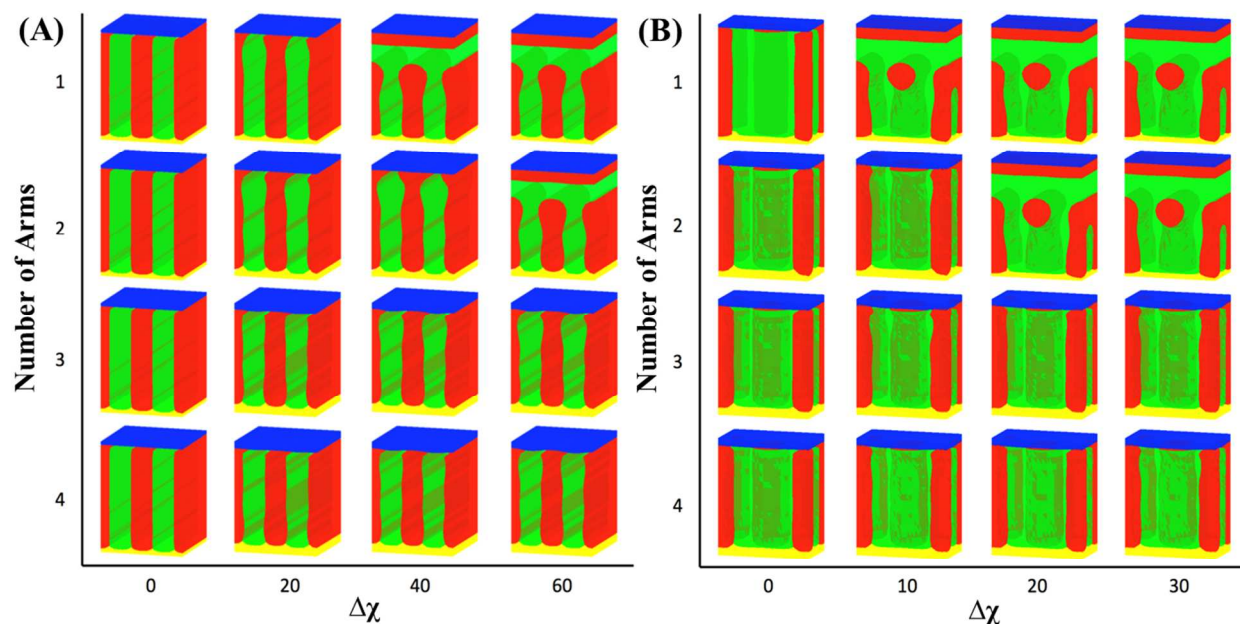


Figure S9. 3-D density profiles for the (A) lamellae-forming and (B) cylinder-forming 1, 2, 3 and 4 arm star-block copolymers as a function of $\Delta\chi$.

References

1. Wu, S. *Polymer Interface and Adhesion*; Marcel Dekker: New York, **1982**; Chapter 5
2. Mark, J. E. *Physical Properties of Polymers Handbook*; Woodbury, New York, **1996**; 669-677
3. Moreira, J. C. Influence of temperature, molecular weight, and molecular weight dispersity on the surface tension of PS, PP, and PE. I. Experimental *Journal of Applied Polymer Science* **2001**, *82*, 1907-1920.
4. Roe, R. J. Surface tension of polymer liquids *J. Phys. Chem* **1968**, *72*, 2013-2017.
5. Shi, A.-C., *Self-consistent Field Theory of Block Copolymers*, in *Developments in Block Copolymer Science and Technology*, Edited by I. W. Hamley (Wiley, New York, 2004), Chap. 8.
6. Fredrickson, G. H. *The Equilibrium Theory of Inhomogeneous Polymers* (Clarendon, Oxford, 2006).
7. Shi, A. C., Li, B. Self-assembly of diblock copolymers under confinement *Soft Matter* **2013**, *9*, 1398-1413.

7 | Unbinding Transition in Pentablock Terpolymer/Homopolymer Blends

7.1 INTRODUCTION

Block copolymers can self-assemble into a variety of inhomogeneous phases with periods on the order of 10-100 nm. The highly ordered structures formed from block copolymers have potential applications in the nanofabrication of photonics crystals, nanowires, nanolithographic templates and quantum dots (2, 3, 63–71). The increasing demand for engineering new polymeric materials with functional features tuned for a specific applications has been one of the driving forces for the discovery of new polymeric systems with complex properties. In order to provide a comprehensive understanding of the phase behaviour of a polymeric system, one must investigate a complex and multidimensional parameters space. It is often highly time consuming and expensive to carry out a thorough experimental study of the phase behaviour of multiblock copolymers. From this perspective, theoretical and computational studies can provide a useful guideline for the discovery of new polymeric materials with complex morphologies.

multiblock copolymers have been the subject of numerous experimental and theoretical studies with their phase behaviour examined extensively in bulk and confined geometries (72–80). Although diblock and triblock copolymers can self-assemble into a variety of ordered structures, the rather small parameter space for these systems sets a limit on the complexity of these ordered structures. One approach for engineering materials with intricate morphologies is to synthesize multiblock copolymers with more complex architectures (23, 81–84). In a recent study, Xie *et al.* carried out a comprehensive study of the phase behaviour of $B_1AB_2CB_3$ pentablock terpolymers using the self-consistent field theory (SCFT) (81). The authors showed that, for the $B_1AB_2CB_3$ pentablock copolymer in which the *A* and *C* polymer species form spherical domains,

the copolymers could self-assemble into a variety of mesocrystals with space group symmetries similar to those of binary ionic crystals (81).

Among the many mesocrystals predicted by Xie *et al.*, the α -BN phase is of particular interest for its structural resemblance to the graphite crystal. Similar to the carbon atoms in the graphite structure, the A and C polymer spheres form stacked layers of honeycomb lattices. It is interesting to examine whether the analogy between the α -BN phase and the graphite structure extends beyond the similarities in the symmetry of the two phases. In particular, it is interesting to investigate whether there exists a single-layer α -BN phase similar to the single-layer graphene structure.

To explore these questions, we study the unbinding transition of the α -BN phase in the $B_1AB_2CB_3$ Pentablock Terpolymer/ H Homopolymer blends. The unbinding transition of ordered structures in polymeric systems has been studied extensively in ternary blends of AB/A/B diblock copolymers and homopolymers (85–89). In a recent study, using Monte-Carlo simulations, Pike *et al.* examined the effects of added homopolymers on the period of lamellar domains in AB/A/B blends (85). The authors showed that increasing the concentration of homopolymers could result in the macrophase separation of the blends into block copolymer rich, homopolymer rich domains. Similar phase behaviour has also been reported in experimental and self-consistent field theory studies of block copolymer/homopolymer blends (87, 90–92).

In the following section, we present a SCFT model for the $B_1AB_2CB_3$ pentablock terpolymers/ H homopolymer blends. We investigate the phase behaviour of the pentablock copolymers as a function of added homopolymers and construct a phase diagram in the ϕ_H - f_{B_2} plane. We focus on the unbinding transition in the α -BN phase as a function of ϕ_H and investigate the effects of added homopolymers on the α -BN domain spacing.

7.2 RESULTS AND DISCUSSION

In this section, we investigate the unbinding transition of the α -BN phase in $B_1AB_2CB_3$ Pentablock Terpolymer/ H Homopolymer blends. A schematic diagram for the $B_1AB_2CB_3$ /H system is shown in Figure 7. The thermodynamic properties of the blend are described using the grand canonical ensemble, where the volume fractions for the pentablock terpolymers ϕ_P and homopolymers ϕ_H are determined by their respective

chemical potentials, μ_P and μ_H . We calculate the equilibrium phase behaviour of the $B_1AB_2CB_3/H$ for a set of blend parameters. The $B_1AB_2CB_3$ -H blends have a rather large and complex phase space, with many degrees of freedom. In our study however, we restrict our calculations to a small subset of these parameters, while keeping the remaining parameters constant.

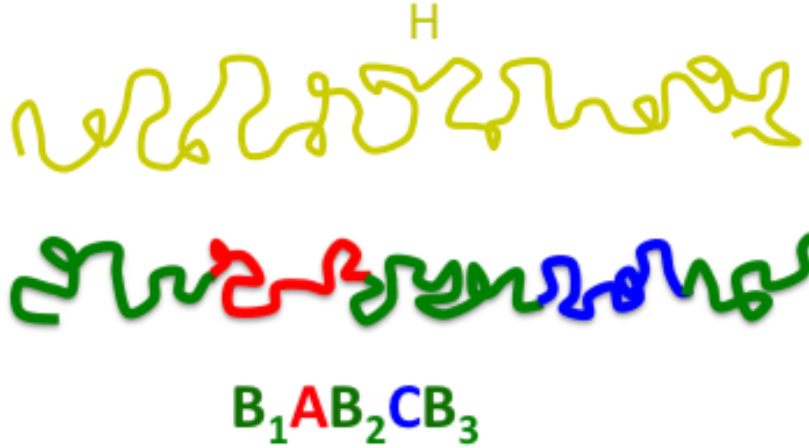


Figure 7: A schematic diagram for the $B_1AB_2CB_3/H$ system.

Among those parameters are the lengths of the A and C blocks, which are kept constant at $f_A=f_C=0.1$. The length of the middle block however is used as a controlling parameter such that: $f_{B_1}=f_{B_3}=0.5(0.8 - f_{B_2})$. We also fix the relative degree of polymerization between the pentablock terpolymers and homopolymer chains such that $N_P=N_H$. The interactions between the polymer species are defined using the Flory-Huggins parameters $\chi_{\alpha\beta}$, where $\alpha, \beta = A, C, B_1, B_2, B_3, H$. We fix the interactions between the polymer species such that, $\chi_{AB_\alpha}N_P = \chi_{CB_\alpha}N_P = \chi_{AC}N_P = \chi_{AH}N_P = \chi_{CH}N_P = 80$ and $\chi_{B_\alpha B_\beta}N_P = \chi_{B_\alpha H}N_P = 0$, where $\alpha, \beta = 1, 2, 3$.

Using self-consistent field theory, we calculate the phase behaviour of the $B_1AB_2CB_3$ melt, based on the set of parameters described above. The ordered phases used in our calculations are presented in Figure 8, where the binary polymer mesocrystals have group symmetries of the $\alpha - BN$, $NaCl$, $C_{A/C}$ and $CsCl$ ionic crystals. It is important to note that the average domain size in the polymeric system is of the order of ~ 10 -100 nm.

Among the $B_1AB_2CB_3$ mesocrystals, the α -BN structure is of particular interest for its structural re-

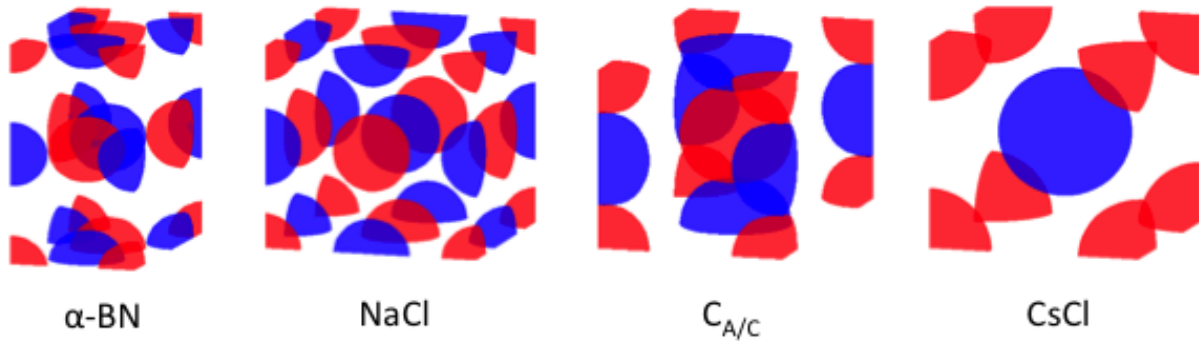


Figure 8: Density profiles for the α -BN, NaCl, $C_{A/C}$ and CsCl morphologies, constructed for the $B_1AB_2CB_3$ melt with $\phi_H=0$. Here, only the A (red) and C (blue) species are presented.

semblance to graphite. In Figure 9.a we present a schematic diagram for the graphite structure, which is composed of layers of carbon atoms packed in a honeycomb lattice (93). Similarly, in Figure 9.b we present the side and top-down view of the α -BN phase, where the A and C blocks form layers of honeycomb packed spheres.

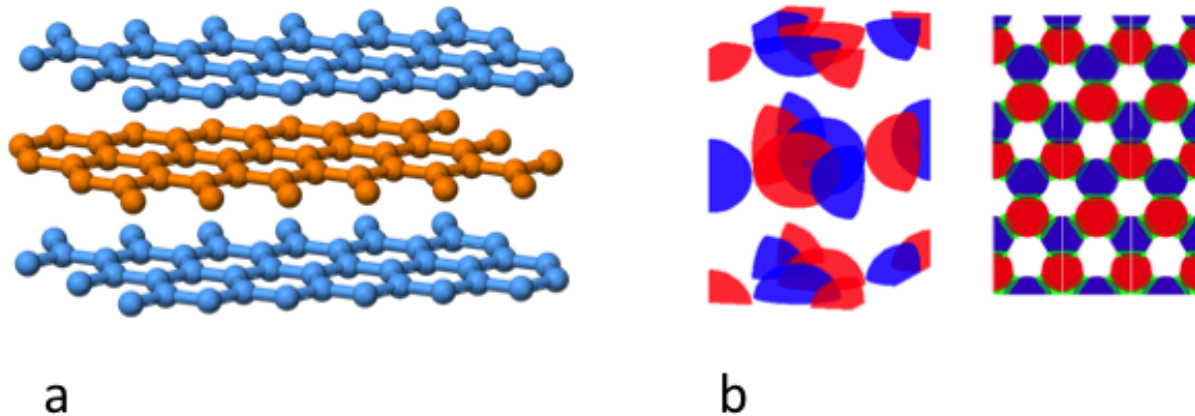


Figure 9: Figure (a), shows a schematic model a graphite structure (public domain image). In Figure (b), we present a side and top-down view of the α -BN morphology.

One of the many unique properties of the graphite phase is the large difference in the interactions between the carbon atoms within the planes and between the planes (93). The carbon atoms within each layer

are held together by strong covalent bonds, whereas the interactions between the layers are governed by much weaker van der Waals forces (93). This unique property of the graphite phase allows for the unbinding of the graphite layers into single-layer graphene sheets. Similar to the graphite structure, the A and C polymer spheres in the α -BN phase are held together via weak and strong connections. The weak bonds are the B_1 and B_3 tail blocks, and the strong bonds between the A/C spheres are the B_2 bridge blocks. By investigating the tail/bridge density distributions within the α -BN structure, we find that, similar to graphite, the B_2 bridge connections lie predominately within the planes, whereas the B_1 and B_3 tail blocks are concentrated in the region between the planes.

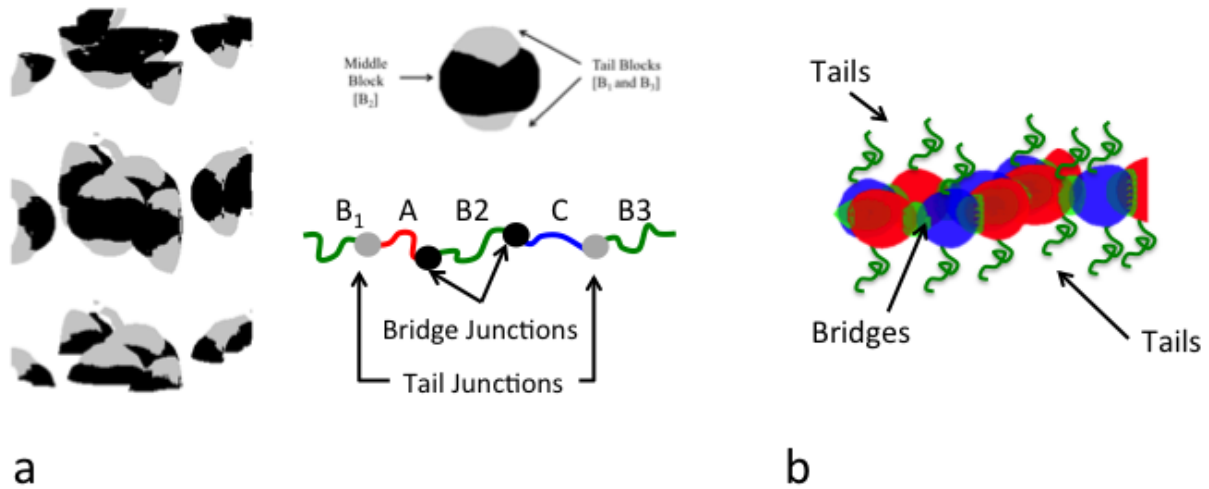


Figure 10: In Figure (a) we present the density distribution for the tail and bridge junctions, shown in grey and black respectively. In Figure (b), we present a schematic diagram showing that the B_2 bridge blocks concentrated within the α -BN plane, whereas the B_1 and B_3 tail blocks concentrate in the region between the planes.

In Figure 10.a, we present the density distributions for the tail and bridge blocks, plotted in black and grey colours respectively. The results shown here indicate that the B_2 blocks form bridges between the A and C spheres, whereas the B_1 and B_3 blocks concentrate in the region between the planes. This is shown more clearly in the schematic diagram presented in Figure 10.b. Similar calculations done for other mesocrystals are presented in Figure 11.

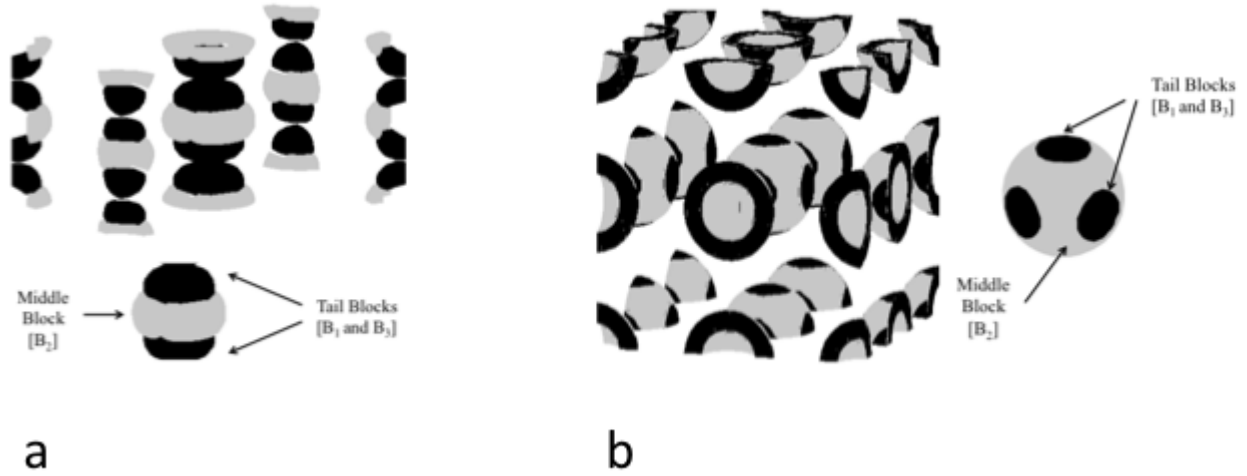


Figure 11: In Figures (a) and (b) we present the density profiles for the tail and bridge junctions for the $C_{A/C}$ and NaCl phases respectively.

We now focus on the unbinding transition of the α -BN phase as a function of added homopolymers. Based on our analysis of the bridge/tail densities, we expect the added homopolymers to concentrate in the region between the α -BN layers. Therefore, an increase in ϕ_H should result in an increase in the distance between α -BN layers. To examine this effect, we study the phase behaviour of the $B_1AB_2CB_3$ as a function of added homopolymers. In Figure 12, we present the phase diagram for the $B_1AB_2CB_3$ -H blends in the f_{B_2} - ϕ_H plane.

As expected, for blends with $\phi_H \leq 0.1$, the $B_1AB_2CB_3$ block copolymers form mesocrystals with group symmetries of binary ionic crystals. Furthermore, we observe that increase in the length of the f_{B_2} block results in order-order phase transitions between the $C_{A/C}$, α -BN, NaCl and CsCl phases. We also observe an order-order phase transition as a function of ϕ_H , for $\phi_H \leq 0.1$. However, further increase in the homopolymer concentration results in the macrophase separation of the $B_1AB_2CB_3$ -H blends into block copolymer rich, homopolymer rich domains. By calculating the density profiles for the block copolymer rich and homopolymer rich blends we observe that the homopolymer rich domains, with $\phi_H \geq 0.95$ are disordered. Also, the block copolymer rich domains are composed of swollen mesocrystals.

We further investigate the unbinding transition by calculating and comparing the free energies of the

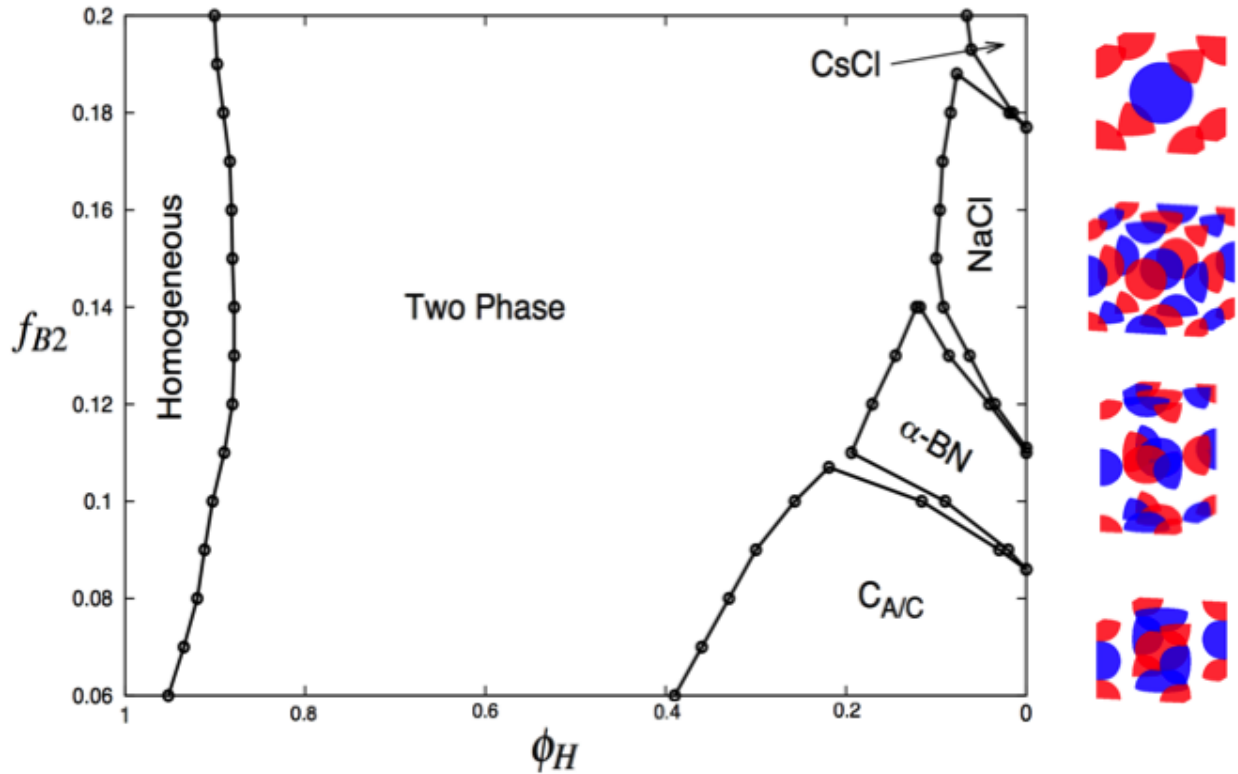


Figure 12: Phase diagram for the $B_1AB_2CB_3$ -H blends in the f_{B2} - ϕ_H plane.

α -BN, single-layer α -BN and the disordered phases for $B_1AB_2CB_3$ -H blends with $f_{B2}=0.11$. In Figure 13 we plot the free energy as a function of the homopolymer chemical potential $\Delta\mu$. Here, increase in $\Delta\mu$ corresponds to an increase ϕ_H . Our results indicate that an increase in the homopolymer concentration results in a macrophase separation of the $B_1AB_2CB_3$ -H blends into block copolymer rich/ homopolymer rich domains. Furthermore, we find that the single-layer α -BN phase is metastable for the given blend parameters. This indicates that the unbinding transition in the α -BN phase is preempted by the macrophase separation of the particular $B_1AB_2CB_3$ -H blend under investigation. The results captured in our study, are consistent with those reported by Pike *et al.* for the AB/A/B ternary blends (85). They discovered that the unbinding transition in the AB/A/B system is preempted by the macrophase separation of the blends into homopolymer rich, block copolymer rich domains.

We further investigate the effects of added homopolymers on the phase behaviour of the α -BN by study-

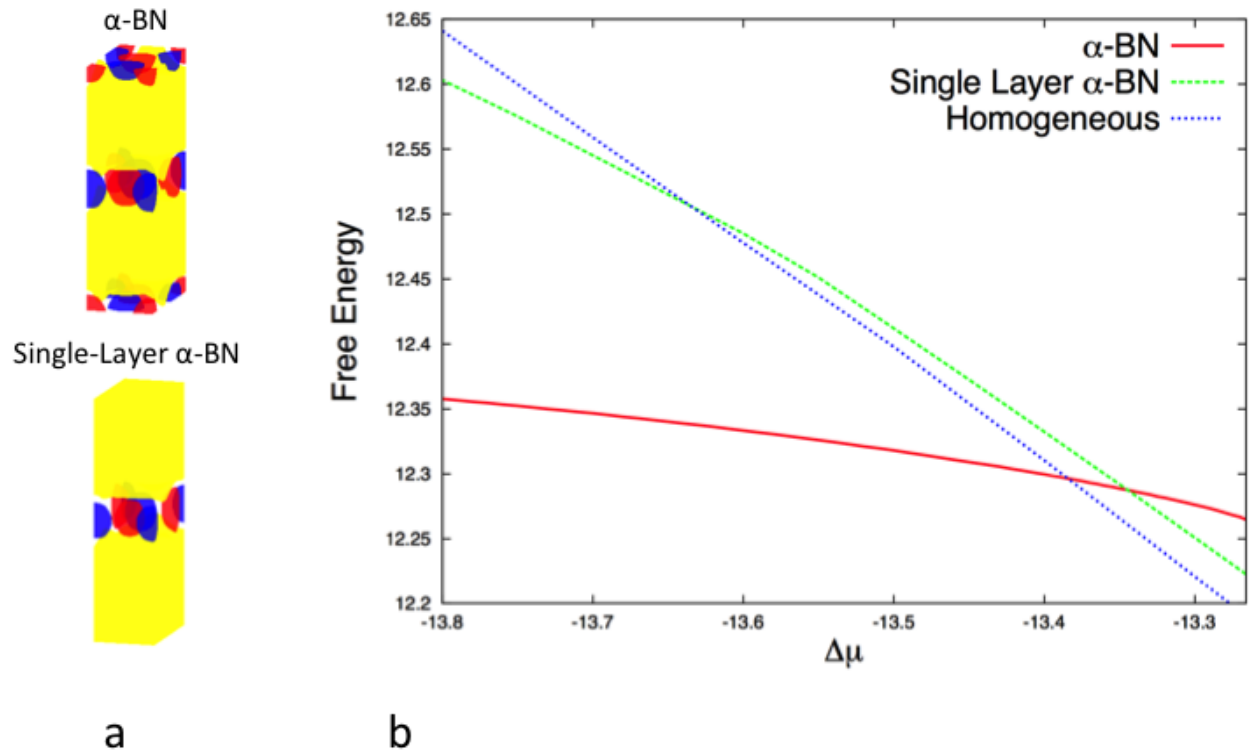


Figure 13: Figure (a), shows the density profiles for the α -BN and single-layer α -BN phases, where homopolymers are shown in yellow. In Figure (b), we show the free energy for the α -BN phase, single-layer α -BN morphology and the disordered phase, as a function of chemical potential.

ing the domain spacing in the x , y and z directions as a function of ϕ_H . An indicator for the unbinding transition is a divergence, at a finite ϕ_H , in the period of the α -BN phase in the direction perpendicular to the planes (85, 89). In Figure 14, we plot the x, y and z components of the α -BN domain spacing as a function of ϕ_H . Here, the values for the L_x, L_y and L_z are plotted prior to the macrophase separation of the $B_1AB_2CB_3$ -H blends. The results presented here indicate that the z -component of the period (L_z) remains finite, indicating that the unbinding transition is preempted by the macrophase separation. However, it is important to note that the added homopolymers concentrate in the region between the α -BN planes, resulting in a more noticeable increase in L_z , as compared with L_x and L_y .

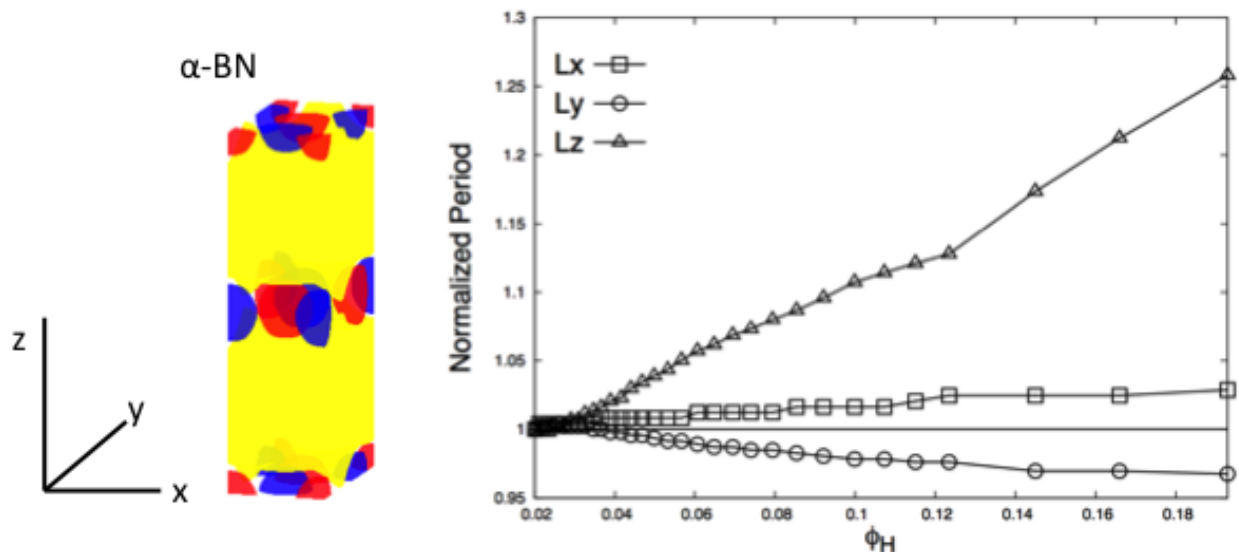


Figure 14: The normalized period of the α -BN phase in the x, y and z directions plotted as a function of homopolymer concentration.

7.3 CONCLUSION

In this study, we used self-consistent field theory to investigate the unbinding transition of the α -BN phase in $B_1AB_2CB_3/H$ pentablock terpolymer homopolymer blends. We focused on the effects of added homopolymers on the binary mesocrystals formed in the $B_1AB_2CB_3$ melts. In agreement with previous studies, we showed that the $B_1AB_2CB_3$ pentablock terpolymers self-assemble into ordered mesocrystals with space group symmetries of the binary ionic crystals. In our study of the phase behaviour of the $B_1AB_2CB_3/H$ blends, we focused on the the $C_{A/C}$, α -BN, NaCl and CsCl morphologies. Among these phases, the α -BN phase is of particular interest for its structural resemblance to the graphite crystal.

We made comparison between the α -BN phase and the graphite structure and argued that the analogy between the two structures goes beyond the structural resemblance. By calculating the density distribution for the B_2 bridge and B_1 and B_3 tail blocks, we showed that the bridge connections between the A and C spheres form mainly within the α -BN layers, whereas, the B_1 and B_3 tail blocks concentrate in the regions between the layers.

To investigate the unbinding transition, we studied the phase behaviour of the $B_1AB_2CB_3/H$ blends. Using the self-consistent field theory, we constructed a phase diagram for the $B_1AB_2CB_3/H$ systems in the $f_{B_2}-\phi_H$ plane. We observed that at a finite homopolymer concentration, the $B_1AB_2CB_3/H$ blends macrophase separate into homopolymer rich, block copolymer rich domains. Based on our self-consistent field theory calculations, we concluded that the unbinding transition in the α -BN phase is preempted by the macrophase separation of the $B_1AB_2CB_3/H$ blends into a homopolymer rich, block copolymer rich domains.

8 | Conclusion and Final Remarks

In this thesis, we used the self-consistent field theory to study the equilibrium properties of inhomogeneous polymeric systems. We presented a detailed formalism of the self-consistent field theory for neutral and charged block copolymers in bulk and confined geometries. We also provided detailed description of numerical techniques, such as Pseudo-Spectral and ADI methods, for solving the SCFT equations. The goal of this thesis was to make use of the self-consistent field theory as a powerful tool to study model systems of complex polymers. The results presented in this thesis advance our understanding of various properties of polymeric systems such as; elastic properties of polymeric membranes, directed self-assembly in polymer thin films and the phase behaviour of block copolymers in bulk.

In our first study, we explored the elastic properties of multi component bilayer membranes. Lipid molecules were modelled as amphiphilic diblock copolymers, forming a bilayer membrane in a solvent modelled as homopolymers. The focus of our study was to understand the relationship between the molecular architecture of the amphiphilic molecules and the line tension or edge energy of the membrane pores. We discovered that the effects of molecular architecture on the line tension depends on the lipids' effective packing structure. Amphiphiles with large head groups and short tails form cone-shaped structures, with spontaneous curvature similar to the curvature of pore edge. We found that the cone-shaped molecules aggregate at the pore edge to relieve the stress caused by the pore's large positive curvature. Therefore, in multi component membranes, increase in the concentration of cone-shaped molecules results in a decrease in the line tension. We observed an opposite behaviour for amphiphiles with short head groups and large tails, forming inverse cone-shaped structures. The inverse cone-shaped molecules have an effective packing structure with negative spontaneous curvature, which is opposite to the curvature of pore edge. We found that in multi component membranes the inverse cone-shaped molecules aggregate away from the pore edge and an increase in their concentration results in an increase in line tension. Lastly, we explored the effects of inter-chain interactions on the line tension. We controlled the repulsive interaction between the amphiphilic

head groups by tuning the Flory-Huggins parameter χ . We discovered that in multi component membranes composed of symmetric molecules, an increase in the repulsive interaction between the head groups results in a decrease in the line tension. We argued that this is due to the formation of effective cone-shaped molecules, which are known to lower the line tension.

An interesting extension to the study of multi component membranes is to investigate the effects of charged molecules and ion concentration on the elastic properties of the membrane. Many lipid molecules are charged, and thus a more realistic model of lipid systems should take into account the charged properties of the lipids. One could explore the effects of ion solubility on elastic properties such line tension, surface tension and bending modulus.

In our second and third study, we explored various mechanisms for directing the self-assembly of block copolymers in thin films. A fundamental challenge with using block copolymers in nano-lithography is the lack of control on the orientation of the ordered micro-domains formed with respect to the thin film surfaces. In many systems, the asymmetry in the interactions between polymer species and air/substrate surfaces results in the formation of micro-domains parallel to the thin film surfaces. In most applications however, the perpendicular orientation is desired. In this thesis, we explored two novel mechanisms for directing the self-assembly of micro-domains in polymer thin films.

In the first study, we considered a charged diblock copolymer system and examined the effects of ion concentration on the critical electric field required to reorient lamellae domains from the parallel to the perpendicular orientation. We considered two scenarios, one in which the neutral blocks were attracted to the top and bottom surfaces, and the other where the charged blocks were. We calculated the free energy of the perpendicular and parallel lamellae phases as a function of ion concentration. In the case where the neutral blocks interacted favourably with the surfaces, we observed that an increase in the concentration of ions lowered the critical electric field. We argued that the decrease in the critical electric field is due to the difference in the magnitude of charge separation between the parallel and perpendicular orientations. In contrast, in the case where the charged species were attracted to the surfaces we discovered that an increase in the ion concentration results in an increase in the critical electric field. In this scenario, we found no difference in the magnitude of charge separation between the parallel and perpendicular phases. However, we showed that in the parallel morphology, the negative and positive species were able to fully wet the top and bottom

electrodes, however this is only partially possible in the perpendicular phase. Therefore, when the charged polymer species are attracted to the thin film surfaces, increase in the concentration of ions results in an increase in the critical electric field.

An interesting extension, inspired by our study of charged polymer thin films, is to explore the effects of ion solubility on the phase behaviour of blends of charged and neutral homopolymers. Based on our previous work, we have shown that blends of charged/neutral homopolymers could form microphases similar to those observed in block copolymer systems. However, this unique property of charged/neutral homopolymer blends is sensitive to the concentration of charged species within the system. In an ongoing project, we are investigating the phase behaviour of charged/neutral homopolymer blends, focusing on the effects of ion solubility on the formation of microphases and their sensitivity to the concentration of charged species.

Continuing with the theme of directed self-assembly, we studied the effects of entropy on the phase behaviour of $(\text{PS-PDMS})_n$ star block copolymers thin films. Using a combination of experiments and self-consistent field theory, we studied the phase behaviour of lamellae and cylinder forming n -arm star block copolymers as a function of the number of arms (n). We modelled the n -arm $(\text{AB})_n$ star block copolymers by joining together the ends of n AB linear diblock copolymers. We observed that for linear $(\text{AB})_1$ block copolymers, the lamellae and cylindrical domains are formed parallel to the thin film surfaces. However, for $(\text{AB})_n$ star block copolymers with $n > 3$, the micro-domains are formed perpendicular at the polymer-substrate and bulk region of the thin film, with thin wetting layer of PDMS (A) species at the air interface. Our experimental and theoretical results indicate that the entropic penalty for aligning domains parallel to the surfaces is greater for star block copolymers with large n value. Therefore we concluded that the entropy of star block copolymers could be used as a mechanism for directing the self-assembly of micro-domains in polymer thin films.

In our last study, we examined the unbinding transition of the α -BN phase in $B_1AB_2CB_3$ pentablock terpolymer/H homopolymer blends. We explored the effects of added homopolymers on the phase behaviour of the $C_{A/C}$, α -BN, NaCl and CsCl morphologies. Using self-consistent field theory, we constructed a phase diagram for the $B_1AB_2CB_3$ -H blends in the ϕ_H - f_{B2} plane. By comparing the free energies of the α -BN, single-domain α -BN and the disordered phase, we showed that the unbinding transition is preempted by the macrophase separation of the blends into homopolymer rich/ block copolymer rich domains.

A natural extension to this work is to explore the parameter space in search for blend parameters for which the unbinding transition in the α -BN is possible. In an ongoing project, we are exploring the parameter space by investigating blends in which the B_1 and B_2 tail blocks interact favourably with the homopolymers. By tuning the relative interactions between the homopolymer species and the tail/bridge blocks, we hope to direct the aggregation of the added homopolymers to domains between the α -BN planes, while preventing the macrophase separation of the $B_1AB_2CB_3$ -H blends.

Bibliography

1. A.-C. Shi, *Developments in Block Copolymer Science and Technology*, ed. by I. W. Hamley *et al.* (Wiley Online Library, 2004), chap. 8.
2. T Thurn-Albrecht *et al.*, *Science* **290**, 2126–2129 (2000).
3. M. Park, C. Harrison, P. M. Chaikin, R. A. Register, D. H. Adamson, *Science* **276**, 1401–1404 (1997).
4. I. Y. Galaev, B. Mattiasson, *Trends in Biotechnology* **17**, 335–340 (1999).
5. R. Phillips, J. Kondev, J. Theriot, H. Garcia, *Physical Biology of The Cell* (Garland Science, 2012).
6. J. Lötters, W Olthuis, P. Veltink, P Bergveld, *Journal of Micromechanics and Microengineering* **7**, 145 (1997).
7. M. Rubinstein, R Colby, *Polymers Physics* (Oxford, UK, 2003).
8. L. H. Sperling, *Introduction to Physical Polymer Science* (John Wiley & Sons, 2005).
9. Y. Tu, X. Wan, D. Zhang, Q. Zhou, C. Wu, *Journal of the American Chemical Society* **122**, 10201–10205 (2000).
10. G. Fredrickson, *The Equilibrium Theory of Inhomogeneous Polymers* (Oxford University Press, USA, 2006).
11. T. Kawakatsu, *Statistical Physics of Polymers: an Introduction* (Springer Science & Business Media, 2013).
12. E. Helfand, *Macromolecules* **8**, 552–556 (1975).
13. P.-G. De Gennes, *Reports on Progress in Physics* **32**, 187 (1969).
14. S. Edwards, *Proceedings of the Physical Society* **88**, 265 (1966).
15. L. Leibler, *Macromolecules* **13**, 1602–1617 (1980).

16. A. Semenov, *Macromolecules* **26**, 6617–6621 (1993).
17. M. W. Matsen, M. Schick, *Physical Review Letters* **72**, 2660 (1994).
18. M. W. Matsen, M. Schick, *Current Opinion in Colloid & Interface Science* **1**, 329–336 (1996).
19. J. Scheutjens, G. Fleer, *Journal of Physical Chemistry* **83**, 1619–1635 (1979).
20. A.-C. Shi, J. Noolandi, R. C. Desai, *Macromolecules* **29**, 6487–6504 (1996).
21. J. Vavasour, M. Whitmore, *Macromolecules* **25**, 5477–5486 (1992).
22. E. Helfand, Z. Wasserman, *Macromolecules* **9**, 879–888 (1976).
23. F. Drolet, G. H. Fredrickson, *Macromolecules* **34**, 5317–5324 (2001).
24. F. Drolet, G. H. Fredrickson, *Physical Review Letters* **83**, 4317 (1999).
25. A.-C. Shi, J. Noolandi, *Macromol. Theory Simul* **8**, 214–229 (1999).
26. Q. Wang, T. Taniguchi, G. H. Fredrickson, *The Journal of Physical Chemistry B* **108**, 6733–6744 (2004).
27. B. Yu *et al.*, *Physical Review Letters* **96**, 138306 (2006).
28. P. Chen, H. Liang, A.-C. Shi, *Macromolecules* **41**, 8938–8943 (2008).
29. Y. Yang, F. Qiu, H. Zhang, Y. Yang, *Polymer* **47**, 2205–2216 (2006).
30. J. Li, K. A. Pastor, A.-C. Shi, F. Schmid, J. Zhou, *Physical Review E* **88**, 012718 (2013).
31. M. Whitmore, J. Whitehead, A Roberge, *Canadian Journal of Physics* **76**, 831–881 (1998).
32. P. M. Chaikin, T. C. Lubensky, *Principles of Condensed Matter Physics* (Cambridge Univ Press, 2000), vol. 1.
33. M. Doi, S. F. Edwards, *The Theory of Polymer Dynamics* (oxford university press, 1988), vol. 73.
34. M. Doi, *Introduction to Polymer Physics* (Oxford university press, 1996).
35. D. Chandler, *Introduction to Modern Statistical Mechanics* (Oxford University Press, 1987).
36. H. Kleinert, *Path Integrals in Quantum Mechanics, Statistics, Polymer Physics, and Financial Markets* (World Scientific, 2009).

37. N. G. Van Kampen, *Stochastic Processes in Physics and Chemistry* (Elsevier, 1992), vol. 1.
38. L. Wang, J. Lin, Q. Zhang, *Soft Matter* **9**, 4015–4025 (2013).
39. W. Li, M. Liu, F. Qiu, A.-C. Shi, *The Journal of Physical Chemistry B* **117**, 5280–5288 (2013).
40. S Zhu *et al.*, *Nature* **400**, 49–51 (1999).
41. M Müller, L. G. MacDowell, *Macromolecules* **33**, 3902–3923 (2000).
42. M. Matsen, *The Journal of Chemical Physics* **106**, 7781–7791 (1997).
43. V Khanna *et al.*, *Macromolecules* **39**, 9346–9356 (2006).
44. M Muthukumar, J. S. Ho, *Macromolecules* **22**, 965–973 (1989).
45. T. G. Pedersen, P. M. Johansen, N. C. R. Holme, P. Ramanujam, S. Hvilsted, *Physical Review Letters* **80**, 89 (1998).
46. M. Bawendi, K. F. Freed, U. Mohanty, *The Journal of Chemical Physics* **87**, 5534–5540 (1987).
47. G. H. Fredrickson, V. Ganesan, F. Drolet, *Macromolecules* **35**, 16–39 (2002).
48. G Tzeremes, K. Rasmussen, T Lookman, A Saxena, *Physical Review E* **65**, 041806 (2002).
49. J.-L. Barrat, G. H. Fredrickson, S. W. Sides, *The Journal of Physical Chemistry B* **109**, 6694–6700 (2005).
50. Y. Bohbot-Raviv, Z.-G. Wang, *Physical Review Letters* **85**, 3428 (2000).
51. B. Fornberg, *A Practical Guide to Pseudospectral Methods* (Cambridge university press, 1998), vol. 1.
52. R. A. Friesner, *Chemical Physics Letters* **116**, 39–43 (1985).
53. K. Rasmussen, G Kalosakas, *Journal of Polymer Science Part B: Polymer Physics* **40**, 1777–1783 (2002).
54. W. H. Press, S. A. Teukolsky, W. T. Vetterling, B. P. Flannery, *Numerical recipes in C*, 1992.
55. J. London, *Modeling Derivatives in C++* (John Wiley & Sons, 2005), vol. 263.
56. N. Ozisik, *Finite Difference Methods in Heat Transfer* (CRC press, 1994).
57. J.-R. Roan, T. Kawakatsu, *The Journal of Chemical Physics* **116**, 7283–7294 (2002).

58. W. Helfrich, *Zeitschrift für Naturforschung C* **28**, 693–703 (1973).
59. Y. Tsori, F. Tournilhac, D. Andelman, L. Leibler, *Physical Review Letters* **90**, 145504 (2003).
60. T. Xu *et al.*, *Macromolecules* **38**, 10788–10798 (2005).
61. J. Bang, U. Jeong, D. Y. Ryu, T. P. Russell, C. J. Hawker, *Advanced Materials* **21**, 4769–4792 (2009).
62. Y. Xia, G. M. Whitesides, *Annual Review of Materials Science* **28**, 153–184 (1998).
63. M. Lazzari, G. Liu, S. Lecommandoux, *Block Copolymers in Nanoscience* (Wiley. com, 2007).
64. J. Bang, U. Jeong, D. Y. Ryu, T. P. Russell, C. J. Hawker, *Advanced Materials* **21**, 4769–4792 (2009).
65. Y. Bae, S. Fukushima, A. Harada, K. Kataoka, *Angewandte Chemie International Edition* **42**, 4640–4643 (2003).
66. J. Y. Cheng *et al.*, *Advanced Materials* **13**, 1174–1178 (2001).
67. K. Liu, S. M. Baker, M. Tuominen, T. P. Russell, I. K. Schuller, *Physical Review B* **63**, 060403 (2001).
68. W. A. Lopes, H. M. Jaeger, *Nature* **414**, 735–738 (2001).
69. R. Li *et al.*, *Applied Physics Letters* **76**, 1689–1691 (2000).
70. A. Urbas *et al.*, *Advanced Materials* **12**, 812–814 (2000).
71. Z. Nie, E. Kumacheva, *Nature Materials* **7**, 277–290 (2008).
72. A. Semenov, *Macromolecules* **26**, 2273–2281 (1993).
73. M. Matsen, *Macromolecules* **28**, 5765–5773 (1995).
74. F. S. Bates *et al.*, *Faraday Discussions* **98**, 7–18 (1994).
75. M. Laradji, A.-C. Shi, R. C. Desai, J. Noolandi, *Physical Review Letters* **78**, 2577 (1997).
76. F. S. Bates, G. H. Fredrickson, *Annual Review of Physical Chemistry* **41**, 525–557 (1990).
77. A. K. Khandpur *et al.*, *Macromolecules* **28**, 8796–8806 (1995).
78. M. Matsen, R. Thompson, *The Journal of Chemical Physics* **111**, 7139–7146 (1999).
79. C. A. Tyler, J. Qin, F. S. Bates, D. C. Morse, *Macromolecules* **40**, 4654–4668 (2007).
80. A.-C. Shi, B. Li, *Soft Matter* **9**, 1398–1413 (2013).

81. N. Xie *et al.*, *Journal of the American Chemical Society* **136**, 2974–2977 (2014).
82. X. Ye *et al.*, *The Journal of Physical Chemistry B* **110**, 23578–23582 (2006).
83. F. S. Bates *et al.*, *Science* **336**, 434–440 (2012).
84. J.-H. Choi, A. Kota, K. I. Winey, *Industrial & Engineering Chemistry Research* **49**, 12093–12097 (2010).
85. D. Q. Pike, M. Müller, J. J. dePablo, *The Journal of Chemical Physics* **135**, 114904 (2011).
86. S Komura, N Shimokawa, T Kato, *The Journal of Chemical Physics* **124**, 034906 (2006).
87. L. Corvazier *et al.*, *Journal of Materials Chemistry* **11**, 2864–2874 (2001).
88. R. Wang *et al.*, *Macromolecules* **42**, 2275–2285 (2009).
89. P. K. Janert, M Schick, *Macromolecules* **30**, 137–144 (1997).
90. G. Pandav, V. Ganesan, *Macromolecules* **46**, 8334–8344 (2013).
91. P. K. Janert, M Schick, *Macromolecules* **31**, 1109–1113 (1998).
92. M. W. Matsen, *Macromolecules* **36**, 9647–9657 (2003).
93. S. K. Pati, T. Enoki, C. N. R. Rao, *Graphene and its Fascinating Attributes* (World Scientific, 2011).